The Dissertation Committee for Mark Charles Monti
certifies that this is the approved version of the following dissertation:

The effect of epitaxial strain and R^{3+} magnetism on the interfaces between polar perovskites and $SrTiO_3$

Committee:

John T. Markert, Supervisor

Alex de Lozanne

Maxim Tsoi

Zhen Yao

Alan Campion

The effect of epitaxial strain and R^{3+} magnetism on the interfaces between polar perovskites and $SrTiO_3$

by

Mark Charles Monti, B.S.

DISSERTATION
Presented to the Faculty of the Graduate School of
The University of Texas at Austin
in Partial Fulfillment
of the Requirements
for the Degree of

DOCTOR OF PHILOSOPHY

THE UNIVERSITY OF TEXAS AT AUSTIN
May 2011

Dedicated to Holly

Acknowledgments

I'd first like to thank my wife Holly, who has always believed in me and given me confidence during times of doubt. My life with Holly outside of physics is something that I truly love and cherish and has made these six exciting years to fly by. I can't imagine what graduate school would have been like had I not been so close to and had such great support from my parents Susan and Steve. It has been great being back in Austin and being able to spend time with my family. I will sorely miss our weekly dinners and knowing that you are only a short drive or bike ride away. Holly's parents Ted and Gail have been like a second set of parents over the past six years, and I am really grateful to have been such an integrated part of their family. I'll always be available for vacations to Hawaii!

John Markert, my advisor and mentor, has been a constant source of support and advice, even before I was one of his graduate students. His calm demeanor and abundant knowledge of everything 'physics' made any problem seem solvable and no project too daunting. Thanks, John, for giving me the opportunity to work in your lab and learn from you; I've really enjoyed being one of your students.

My lab mates have always made the lab a great environment to work in. I'd especially like to thank Jackson Stolle and Shirin Mozafarri who helped tremendously in the work presented in this dissertation. It was a pleasure working closely with the two of you. Han-Jong Chia was a great lab partner during our work together on the NMRFM ^{3}He probe, and Isaac, Rosie, and Jeremy were always happy to help in any way possible; I really enjoyed our time together in the lab.

Martin Kochanczyk and Ben King were great friends and study partners, and between playing trashket ball and tennis we gave ourselves a little distraction from the homework sets. I've really enjoyed taking vacations and hanging out with Martin, Carlie, Ralph and Nina. I'd also like to thank Ralph for letting me draft on his broad shoulders during those long bike rides. Austin has been a great place to be for graduate school, and it is because of my friends and family that I've enjoyed my time here so much. Thank you all for your support!

The effect of epitaxial strain and R^{3+} magnetism on the interfaces between polar perovskites and $SrTiO_3$

Publication No. __________________

Mark Charles Monti, Ph.D.
The University of Texas at Austin, 2011

Supervisor: John T. Markert

We have embarked on a systematic study of novel charge states at oxide interfaces. We have performed pulsed laser deposition (PLD) growth of epitaxial oxide thin films on single crystal oxide substrates. We studied the effects of epitaxial strain and rare-earth composition of the metal oxide thin films. We have successfully created TiO_2 terminated $SrTiO_3$ (STO) substrates and have grown epitaxial thin films of $LaAlO_3$ (LAO), $LaGaO_3$ (LGO), and $RAlO_3$ on STO using a KrF pulsed excimer laser. Current work emphasizes the importance of understanding the effect of both epitaxial strain and R^{3+} magnetism on the interface between $RAlO_3$ and STO. We have demonstrated that the interfaces between LAO/STO and LGO/STO are metallic with carrier concentrations of 1.1×10^{14} cm^{-2} and 4.5×10^{14} cm^{-2}, respectively. Rare-earth aluminate films, $RAlO_3$, with R = Ce, Pr, Nd, Sm, Eu, Gd, and Tb, were also grown on STO. Conducting interfaces were found for R = Pr, Nd and Gd, and the results indicate that for $R \neq La$ the magnetic nature of the R^{3+} ion causes

increased scattering with decreasing temperature that is modeled by the Kondo effect. Epitaxial strain between the polar $RAlO_3$ films and STO appears to play a crucial role in the transport properties of the metallic interface, where a decrease in the R^{3+} ion size causes an increase in sheet resistance and an increase in the onset temperatures for increased scattering.

Table of Contents

List of Tables

List of Figures

Chapter 1

Introduction

In Herbert Kroemers Nobel lecture in 2000, he stated that the interface is the device, a statement that has become increasingly more true over the past decade [1]. His remarks concerned the interfaces between semiconductor heterostructures and thus referred to electronic devices as a whole. In essence, size matters and smaller is better in the case of electronic devices. Thus, the ability to control and understand the electronic properties of materials at the interfacial level is of great interest. The development of experimental methods used to create epitaxial heterostructures of semiconducting materials has led to countless technological advancements. Methods such as molecular beam epitaxy (MBE), chemical vapor deposition (CPE) and pulsed laser deposition (PLD) have allowed research on thin film and interface properties to flourish over the last few decades. The electronic and magnetic properties of materials can change drastically at interfaces, giving rise to states not seen in either bulk material, such as ferromagnetism, conductivity, and even superconductivity [2, 3, 4]. Out of all of these unique interface systems, the recent discovery of a two-dimensional electron gas (2DEG) between band insulators $SrTiO_3$ (STO) and $LaAlO_3$ (LAO) has sparked a great amount of research interest.

In 2004, Hwang discovered that a thin film of LAO deposited epitaxially on STO gave rise to a conducting layer at the interface between the thin film and the STO substrate [2]. This breakthrough has led to countless research efforts over the last 7 years aimed at understanding both the electronic properties and the nature of the metallic state found at the interface of LAO/STO. This interface displays a high mobility, n-type 2DEG that becomes superconducting at extremely low temperatures [2, 5, 6, 7, 8, 9, 10, 11, 12, 13, 14, 15]. The electronic properties of this interface have been extensively studied and reported; however, the exact mechanism behind the charge doping at the interface remains an open question. The extent of La intermixing or diffusion into the STO substrate and the role of oxygen vacancies at the interface are two of many unanswered questions that affect the nature of the 2DEG [16, 17, 18]. The roles of both epitaxial strain at the interface and magnetic over-layers have yet to be explored in detail. This work aims to unravel the mystery behind the conducting state between insulating oxides by systematically studying the roles of both epitaxial strain and magnetism on the interface between polar perovskites and $SrTiO_3$.

1.1 Two dimensional electron gas: 2DEG

The LAO/STO system presents a unique opportunity to explore the physics of a two dimensional system. Although the conducting region of the interface is estimated to be a few nanometers thick, the electron gas at the interface can be viewed as a quasi-2DEG [19, 20, 21]. The electrons at the interface between LAO/STO are free to move parallel to the interface (xy plane), but are confined in the z direction and thus can be thought of as a two dimensional sheet of electrons sandwiched between two insulators. Interesting phenomena can result from this confinement of electrons in two dimensions due to the quantization of the electrons energy levels in the z-direction. Observation of the quantum Hall effect is unique property of such systems and has been reported for 2D systems [22].

A simple model of a 2D system can be achieved by imposing boundary conditions on Schrödingers equation, which creates a potential well that restricts the particles' motion. This straightforward model, often referred to as the particle in a box, is instructive due to both its simplicity and its implications for the energy levels of an electron in a 2DEG. Consider the time independent Schrödinger equation for one dimension

$$\hat{H}\Psi(x) = E\Psi(x) \tag{1.1}$$

or more precisely,

$$\frac{-\hbar^2}{2m}\frac{\partial^2}{\partial^2 x}\Psi(x) + V(x)\Psi(x) = E\Psi(x) \tag{1.2}$$

where $V(x)$ is the position dependent potential and $\Psi(x)$ is the particle's wave function. A free particle is non-interacting and weakly bound, such as a conduction electron in a metal which propagates freely past the ionic cores and scatters infrequently with other conduction electrons, and hence $V(x) = 0$. This type of particle is free to propagate over all space with energy equal to

$$E = \frac{\hbar^2 k^2}{2m} \tag{1.3}$$

and thus momentum $p = \hbar k$, where k is the wave vector. A free particle thus has continuous energy levels described by equation 1.3. Now consider a particle bound to one dimension by infinite potential barriers at $x = 0$ and $x = L$, where $V(x) = 0$ for $0 < x < L$. A wave function for this particle in a box is

$$\Psi = A \sin(\frac{n\pi x}{L}) \tag{1.4}$$

where n is a non-zero integer and A is a normalization constant. The wave function for the first three energy levels is plotted in figure 1.1 as well as the more realistic scenario where the potential barrier is finite and thus the wave function for the particle can extend into the medium on either side of the box [23]. Equation 1.3 yields

$$E_n = \frac{\hbar^2 n^2 \pi^2}{2mL^2},\ n = 1, 2, 3\ldots \tag{1.5}$$

The restriction on the values of energy arises due to the boundary conditions that confine the particle. Thus, confinement leads to energy quantization. If N electrons that obey the Pauli exclusion principle are confined in such a box

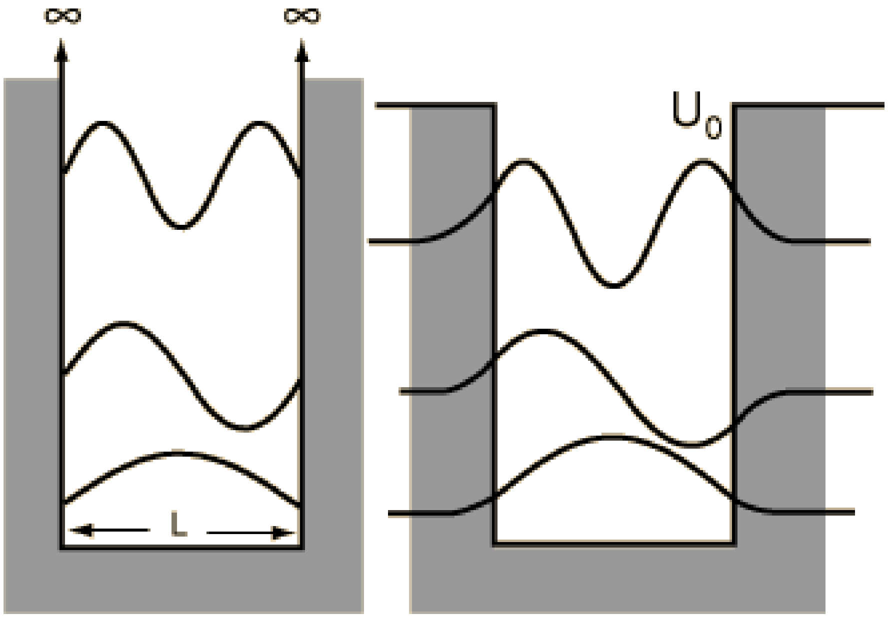

Figure 1.1: The wave function for a particle in a box with infinite potential barriers (left) and finite barriers (right) Plot taken from Ref. [23]

then there are 2 electrons ($m_s = \pm\frac{1}{2}$) for each value of n and thus for each energy level E_n. If the top most filled energy level is n_f then the Fermi energy ϵ_F is given by

$$\epsilon_F = \frac{\hbar^2 n_F^2 \pi^2}{2mL^2} = \frac{\hbar^2 N^2 \pi^2}{8mL^2}. \tag{1.6}$$

This example of a particle in a box is relevant to the 2DEG in the LAO/STO system because here the electrons are confined to the interface by insulating slabs on either side but are free to move within the plane. Thus, the quantum nature of electrons at the LAO/STO interface is modeled well by the 1D particle in a box example.

Chapter 2

Materials

The materials used in this work for both the substrates and the thin films consist of perovskite oxides. These oxides have very similar crystal structures and thus allow the formation of epitaxial heterostructures. The substrates are always STO, which are primarily purchased from MTI Corporation[1], and all of the targets that produce the thin films are created in our lab by solid state reaction. These materials will be described in detail below.

2.1 Perovskites

The perovskite family of materials takes on the general form ABX_3, where A is a large cation, B is a smaller cation and X is an anion that bonds to B, while A is typically closed-shelled. Perovskites can form with X as a halogen, but in the case of oxides X is always oxygen. This class of materials displays a broad range of behavior and depending on the chemical composition can be superconducting, semiconducting, insulating, ferroelectric, or piezoelectric. They also form a variety of crystal structures such as cubic, orthorhombic and rhombohedral and have phase transitions between such structures under

---

[1] www.mtixtl.com

various conditions. Figure 2.1a shows the cubic perovskites structure. The B cation occupies the cube center and is surrounded by an oxygen octahedra and the A cations are at the corners [24]. Figure 2.1b shows the crystal structure from a different perspective where the A cation occupies the center and the B cations occupy the cube corners. In this work the STO substrates and the thin films ($LaAlO_3$, $LaGaO_3$ (LGO), and various rare earth aluminates $RAlO_3$) take on this cubic structure, but often a slight rotation or tilting of the oxygen octahedra can create a psuedo-cubic unit cell such as rhombohedral or orthorhombic.

Viewing the ABO_3 perovskite structure as alternating sheets of AO and BO_2 yields a simple ionic picture of the building blocks of these crystals. For example, a unit cell of STO contains alternating layers of SrO and TiO_2. In the ionic limit the oxidation state of oxygen is always O^{2-} and thus the layers $[Sr^{+2}O^{-2}]^0$ and $[Ti^{+4}O_2^{-4}]^0$ are charge neutral. This layer-by-layer evaluation of this crystal structure indicates that bulk STO is non-polar. However, applying the same treatment to LAO gives a completely different result. The layers comprising a unit cell of LAO are $[La^{+3}O^{-2}]^{+1}$ and $[Al^{+3}O_2^{-4}]^{-1}$, which creates a polar structure. The leading theory for the creation of a charged state at the interface between LAO/STO or LGO/STO revolves around the polar discontinuity between the film and the substrate and will be discussed in detail in Section 2.4.

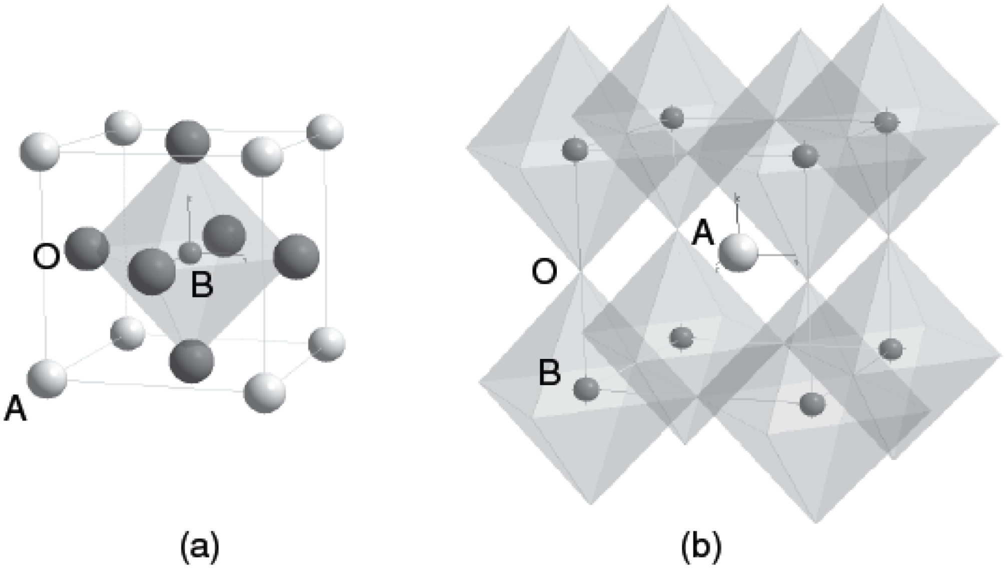

Figure 2.1: The perovskite crystal unit cell showing both viewpoints (a) the B cation at the center surrounded by an oxygen octahedra at the face centers and (b) the A cation at the center and the B cations at the corners surrounded by oxygen octahedrons. Taken from Ref. [24]

2.2 $SrTiO_3$ substrates

All thin films in this work are deposited on single crystal (001) STO substrates. A full description the substrate preparation and characterization will be given in Section 4.1; this section aims to discuss the properties of bulk STO. STO is a very suitable candidate for epitaxial thin film growth due to its nearly temperature independent thermal expansion coefficient of 3.23×10^{-5} K^{-1} and its stable cubic phase from room temperature up to the melting point at 2080 °C [25]. Figure 2.2 displays the thermal expansion of the cubic phase of STO; this plot becomes important when determining optimal growth conditions. The only structural phase change occurs below 110 K where STO becomes tetragonal due to a slight tilting of the oxygen octahedras. Room temperature cubic STO has a lattice constant of 3.905 Å and is a band insulator with a band gap of 3.2 eV [26]. Even though STO is an insulator in its pure state it can become conducting if either reduced or doped [27, 28, 29]. The addition of La as a substitute for Sr can cause n-type conductivity to be observed in doped STO [30]. Also, reduced STO, achieved by heating under low vacuum, can cause STO to become metallic. These two features of bulk STO raise the question: is the 2DEG at the interface between LAO/STO a result of a charge transfer due to the polar nature of LAO or a result of either oxygen vacancies or diffusion of La into the first few atomic layers of STO?

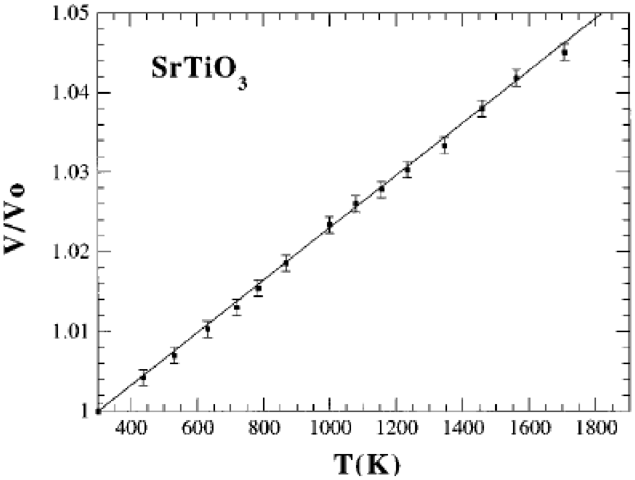

Figure 2.2: This plot shows the thermal expansion of STO, where V_O is the room temperature volume of the STO unit cell. This data is important because the expansion is linear over the temperature ranges that are used during crystal growth. Taken from Ref. [25]

2.3 $RAlO_3$

The rare-earth alluminates ($RAlO_3$) all form perovskite crystals. For instance, LAO is a rhombohedral perovskite with a c axis lattice constant of 3.789 Å and a band gap of 5.6 eV at room temperature, but when heated past 813 K, LAO becomes cubic [31]. Both the thermal expansion and phase change of LAO are shown in figure 2.3. Typical growth conditions for LAO on STO are at temperatures above 750 °C, where LAO is cubic and has with a lattice mismatch of 3.25% with STO. Going from left to right across the periodic table, the $RAlO_3$ decrease in size due to the lanthanide contraction (see table 1); however, the perovskite structure remains intact for the entire rare-earth series.

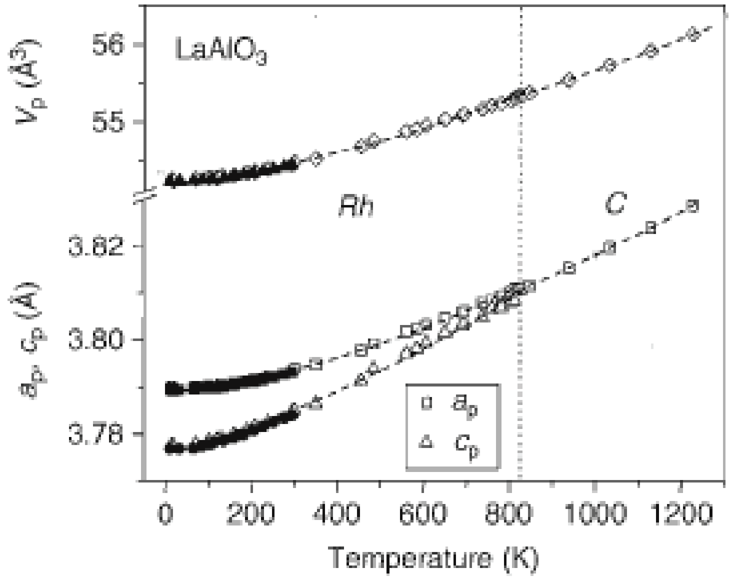

Figure 2.3: This plot shows the thermal expansion of LAO. This data was taken from Ref. [32]

2.4 Interfaces between polar films and STO

The current model of the 2DEG formed between polar perovskites and STO is based almost entirely on two systems, LAO/STO and LGO/STO, both of which are almost identical in properties [33]. In each of these systems a metallic interface occurs for thin films of 4 unit cells or greater [5, 33]. This experimental evidence promotes a model known as the polar catastrophe that predicts charge doping at the interface. In this model the polar nature of the thin film drives the insulator to conductor transition due to an electronic reconstruction at the interface based on the mixed valence state of titanium.

The first formulation of the effects of a polar heterostructure were developed by W. A. Harrison for the Ge:GaAs interface [34]. This model looks at the electric potential of planes parallel to the interface by integrating Poisson's equation, and figure 2.4 shows the potential developed for the Ge:GaAs system. This potential would continue to increase with increasing layers of GaAs, creating an unrealizable potential divergence. In this system an atomic reconstruction occurs that causes an alternating potential which is shown in figure 2.5.

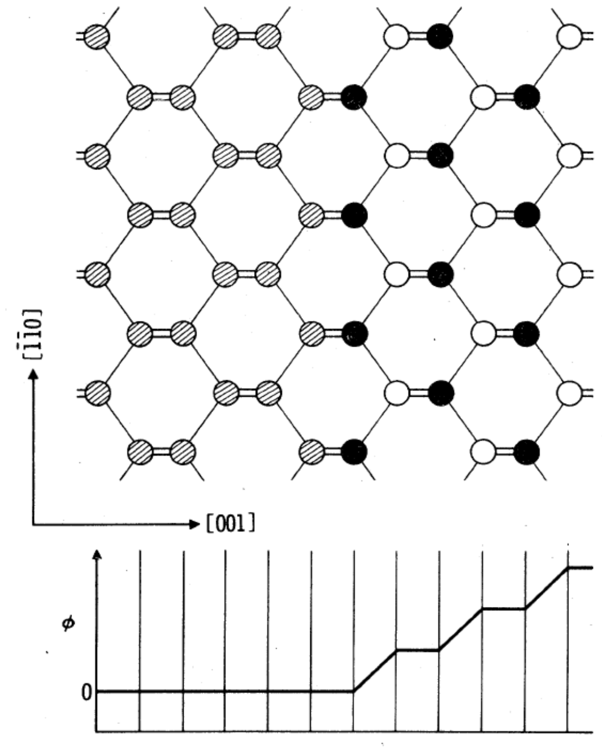

Figure 2.4: This plot shows the original polar heterojunction between Ge and GaAs. The Ge atoms are striped, Ga atoms are black and the As atoms are white. The first row of atoms after the Ge plane is negative and the next row of atoms, As, is positive. The lower image shows the potential generated by the GaAs film which was obtained by integrating Poisson's equation from left to right. Taken from Ref. [34]

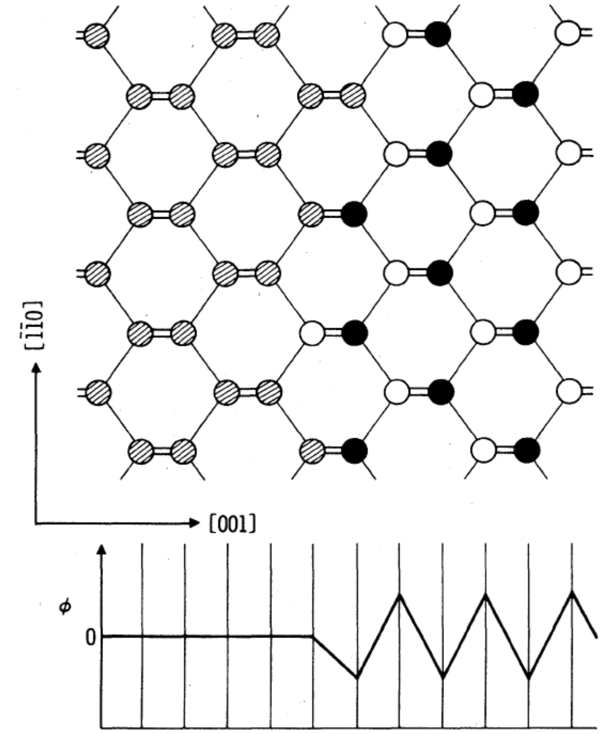

Figure 2.5: This plot shows the reconstructed interface between Ge and GaAs. The first row after the Ge rows has 1/4 As and the second row has 3/4 Ga which produce an alternating potential that eliminates the potential build up due to the polar GaAs layers. Taken from Ref. [34]

The LAO/STO system is similar to the Ge:GaAs case in that the polar LAO film produces a diverging potential. The polar layers and the associated potential are shown in figure 2.6. The potential created by such a polar film can be derived using Gauss' Law, where the electric field $\boldsymbol{E}$ at a distance z away from the interface is given by

$$\oint \boldsymbol{E} \cdot d\boldsymbol{a} = \frac{Q}{\epsilon_\circ} \tag{2.1}$$

which yields,

$$\boldsymbol{E} = \frac{\sigma}{2\epsilon_\circ}. \tag{2.2}$$

Here σ is the surface charge density, which is positive, +e/unit cell, for LaO layers and negative, -e/unit cell, for AlO_2 layers. The electric potential is now

$$\Phi = \oint \boldsymbol{E} \cdot d\boldsymbol{l} = \frac{\sigma z}{2\epsilon_\circ}. \tag{2.3}$$

Once the first charge layer, positive LaO, is deposited the potential, Φ, increases linearly until the next layer of opposite charge, AlO_2, is deposited. The potential is constant at this point and increases linearly again with the deposition of the next LaO layer. The potential will continue to increase with increasing film thickness unless some mechanism alters the charged state at the interface. This building up of the electric potential is what is coined the polar catastrophe. It is this polar catastrophe that causes an electronic reconstruction to occur at the interface, whereby each Ti atom at the interface donates 1/2 an electron, which effectively changes the diverging potential into an alternating potential as in the case of the Ge:GaAs system.

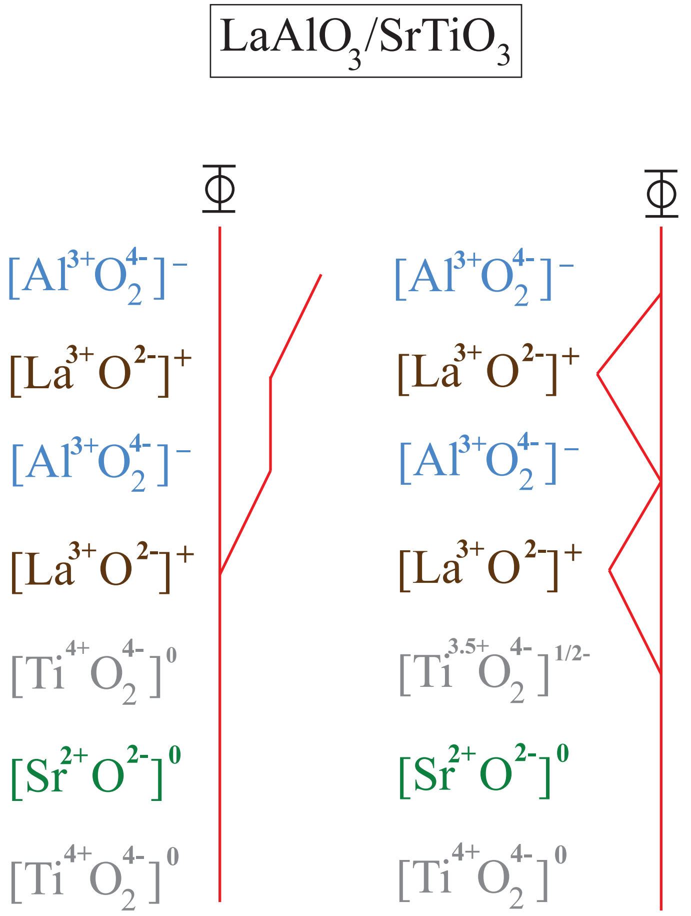

Figure 2.6: The left plot shows stacking sequence of the polar LAO layers for the LAO/STO system and the associated potential that diverges with thickness. The right plot shows the reconstructed interface and the alternating potential that occurs when the Ti atoms donate electrons to the interface.

The potential generated by the film takes the same form as in Harrison's model that describes the Ge:GaAs system. The main difference between the LAO/STO system and the Ge:GaAs system is that the diverging potential causes an electronic reconstruction to occur at the LAO/STO interface. This justification of the charge doping at the interface has very important implications on the nature of the 2DEG in LAO/STO. If there truly is an electronic reconstruction then the interface between LAO/STO is perfectly clean and the mobile electrons are due to the polar catastrophe model and ultimately from the Ti atoms at the interface. However, if there is an atomic reconstruction, similar to the Ge:GaAs case, then diffusion of La atoms into STO could result in both an alternating potential and conducting STO. This has been highly debated and there is evidence supporting both cases, but the current consensus is that the polar catastrophe causes the charged state at the interface due to an electronic reconstruction. This leaves open the very important question of the true nature behind the charged state between polar films and STO. This study aims to illuminate the mechanism that drives the conducting interface by investigating the role of epitaxial strain and magnetism on the conducting properties of polar thin films and STO.

2.5 RAlO$_3$ Polar Perovskites

In order to better understand the true nature of the charged state at the interface between polar perovskites and STO, different polar rare-earth aluminates (RAlO$_3$) were deposited onto STO substrates. The series of RAlO$_3$

perovskites deposited include: La, Ce, Pr, Sm, Nd, Eu, Gd, and Tb. The lattice size of each rare-earth aluminate decreases as you move from left to right across the lanthanide series by roughly 0.5% per step. Detailed information regarding the precise crystal structure and magnetic behavior of these materials will be discussed along with the experimental results for these materials. The purpose of exploring the heterostructures formed by these materials and STO is to understand the role of epitaxial strain and differing magnetic natures of the polar films on the interfaces formed. The role of epitaxial strain on the interface was also explored by studying the $La_xY_{1-x}AlO_3$ and $La_xEu_{1-x}AlO_3$ series.

Chapter 3

Pulsed Laser Deposition

There are two primary techniques that have been developed for the creation of epitaxial thin films, molecular beam epitaxy (MBE) and pulsed laser deposition (PLD) [35]. MBE systems use one or several source materials, that, upon heating, create a flux of evaporated atoms that are shuttered on and off to create the correct stoichiometric ratio for the desired film. These systems can create layer-by-layer epitaxial growth, but they are very expensive and labor intensive to operate due to the importance of precise calibration of the flux from the various elemental sources. This calibration is done using quartz crystals to measure the deposition rate for various conditions and is used to control the stoichiometry of the thin film. PLD, however, creates epitaxial growth by focusing a high power laser pulse onto a stoichiometric target that evaporates the material and coats an often heated substrate. PLD systems require far less equipment than MBE systems and can create the same layer-by-layer growth as their expensive counterpart. In the work described in this thesis, a PLD system was used to create all of our epitaxial oxide thin films.

The pulsed laser deposition system (PLD) that I installed for this work creates epitaxial thin films uses a Lambda Physik COMPex 201 KrF (248 nm) pulsed excimer laser (excimer lasers get their name because the lasing occurs due to an excited dimer). In this case, the excimer is krypton fluoride (KrF), which produces intense light in the UV range. The laser has a pulse duration of 25 ns, a maximum power outputof 600 mJ, and pulse repetition rates up to 5 Hz. The high energy laser pulse ablates a 2−3 mm spot on a rotating polycrystalline target, creating a plasma plume of the oxide which can then deposit epitaxially on an STO substrate. The single crystal STO substrates are heated using a custom designed heater capable of reaching temperatures above 750°C. After deposition, films are cooled to room temperature under the same oxygen pressure used during growth. Detailed explanation of the growth conditions will be described in chapter 4.

3.1 Deposition Chamber

The deposition chamber contains the target, substrate heater, pressure gauges and valves that allow the control of oxygen pressure during growth. A schematic of the PLD system, which includes both the deposition chamber and the laser, is shown in figure 3.1. When swapping targets or substrates, access to the chamber is made via the main door on the left hand side, but there is a second door that is blocked by the rear wall that was used to perform more complicated alterations to the interior of the chamber. Detailed pictures of both the deposition chamber and the front panel can be seen in figures 3.2 and 3.3, respectively.

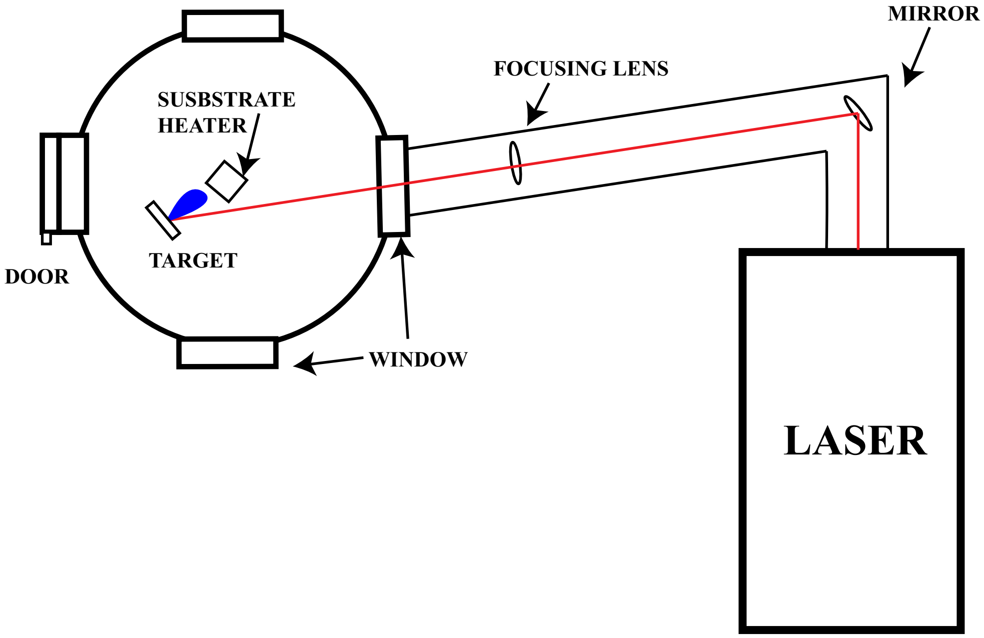

Figure 3.1: A schematic diagram of the PLD system. The laser exits the laser tube and is reflected to a focusing lens, then enters the chamber through a window and ablates a rotating target.

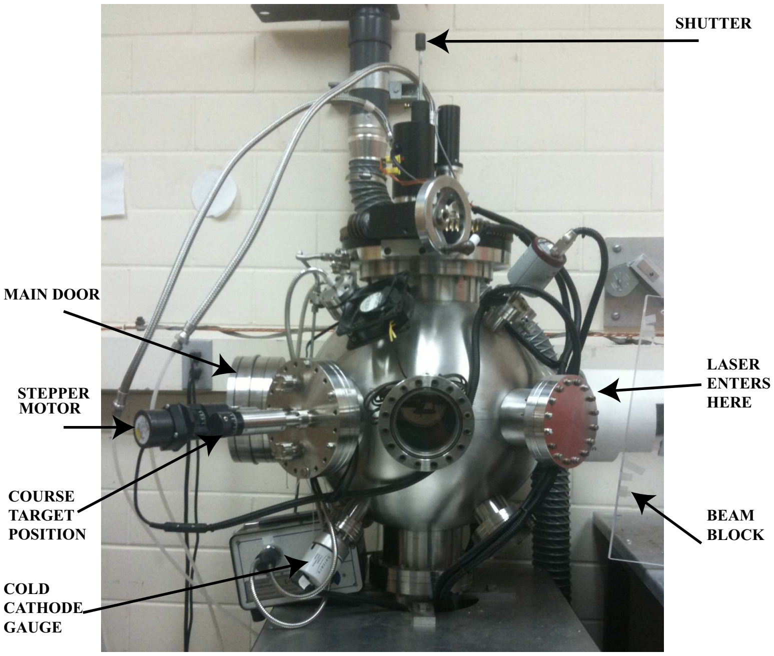

Figure 3.2: This picture shows the main components of the deposition chamber.

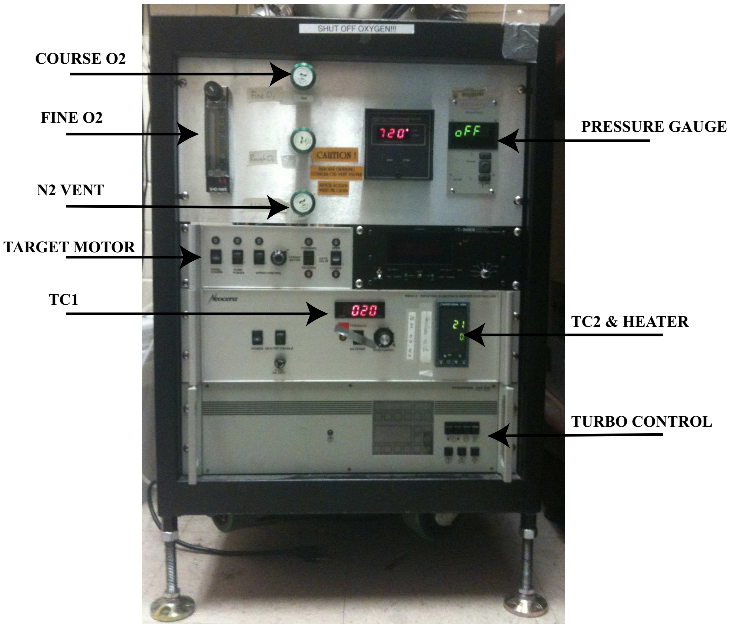

Figure 3.3: This picture shows the front panel of the deposition chamber that controls the following: diaphragm pump, turbo pump, pressure gauges, heater, target motor, gas flow into the chamber, and temperature gauges.

The front panel of the deposition chamber controls the gas flow, heater, pressure gauges, temperature gauges, vacuum pumps, gate valve, and target motor. First, the Vaccubrand GMBH model MD-4T diaphragm pump, which backs the Pfeiffer DCP 600 turbo molecular pump, is turned on with the gate valve in the open position[1]. After the diaphragm pump reaches its base pressure of 4 Torr, the turbo pump can be turned on. The turbo pump will automatically ramp to full speed (100%) unless the speed control switch on the front panel is turned on. Gas flow into the chamber is controlled using a series of valves and can be fine tuned using the flow meter on the front panel. The target is attached to a set of gears on the inside of the chamber, which connect to both a rotating stepper motor and a manual course positioner on the outside of the chamber. This allows the adjustment of the target position with respect to the incoming laser pulses, as well as providing a means to rotate the target during film growth.

3.2 Substrate heater and temperature measurement

Epitaxial growth of perovskite oxides depends critically on oxygen partial pressure, the temperature of the heated substrate, and laser pulse energy and rate. Oxygen environments are not ideal for typical heating elements like tungsten, and thus, a custom designed and built substrate heater assem-

---

[1] The pneumatic gate valve is controlled by a switch on the front panel and requires high pressure nitrogen gas to operate. It is a finicky valve and is always kept in the open position; however, if the panel power is turned off, it will close and can take multiple attempts to re-open.

bly was created in order to reach the growth temperatures necessary for our experiments. The original heater heated the substrates via radiation from a large AerOrod coil heater; however, substrate temperatures were difficult to measure directly due to their transparency and reaching temperatures above 700°C proved to be impossible. Thus, I developed a custom heater assembly, incorporating Kanthal A1 heater wire (an alloy of Cr-Al-Fe) and a boron nitride spool that allows temperatures above 750°C to be easily reached.

The heater consists of five parts, which are diagrammed in Appendix A, and shown in figure 3.4. The heater's main component is a double threaded boron nitride spool that is wrapped with heater wire that connects to a current source controlled by a temperature controller[2]. The temperature controller outputs a current to the heater based on the temperature measured by a thermocouple located near the base of the heater spool (TC1) and according to parameters set by the user (the ramp rate and output limit are the most important values, and are currently set to 0.01 $\%\text{sec}^{-1}$ and 8.5%, respectively). The other components of the heater assembly include a boron nitride cap, which ensures that the heater wire does not short out on the stainless steel outer cap and helps to concentrate the heat from the wire towards the inside of the assembly. The thermal expansion coefficients of stainless steel and boron nitride are quite different, $\alpha = 20\text{x}10^{-6}$ and $0.3\text{x}10^{-6}$ cm/cm/°C,

---

[2] The heater wire is extremely difficult to wrap around the very fragile boron nitride spool, and thus extreme care should be taken when re-wrapping the BN spool with new wire. This is a very tedious process, and if the sidewalls separating the double lead threads are stressed they will break and potentially cause the wire to short.

respectively. Thus, the individual pieces were designed to allow for the larger thermal expansion of the stainless steel components. A stainless steel heater plug that the substrate is silver epoxied to fits into the boron nitride spool and is clamped to the back end of the base plate. The base plate secures to the outer stainless steel shell that holds the rest of the assembly together. This assembly is attached to the support structure in the center of the vacuum chamber that is attached to the top rotating flange, which allows the heater assembly to be rotated 360°.

In order to reach the high temperatures needed for oxide film growth, tests were performed with a variety of different heater wires in order to determine which alloy would survive the high oxygen pressures. The first choice was Nichrome (Ni80 0.015" diameter from Omega), which is a commonly used heater wire used in oxidizing environments that has a maximum operating temperature of 1150°C. This wire burned out at a substrate temperature of 480°C. Larger diameter Ni80 (0.020" diameter) increased the temperature of the substrate to 850°C; however, nickel evaporated from the wire and oxidized, producing a green patina that coated the inner parts of the heater assembly and left a toxic odor inside of the chamber. Platinum 30% wt. rhodium type b thermocouple wire (0.001" diameter), which has a maximum operating temperature of 1700°C, was tried as a last resort due to the extremely high cost ($10 per inch). This PtRh wire allowed us to reach temperatures up to 800°C, but the extremely thin wire did not survive but one temperature ramp. Finally, Kanthal A1 (0.018" diameter) proved to be the wire alloy that allowed the heater to reach the desired temperature and survive multiple temperature cycles. After dozens of depositions the original Kanthal A1 wire is still going strong.

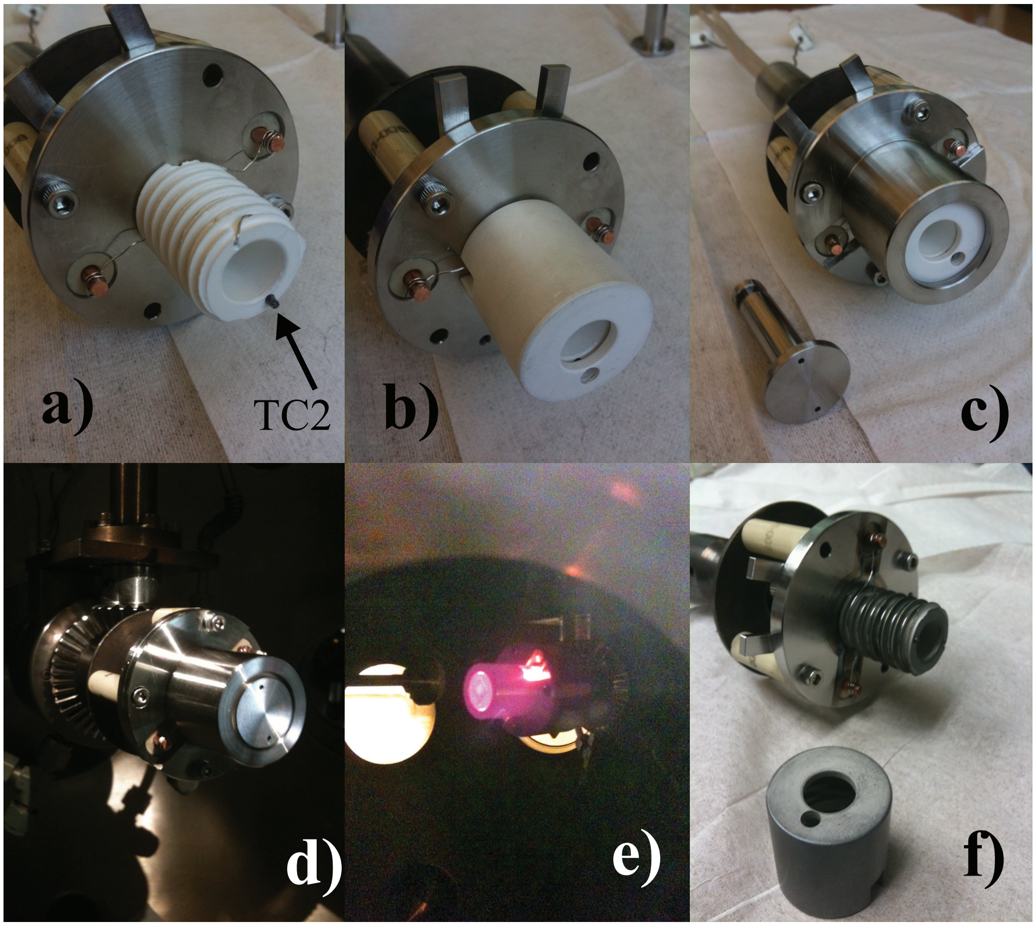

Figure 3.4: These pictures show the substrate heater during different stages of assembly and fully assembled inside of the PLD chamber: a) the Kanthal A1 wire wrapped around the double lead threaded BN spool and secured to large copper wires, as well as the thermocouple closest to the substrate (TC2), which is protruding from the top of the spool, b) the BN spool covered by the BN cap, which ensures that the heater wire does not short on the SS outer cap, c) the fully built heater assembly with the heater plug removed, d) the built assembly inside PLD chamber, e) heater at 750 °C, and f) the heater's worst case scenario after previous attempted use of nicrome wire.

The temperature of the substrate is measured directly using a Mikron Infrared MI-P 140 pyrometer that has a spot size of 1.85 mm at distance of 14 inches away from the substrate. This pyrometer allows for direct measurement of the temperature by measuring the blackbody radiation emitted from the substrate. There are also two thermocouples (TC1 and TC2) which are located inside of the heater assembly, and measure the temperature of the heater at the base (TC1) and the heater plug (TC2). TC1 is located 0.3" from the base of the heater spool, and TC2 protrudes through the top of the heater spool and is in close proximity to the top of the heater plug. These two thermocouples measure temperatures that are typically $50-70°$C higher than the substrate temperature due to the close proximity to the heater wire. The pyrometer is located outside of the vacuum chamber, and thus, proper calibration of the pyrometer was necessary in order to take into account losses due to the vacuum chamber window. Temperature measurements were made with the heater plug and an attached substrate using a box furnace with and without the chamber window [36]. The results of this calibration are shown in figure 3.5, and the temperature of the substrate can thus be determined using

$$T_{acutal} = \frac{T_{measured} + 126°\text{C}(\pm 16.5°\text{C})}{0.947(\pm 0.006)}. \tag{3.1}$$

The temperature of the substrate is most accurately measured using the pyrometer along with equation 3.1. Both TC1 and TC2 will overestimate the actual substrate temperature and are therefore not a good guide for determining the substrate temperature during growth.

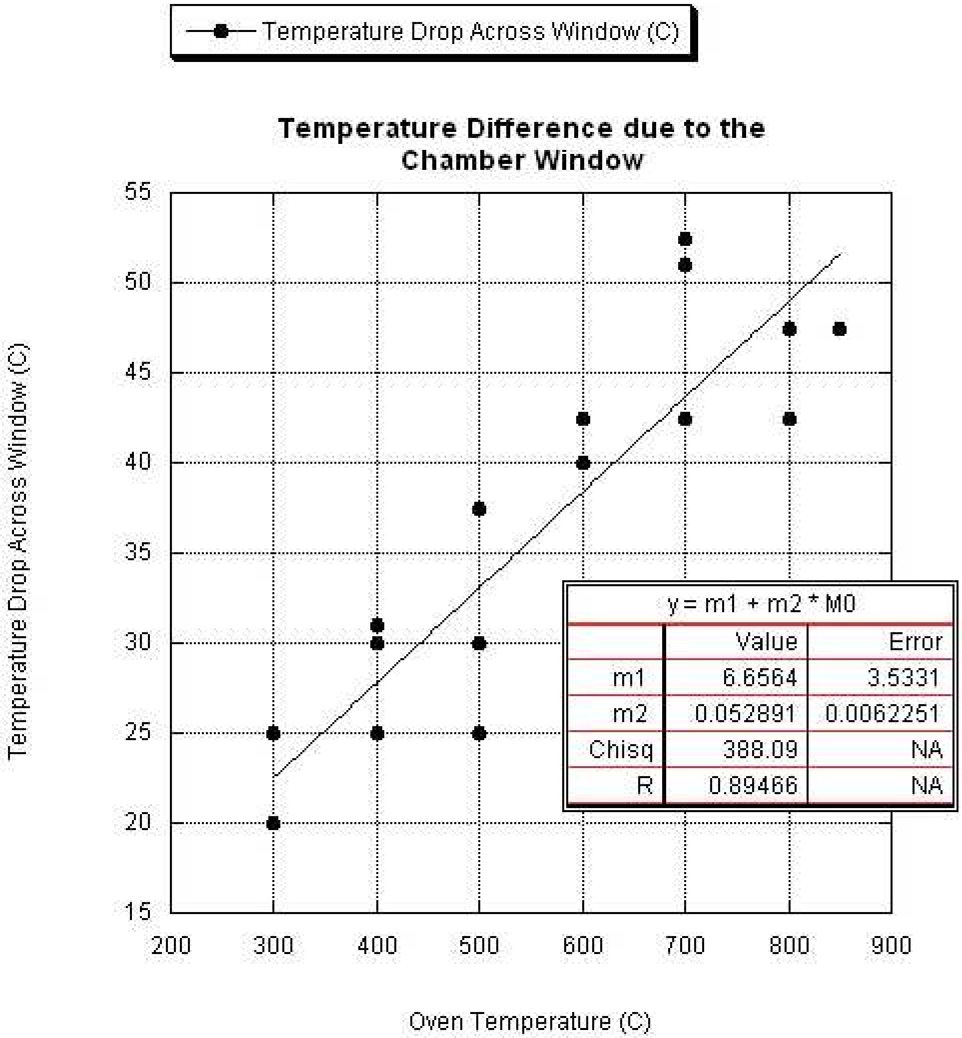

	Value	Error
m1	6.6564	3.5331
m2	0.052891	0.0062251
Chisq	388.09	NA
R	0.89466	NA

Figure 3.5: This figure shows the pyrometer calibration data for the measured temperature drop due to the chamber window.

3.3 Laser Operation

The laser is operated via a handheld keypad that controls both the laser power and pulse repetition, as well as allows the user to fill the laser with new gas. Due to the intense UV light that is produced by the laser, safety measures are in place to ensure that no stray UV light exits either the laser or the PLD chamber, and safety glasses rated specifically for this range of UV are always worn[3]. A large laser pulse, approximately 1.5 x .75 inches, exits the laser and is redirected 50°, using a high energy excimer mirror, towards a 50 cm focal length lens placed 5.5 inches from the chamber window. This laser pulse is focused onto a polycrystalline target at a setting of 238° on the manual target gear control. Prior to depositing a film, the target is pre-ablated for 3 minutes at 100 mJ and a 5 Hz repetition rate with the top flange at an angle of 255° and the shutter completely lowered with the target rotating motor turned on (films are deposited with the top flange at 276° with the shutter raised). The target should be placed in the chamber according to figure 3.6. If the target is not placed in the holder at the correct distance, then the target angle position might need to be adjusted in order to properly ablate the target.

The procedure for operating the laser is posted on the laser and will be briefly summarized here. First, lock both doors, turn on the light to the sign in the hallway (LASER IN USE), and put on the safety glasses rated for the KF laser. Next, insert the key and turn to the right, then turn the main

---

[3] The path of the laser is enclosed in PVC pipe to ensure that no stray radiation escapes.

switch to the right. This will start the warm-up process for the laser, and the laser will perform self diagnostics. After the warm-up is complete, set both the laser power and repetition rate using the handheld key pad. The laser should then be fired into the laser shutter until the laser energy stabilizes near the desired energy. After the laser energy has stabilized, turn off the laser by pressing break (not using the key to turn off power to the laser) and raise the laser shutter by tightening the string on the top of the laser and tying it off on the hooks near the main switch. At this point, pre-ablation can be performed. Pre-ablation creates a smooth dense surfacer free of loose particles in order to ensure a pure atomic plasma during actual deposition. After performing pre-ablation the film can be deposited. An example of the conditions used during film growth will be given in section 4.3.

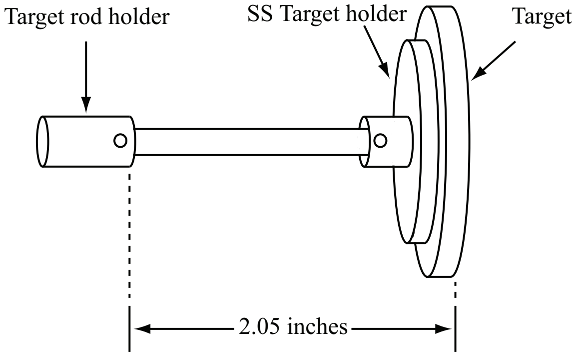

Figure 3.6: This figure shows the position of the target inside of the PLD chamber. The target placed at this position is aligned with the laser beam with the external adjustment set to 238° .

Chapter 4

Substrate preparation and film growth

The creation of epitaxial oxide heterostructures requires the precise control of many parameters, such as substrate quality and termination, polycrystalline target quality, and optimal thin film growth conditions. In order to systematically study the effect of different thin films on STO, it is very important to control all of these conditions to the highest degree of accuracy possible. The procedures to create TiO_2 terminated substrates and grow epitaxial films of various oxides on STO are discussed in detail in this chapter.

4.1 TiO_2 terminated $SrTiO_3$ substrates

The single crystal STO substrates must be chemically etched prior to thin film deposition in order to ensure that the substrate termination layer is solely TiO_2. Substrates come from the manufacturer cut with the correct (001) crystal orientation (normal to the surface) and polished on one side to create a smooth surface for film growth. The quality of substrates depends largely on the miscut angle and the number of dislocations in the crystal [1].

---

[1] The miscut angle refers to the extent to which the (001) direction deviates from the surface normal and is a result of the cutting and polishing procedure performed by the manufacturer.

MTI corporation provides the (001) polished STO substrates that are used in this work, but MTI only guarantees a miscut angle less than 0.5°. Typical miscut angles vary between 0.1−0.3°, where lower values correspond to higher quality substrates.

We performed a systematic study of the etch process to optimize the quality of the TiO_2 termination and the reproducibility of the etch procedure. We studied the effects of three different etchants: two different buffered oxide etchants of $HF:NH_4F$ (BOE 6:1 from J.T. Baker and BOE 10:1 from KMG chemicals) and aqua regia, a 3:1 mixture of $HCl:HNO_3$, as a function of etch time. Buffered HF and aqua regia have both been shown to successfully create TiO_2 termination of STO substrates; however, BOE 10:1 has not been studied [37, 38]. Substrates etched using both the BOE 6:1 and aqua regia were initially ultrasonically agitated in 60°C deionized water, then chemically etched, rinsed, and finally annealed in oxygen at 900°C [37, 39]. BOE 6:1 etch times ranged from 15−90 s while the less aggressive aqua regia etch times ranged from 60−900 s. For these two etchants our best etches occurred for etch times of 60 s for BOE 6:1 and 300 s for aqua regia. Although both the BOE 6:1 and aqua regia etchants were able to create the desired TiO_2 terminated substrates, high quality results were not reproducible. Thus, a third etchant, BOE 10:1, as well as an altered etch procedure, were studied. Substrates were first cleaned by a three step process in an ultrasonic agitator first using isopropanol, then acetone, and then isopropanol for 15 minutes each prior to the formation of Sr-hydroxide on the SrO terminated areas by agitating in 60°C deionized water. We then annealed the etched substrates in oxygen at 950°C for four hours. The BOE 10:1 etch for 60 s, three step cleaning procedure, and higher temperature anneal consistently produced high quality TiO_2 terminated substrates. Although the BOE 6:1 produced higher quality substrate etches than aqua regia, the procedure was not highly reproducible due to the formation of deep etch pits. The aqua regia etches did not create etch pits; however, they also did not create the clean terrace structure observed in the BOE 6:1 etches. Substrates etched using BOE 10:1 did not have etch pits and showed clean unit cell steps between flat, defect-free terraces.

4.1.1 Characterization using AFM

The etched substrates are characterized by atomic force microscopy (AFM) to determine the quality of the substrate prior to thin film deposition. Substrate quality varies due to both batch quality from the distributor and on the miscut angle. The miscut angle varies drastically from substrate to substrate, ranging anywhere from 0.1 to 0.5°. MTI guarantees a substrate miscut of ±0.5°, so it is hit or miss when it comes to getting low miscut angles. Unfortunately, substrate quality decreases with increasing miscut angle, and for very large miscut angles, stacking occurs, where the step size between terraces becomes larger than one unit cell.

All substrates are analyzed by AFM after the TiO_2 termination procedure is completed. If AFM reveals unit cell steps between terraces, then it is concluded that the etch procedure has produced TiO_2 termination. We do not perform any measurements on the substrates to determine the chemical stoichiometry of the termination layer, but it has been shown by Lateral Force Microscopy (LFM) and by coaxial impact-collision ion scattering spectroscopy that substrates treated by similar etching methods that show a clean terrace structure are indeed TiO_2 terminated [39, 40]. Many substrates do not have an ideal terrace structure due to miscut during the cutting and polishing procedure; however, some of these substrates are still able to produce conducing interfaces[2].

The following figures show AFM images of etched substrates using each of the etchants described in the previous section, as well as an AFM image of an STO substrate with a large miscut angle that shows a very jagged terrace structure.

---

[2] The effect of substrate dislocations on the electronic transport properties in the LAO/STO system has been studied in detail by Thiel [41, 42].

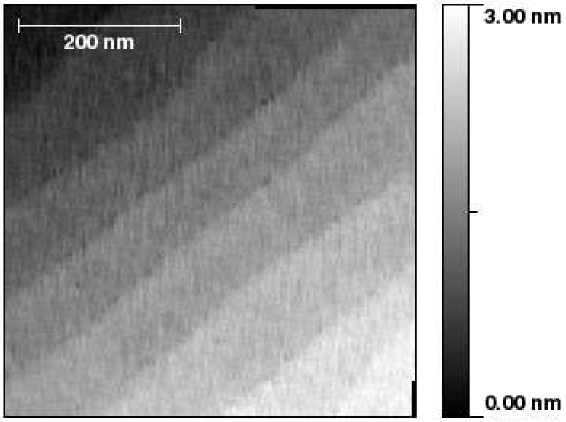

Figure 4.1: An atomic force micrograph of a BOE 6:1 (60 s) etched substrate.

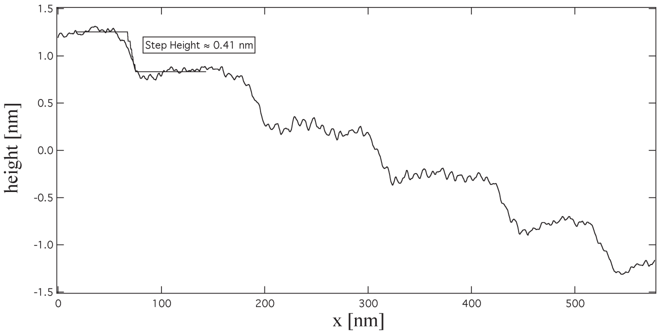

Figure 4.2: A line scan taken perpendicular to the terraces (BOE 6:1 60 s) that verifies the unit cell step size between terraces, indicating single termination.

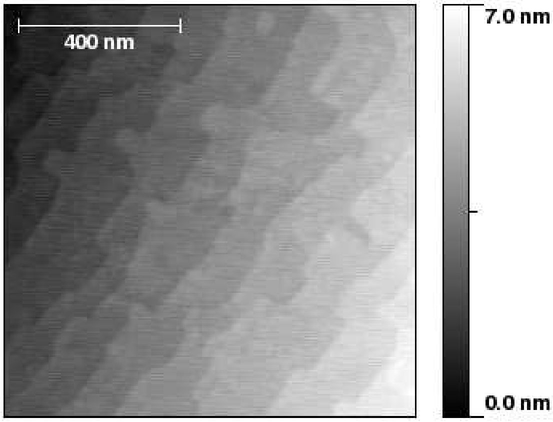

Figure 4.3: An AFM image of an STO substrate after a 300 s aqua regia etch.

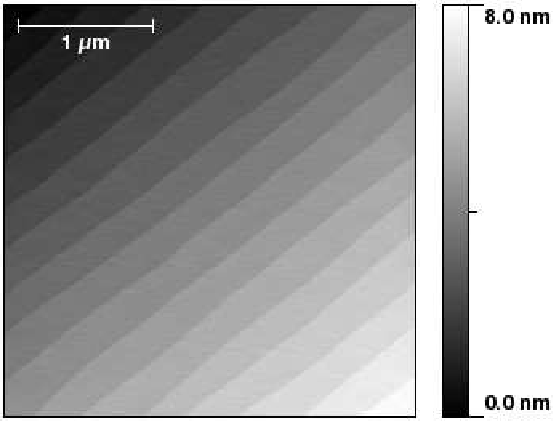

Figure 4.4: An STO substrate after a 60 s BOE 10:1 etch that displays unit cell step height between terraces that are separated by roughly 250 nm (corresponding to a miscut angle of 0.1°)

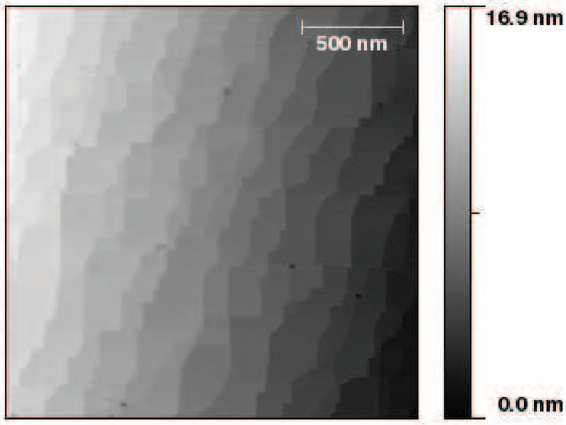

Figure 4.5: This substrate was etched using the BOE 10:1 procedure, but has jagged terrace edges which may be due to a large miscut angle where the terraces are only separated by roughly 100 nm (corresponding to a miscut angle of 0.5°).

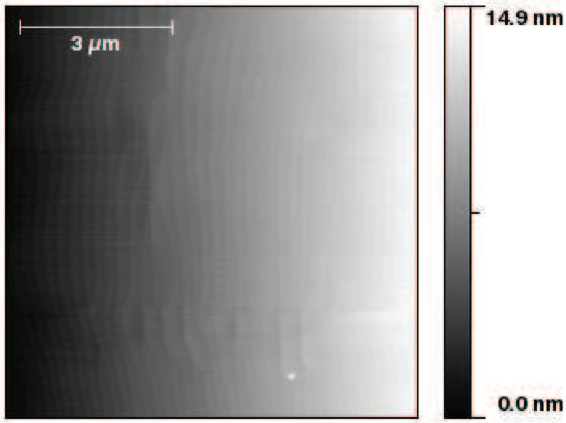

Figure 4.6: This etched and annealed STO substrate shows a very smooth step structure but has a visible edge dislocation.

4.2 Target synthesis using solid state reaction

Targets for use in the PLD system are made using solid state reactions. The stoichiometric target should be dense, without loose, small particles that might be ejected during ablation. Once this is achieved, crystalline films can be created by ablating the target with the pulsed excimer laser.

High purity oxide powders are weighed and then individually dried in alumina crucibles in a 900°C furnace overnight to burn off any carbonates. After the initial drying step, the exact ratio of oxides is calculated and weighed precisely to create a stoichiometric ratio for each ABO_3 perovskite thin film. These oxides are then combined into a large alumina crucible where they are dried in the 900°C furnace in between grindings of the mixture using a mortar and pestle to create a homogenous, fine powder. The process of grinding and drying is repeated three times and then the powder is pressed into a pellet using a hydraulic press to create a dense disc. For our 1.25" diameter pellet, a pressing of 12000 lbs, corresponding to a pressure of 66 MPa is used. At this point in the process, the pellet is extremely fragile and is removed from the press with care and placed into a clean alumina crucible that is placed into a high temperature furnace. For aluminates and gallates the pellet is then sintered at 1450°C for 8 hours, which creates a polycrystalline dense pellet that can be used to create stoichiometric crystalline thin films. A very important part of this process is the final sintering step, where the target becomes a very dense material. If the target does not form a very solid pellet after the initial sintering step, and a powdery material can be easily removed from the surface, then subsequent sintering steps at higher temperatures may be necessary. The melting point of most of these oxides is near 1700°C, so application of higher temperatures will not melt the pellet[3]. Using this method polycrystalline targets of the following materials have been made: $LaAlO_3$, $LaGaO_3$, $LaTiO_3$, $KNbO_3$, $NaTaO_3$, $YAlO_3$, $CeAlO_3$, $PrAlO_3$, $NdAlO_3$, $SmAlO_3$, $EuAlO_3$, $GdAlO_3$, $TbAlO_3$, $La_{0.75}Eu_{0.25}AlO_3$, and $Y_{0.6}La_{0.4}O_3$.

---

[3] The high temperature box furnace has a upper limit of 1500°C and the lifetime of the furnace is decreased significantly if it operated at its maximum temperature. Thus, sintering is performed at the highest practical temperature, which in the case of most of the oxide perovskites in this work is near 1450°C.

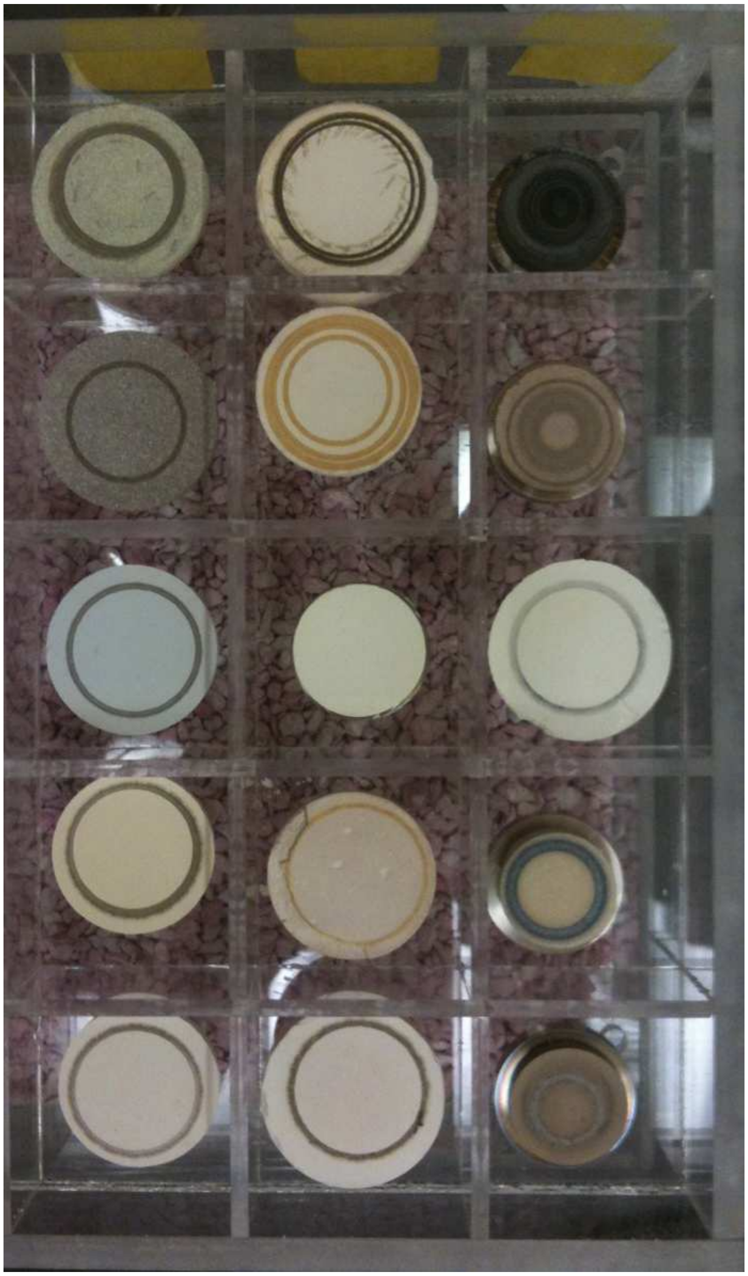

Figure 4.7: Some of the PLD targets that were made using solid state reactions. The rings that can be seen on the surface are where the laser pulse hits the rotating targets.

4.3 Film growth using PLD

Typically, an ABO_3 target is ablated using a laser fluence of 1.5−3 J/cm^2 or lower and a pulse repetition of 2−5 Hz under 0.5 mTorr oxygen pressure in a chamber with a base pressure of 7 x 10^{-7} Torr. This high energy packet of photons heats the surface of a polycrystalline target, evaporating the surface atoms and creating a plasma plume of the target material. This plume is directed onto a heated substrate where the atoms inside the laser plume bond to the substrate's termination layer. If the temperature of the substrate, partial pressure of oxygen in the chamber, and laser power (equivalent to the plume intensity or flux of target material) are all correct, then the atoms in the plume will bond to the substrates termination layer forming an epitaxial single crystal thin film.

The quality of epitaxial film growth is highly dependent on the deposition conditions used in the PLD process. Figure 4.8 illustrates the different growth modes that can occur under various substrate and deposition conditions. If there is strong bonding between the substrate and the film, the total surface energy, $\gamma_I + \gamma_F$, is lower than the bare substrate surface energy, γ_S. Under these conditions, layer-by-layer, Volmer-Weber, and step flow growth modes are possible. If there is no bonding between the substrate and the film, then the total surface energy would increase if the film were to wet the substrate, and hence islands are formed.

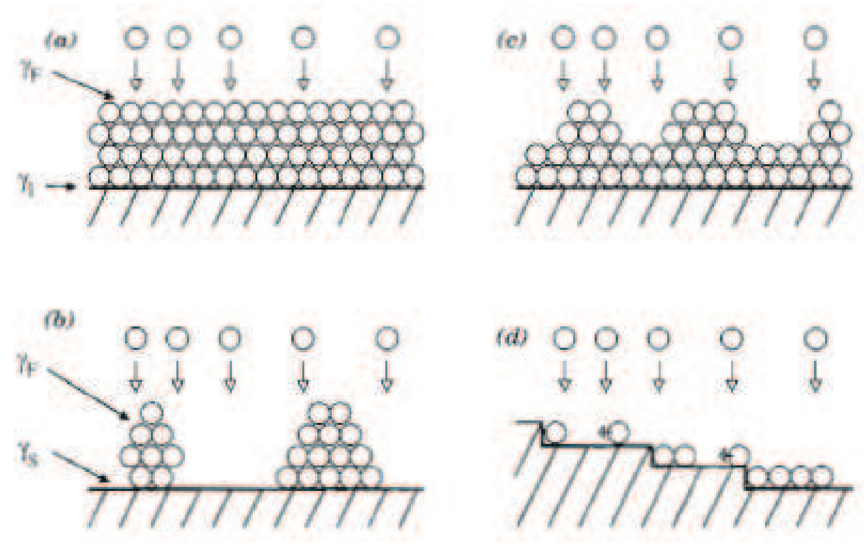

Figure 4.8: Four different film growth modes are illustrated, where the free energies of the film surface (γ_F), substrate surface (γ_S), and the interface between film and substrate (γ_I) are used to determine which growth mode will dominate. The different growth modes are: a) layer-by-layer (Frank-Van der Merwe), b) Volmer-Weber, c) Stranski-Krastanov, and d) step flow. Plot taken from Ref. [43].

4.3.1 Characterization using AFM and XRD

After film deposition, both X-ray diffraction (XRD) and AFM are used to characterize the thin film. AFM confirms that the thin film maintains the original terrace structure of the substrate and therefore indicates layer-by-layer growth. XRD is used to determine the quality of the epitaxial films by performing both $\theta - 2\theta$ and θ-rocking scans. The initial characterization of the thin films determines if the growth conditions used in the PLD process are optimized. The following AFM scans highlight the different types of growth that have been observed for various oxide perovskites on STO.

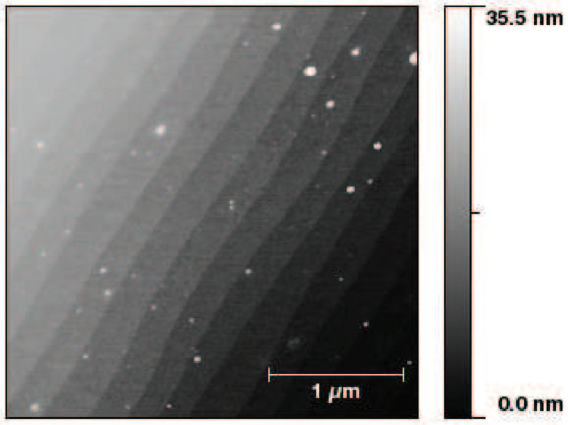

Figure 4.9: Step flow growth can be seen for this film of LAO on STO, because the original terrace structure of the STO substrate remains visible after film deposition.

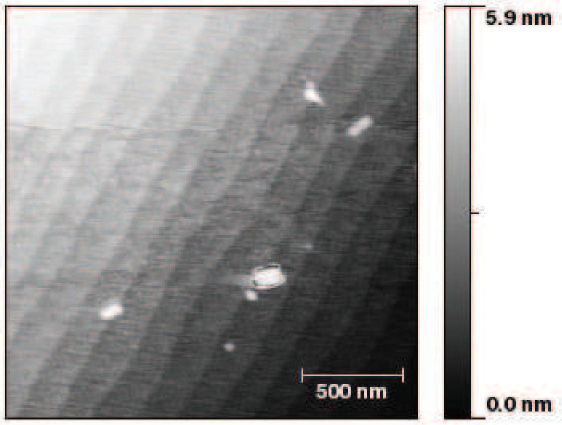

Figure 4.10: This film of $PrAlO_3$ (PAO) on STO indicates good step flow growth and also shows a few nucleation points that could have occurred due to a substrate defects.

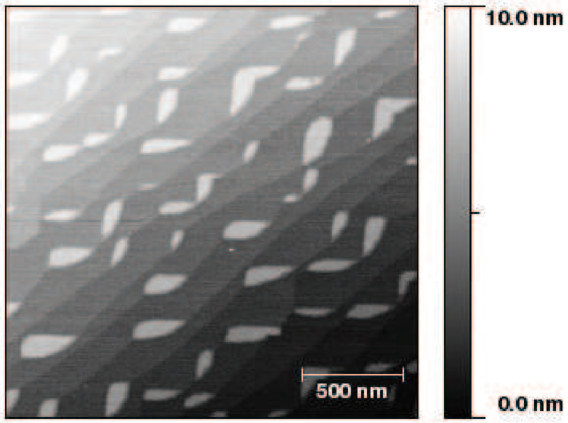

Figure 4.11: This AFM scan of PAO on STO has a very repeated raised image that is indicative of a possible tip error.

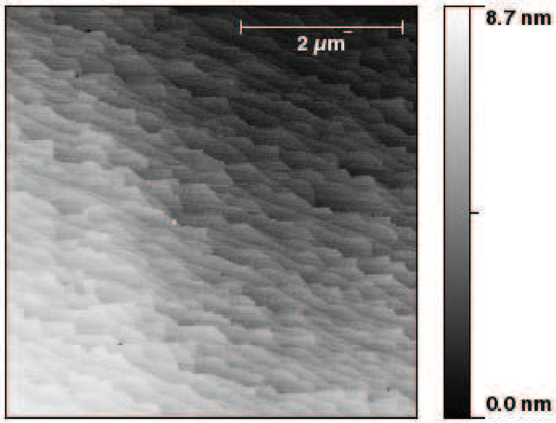

Figure 4.12: An AFM scan of $TbAlO_3$ (TAO) shows that even a non-ideal substrate can produce layer-by-layer growth

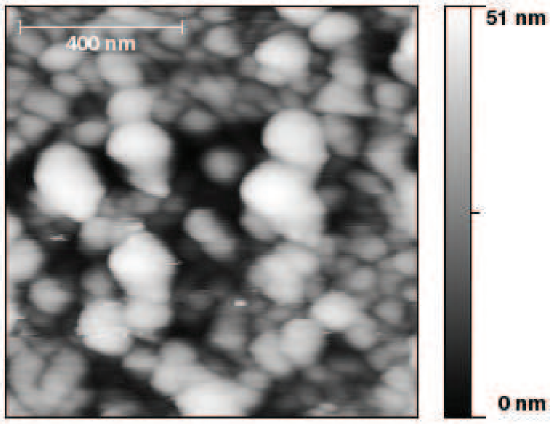

Figure 4.13: AFM scans of $KNbO_3$ never revealed layer-by-layer growth, and various deposition conditions always produced islands.

The previous AFM scans illustrated various types of growth that can occur using PLD. The growth conditions that have been highly successful in creating layer-by-layer or step flow growth of the oxides in this study are the following: 50 mJ laser energy, 2 Hz repetition rate, 1 x 10^{-3} Torr O_2, and a substrate temperature of 760°C. The raised specs that are visible in the some of the AFM scans are unknown in origin but could possibly be due to nucleation around a substrate defect. It should also be highlighted that the AFM image can include artifacts from the interaction of the cantilever tip with the sample. If there is a defect on the tip of the AFM cantilever, it can often be seen as a repeated image in the AFM scan, as in figure 4.11.

XRD is performed using a Bruker-Nonius powder diffractometer, where the diffracted x-rays indicate the crystallinity of both the substrate and the thin film. Incident x-rays diffract from the lattice planes of the crystal and produce constructive interference according to Bragg's law:

$$n\lambda = 2d\sin\theta, \tag{4.1}$$

where λ is the wavelength of the incident radiation ($\lambda = 1.5417$ Å), n refers to which planes are responsible for the diffraction, d is the crystal plane spacing, and θ is the angle of the incident x-ray. A typical XRD scan is referred to as a $\theta - 2\theta$ scan in which the sample plane is rotated by θ while the diffracted x-rays are collected at an angle 2θ. This type of XRD scan shows the presence of crystalline peaks such as the (001) (n=1), (002) (n=2), and (003) (n =3) peaks of both the substrate and the film.

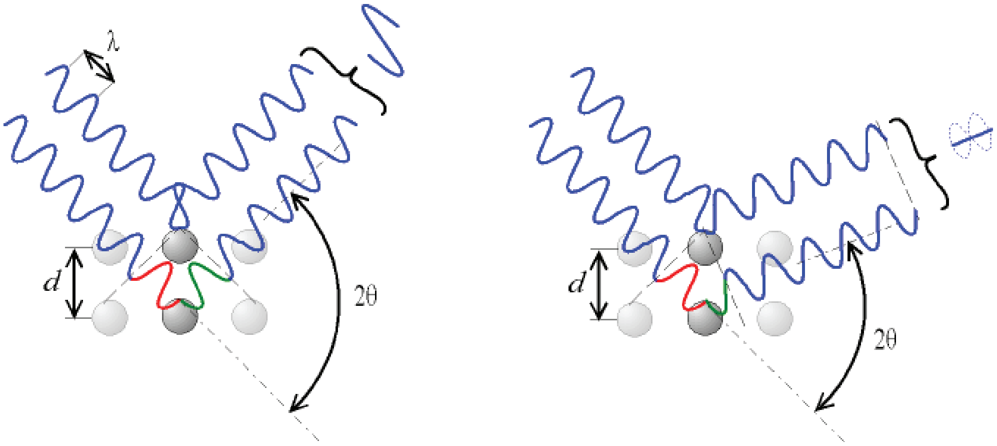

Figure 4.14: This image shows both the constructive and destructive interference that can occur due to diffraction of incident x-rays with a crystal lattice. Image taken from Ref. [44]

As an example of the XRD characterization typically performed on a thin film, consider the case of LAO/STO. The LAO film has a bulk lattice constant of 3.778 Å, which is under tensile strain on the larger 3.905 Å STO lattice. Using an XRD $\theta - 2\theta$ scan, we have directly observed the in-plane lattice constant of the LAO film to be 3.78 Å (exactly that of the bulk). Thus, for this particular film, the tensile strain at the interface is not present in the entire film, or in other words, the lattice relaxes back to the bulk crystal phase at some short distance from the interface, so that the relaxed lattice dominates in the x-ray diffraction data.

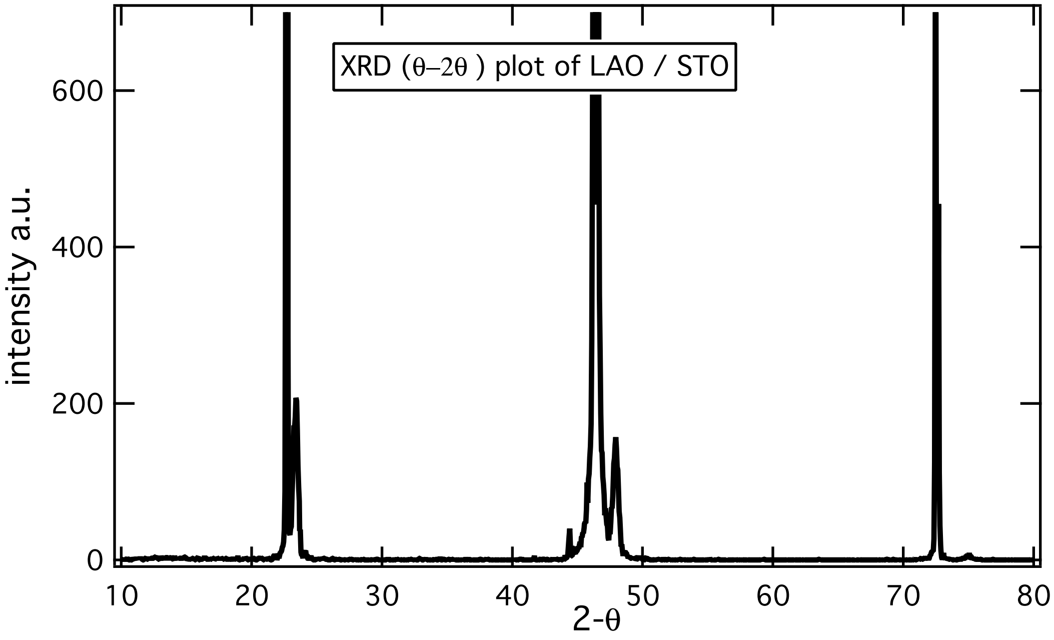

Figure 4.15: This XRD plot shows both the large substrate peaks as well as the film peaks

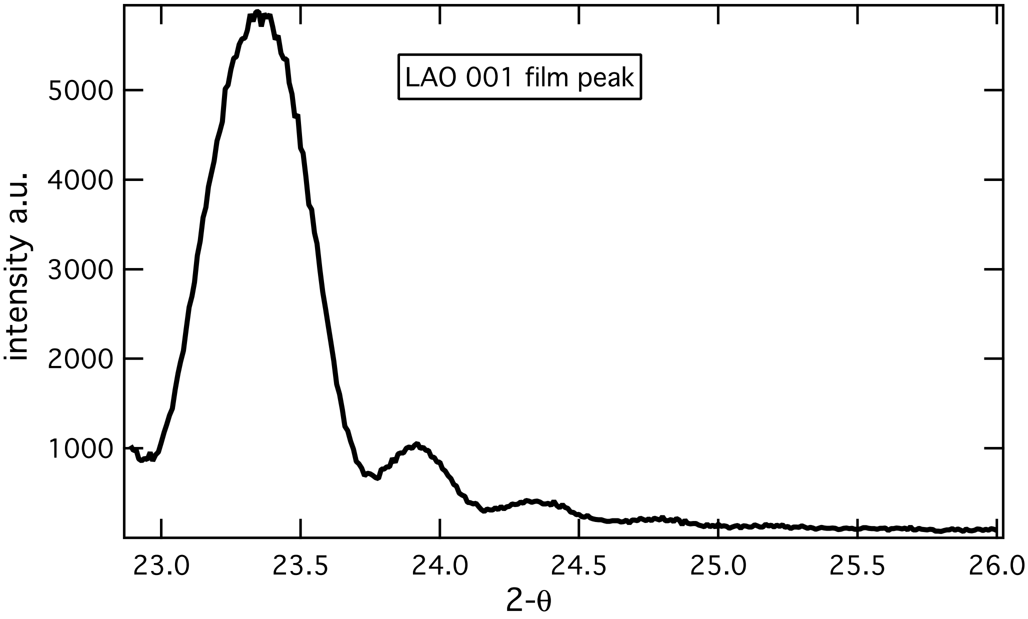

Figure 4.16: This XRD plot shows the (001) film peak of LAO, which indicates film thickness due to the coherent oscillations that are a result of a very smooth flat film.

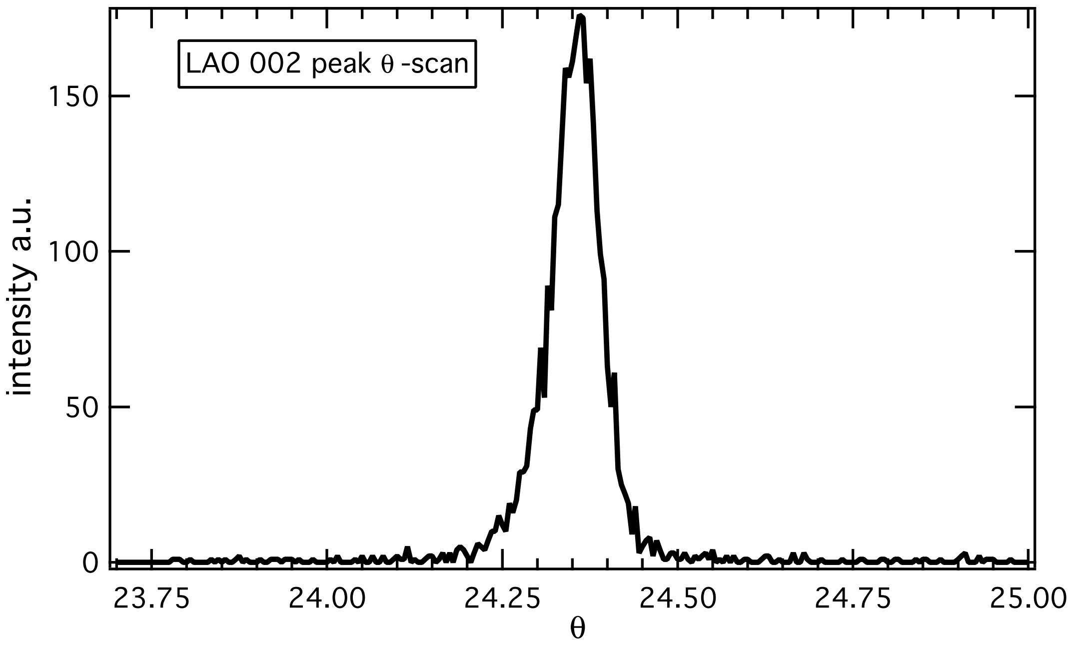

Figure 4.17: This XRD plot shows a rocking curve that is centered around the (002) peak of an LAO film. The FWHM of this rocking curve is 0.08°, indicating that the film is highly aligned with the substrate.

An expanded view of the (001) LAO peak, shown in figure 4.16, allows us to calculate the film thickness, t, using the relation

$$t = \lambda / \cos\theta\delta\theta, \tag{4.2}$$

where θ is the main peak position, $\delta\theta$ is the angular period of the oscillations in radians, and λ is the wavelength of the XRD radiation source; according to this equation, the film in figure 4.16 has a thickness of 26.3 nm. All films with thicknesses between 19−28 nm had XRD 00l peaks at angles identical to that of bulk single crystal LAO. However, films with thicknesses between 8-12 nm had c axis lattice constants of 3.76 Å, a 0.5 % decrease from the bulk. The tensile strain at the interface causes each thin film to shrink along the (001) direction; this strain persists through the films but does relax back to the bulk lattice as the film thickness increases. The FWHM of a rocking curve (or θ scan) is an indicator of how well the thin film is aligned with the substrate. Rocking curves of deposited films exhibit FWHM as small as 0.08° (see figure 4.17) that demonstrates high quality epitaxial growth of LAO.

A characterization of thin films using XRD can be tricky due to misalignment of the substrate. If the XRD's θ value is not carefully adjusted for each scan, then small alignment errors from the substrate holder can cause diffraction peaks to be completely skipped over. The substrate peaks are well defined by Bragg's law and thus can be used to align the θ value of the diffractometer by performing a rocking curve on a substrate peak (known 2θ

position) and then adjusting the value of θ (sometimes referred to as the ZI value of the diffractometer). If the alignment is off, then the rocking curve peak will appear at an angle θ, which is not equal to the calculated and fixed value of $2\theta/2$. Another difficulty in using XRD to verify epitaxial growth is the large response of the substrate. This large signal can cause the detector to overload, which can wash out the small signal of the film peak. In order to see the film peaks, the current and voltage settings for the x-ray source need to be adjusted so that the signal from the substrate does not overload the detector (different size slits can also be placed in front of the detector to cut down on the x-ray intensity).

Chapter 5

Electronic transport: the van der Pauw method

Electronic transport properties such as resistivity and mobility provide a means to distinguish between different classes of materials. These measurements can separate crystals into various classifications such as semiconductors, metals, and band insulators, and they can provide an inside look into the detailed band structures that comprise complex heterostrucures. The following chapter describes the basic concepts behind both resistivity and the Hall effect, as well as the van der Pauw configuration that is used to make these measurements.

5.1 Resistivity

The word resistance indicates an opposition to flow, and it can be used to describe many physical phenomena. With respect to condensed matter, electrical resistance refers to how strongly a material opposes the flow of electric current, where a high opposition corresponds to insulators and a low opposition refers to conductors. The resistivity of a material, ρ, is the inverse of the conductivity, σ, which is a measure of the material's ability to pass an electric current. In order for a current to flow through a material, an electric field must be present. The force on an electron in an electric field **E** is given by

$$\mathbf{F} = m\frac{d\mathbf{v_d}}{dt} = -e\mathbf{E}. \tag{5.1}$$

Thus, the average, or drift velocity is

$$\mathbf{v_d} = \frac{e\mathbf{E}\tau}{m}, \tag{5.2}$$

where τ is the average collision time. The current density j for a volume density n of electrons is related to the drift velocity by

$$\mathbf{j} = -ne\mathbf{v_d}, \tag{5.3}$$

and using equation 5.2, the current density becomes

$$\mathbf{j} = \frac{ne^2\tau\mathbf{E}}{m}. \tag{5.4}$$

Conductivity is the proportionality factor that relates the current density to the electric field; therefore,

$$\mathbf{j} = \sigma\mathbf{E} = \frac{\mathbf{E}}{\rho}. \tag{5.5}$$

Now we can obtain an expression for the resistivity as a function of the collision time, so that

$$\rho = \frac{1}{\sigma} = \frac{m}{ne^2\tau}. \tag{5.6}$$

It is evident that for a long collision time the resistivity is small and the conductivity is large. Hence, materials where electrons can travel unimpeded for long times are good conductors, have low resistivities, and high conductivities. The two main scattering phenomena that reduce the collision time are lattice phonons and impurities or defects. As the temperature of a material is decreased, the effect of lattice phonons decreases, and at 0 K the extrapolated resistance is purely due to impurities or defects. Electrons are not scattered by the ion cores in a lattice but, rather, by the change in the periodicity of the lattice due to thermal vibrations (high temperatures) or by defects and impurities (low temperatures) [45].

Using Poisson's equation on the electric field in equation 5.5 we can show that

$$\frac{I}{A} = \frac{V}{\rho l}, \tag{5.7}$$

where we are considering a rectangular slab of material of cross-sectional area A (the dimensions are shown in figure 5.1). The voltage V that develops along the length, l, leads to the expression

$$V = I\frac{\rho l}{A}. \tag{5.8}$$

The resistance of the sample can now be defined in terms of the resistivity, ρ, the length and the area, so that

$$R = \rho\frac{l}{A}. \tag{5.9}$$

The previous two equations lead to the well known Ohm's law

$$V = IR. \tag{5.10}$$

The resistivity of a material is determined using Ohm's law, where a known current is passed through a sample, and the voltage developed between two points is measured. The resistance of thin films is often reported as the sheet resistance, R_s. If the thin film is of thickness d, and the area is written as the product of the width times the thickness, $A = wd$, then the sheet resistance, R_s, is defined by

$$R = \rho\frac{l}{wd} = R_s\frac{l}{w}, \tag{5.11}$$

that is, $R_s = \rho/d$. The sheet resistance is often written in units of $\Omega/\square$, which is dimensionally equal to Ω, and is called such because a square sheet with $R_s = 1\ \Omega$ has $R = 1\ \Omega$; this definition avoids any confusion with bulk resistance.

5.2 Hall effect

The Hall effect measures a transverse voltage that develops due to a current in a magnetic field. It is a very useful measurement technique that allows determination of both carrier concentration and mobility. Consider figure 5.1, in which a current is passed through a thin sheet with a magnetic field normal to the surface. The force on the current is given by

$$\mathbf{F} = ev_d\mathbf{B} = \frac{I\mathbf{B}}{nA}, \tag{5.12}$$

since the current is equal to

$$I = neA\mathbf{v_d}, \tag{5.13}$$

where n is the carrier concentration. Equilibrium is established once the force of the generated electric field equally opposes the force of the magnetic field. The electric field produced is equal to

$$\mathbf{F_E} = e\mathbf{E} = \frac{eV_H}{w}, \tag{5.14}$$

where V_H is the Hall voltage and w is the width of the sheet. Thus, at equilibrium

$$\frac{I\mathbf{B}}{nA} = \frac{eV_H}{w}, \tag{5.15}$$

which leads to the sheet carrier density

$$n_s = \frac{I\mathbf{B}}{eV_H}. \tag{5.16}$$

The sheet carrier density is the carrier concentration, n, times the thickness of the conducting sheet. This is a more useful quantity when referring to quasi-2DEGs, where the thickness of the charged sheet is uncertain. The mobility, μ, is the proportionality constant that relates the electric field to the drift velocity; thus,

$$\mu = \frac{1}{n_s e R_s}. \tag{5.17}$$

The mobility characterizes how quickly the charge carriers move in a material due to an electric field. The mobility is temperature dependent, similar to the collision time, where a decrease in T increases the mobility by reducing phonon scattering. Another often used parameter for the Hall effect is called the Hall coefficient, R_H, where

$$R_H = -\frac{1}{ne}. \tag{5.18}$$

This parameter is often reported because it is a measure of the carrier concentration (R_H should not be confused with the Hall resistance).

In order to accurately measure the Hall voltage, V_H, it is necessary to perform the Hall effect for both positive and negative magnetic fields. This is required because there is always an offset that is present due to the location of the contacts. This offset can be subtracted out if the measurement is performed at both positive and negative fields.

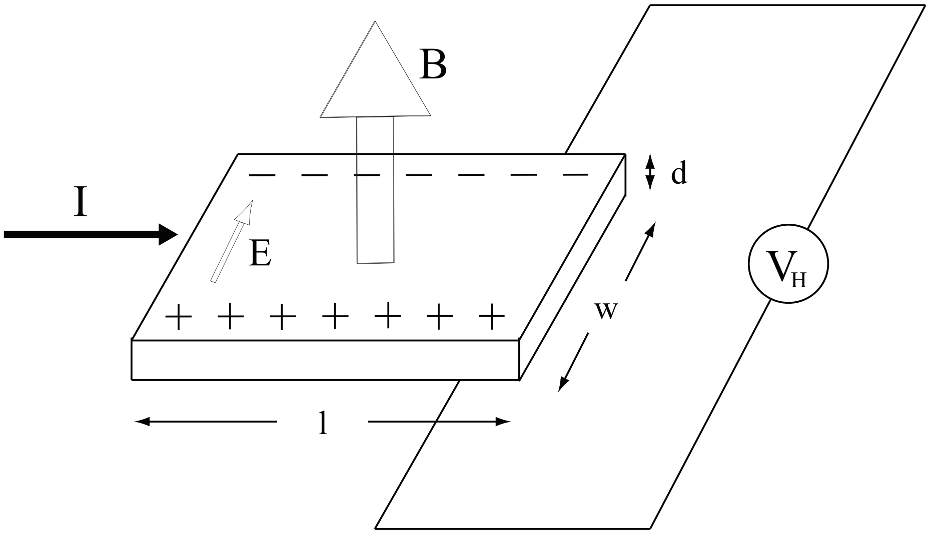

Figure 5.1: This diagram illustrates the Hall effect for a thin slab.

5.3 Resistance measurement techniques

Measurement of sheet resistance is a seemingly simple experiment to perform, and there are many different techniques available to measure this property. All precision resistance measurement techniques utilize four wires, so that the resistance of the wires in the measurement device does not contribute to the sample resistance. However, the arrangement of the wires differs for the two main methods used for measuring resistance. In this section, both the linear four probe method and the van der Pauw method will be discussed in detail.

5.3.1 Four terminal method

The most common way to measure sheet resistance, R_s, is called the four terminal or Kelvin probe technique, which uses two force leads to send current and two sense leads to measure voltage. This technique has the advantage over an ohmmeter, which only uses two wires, in that is does not include the resistance of the current carrying wires in the overall sample resistance measured. The typical four terminal measurement circuit diagram is shown in figure 5.2. A known current is passed through $R_{subject}$, and the voltage developed across it is measured using a voltmeter. A voltmeter is a high impedance device and uses extremely small currents to measure voltage drops, and thus, the voltage developed along R_{wire} in the voltage leads is negligible. The most typical four terminal measurement technique is performed with four contacts along a line, as shown in figure 5.3. The downside to this measurement is that the position of the contacts on the sample significantly affects measurement accuracy. This linear configuration can lead to an accurate measurement of R_s, but careful measurements of the sample size, and the contact positions must be made in order to minimize errors. For a rectangular sample, the resistivity can be calculated using the following formula:

$$\rho_s = \frac{V 2\pi L}{I \ln 4}, \tag{5.19}$$

where V is the voltage measured between the two inner leads, I is the current sent between the outer leads, and L is a correction factor that depends on the sample size and positions of the leads (L is a function of a/d and d/s, for a sample where all contacts are equally spaced by s and has the dimensions shown in figure 5.3) [1].

5.3.2 van der Pauw method for measuring resistance

The van der Pauw method (VDP) is an improvement over the linear four terminal technique, that allows for reproducible measurements of R_s without taking into account details of sample geometry or contact placement [49, 50, 51]. The VDP technique uses four probes but positions the probes at the perimeter of the sample. As long as the sample is of uniform thickness, flat, singly connected (i.e., no physical holes), and the contacts are small and at the sample perimeter, then R_s can be calculated without knowledge

---

[1] Tables of L can be found for various aspect ratios of rectangular samples in reference [46, 47, 48].

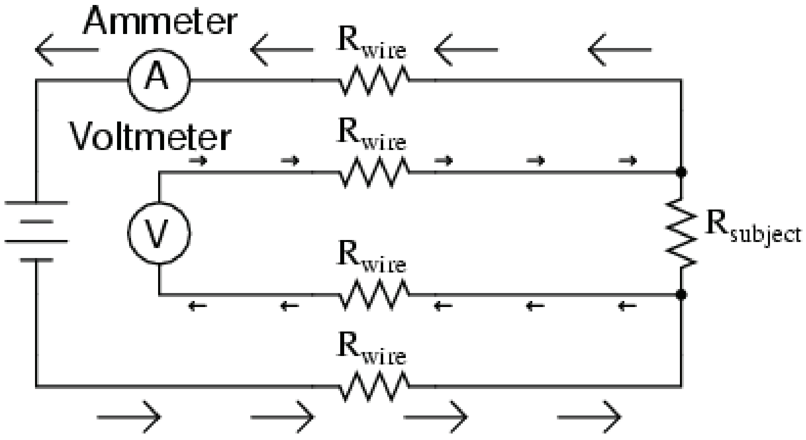

Figure 5.2: In this four terminal configuration the resistance of the voltage sensing wires is negligible due to the high impedance of the voltmeter.

of the sample size or contact separations. This technique offers a reliable way to reproducibly measure sheet resistance without having to perform detailed measurements for error anaysis.

Consider a sample of thickness d with an arbitrary shape extending to infinity in all directions, as shown in figure 5.4. The following derivation for sheet resistance, using the van der Pauw configuration, assumes that the sample is flat, uniformly thick, the contacts are small and there are no physical holes [52]. If a current, $2i$, is injected into a point M on the surface of the sample, then it will flow radially away from M into infinity. The current density at a point r away from M is

$$J = \frac{2i}{2\pi r d}. \tag{5.20}$$

The current density, J, is equal to σE; thus,

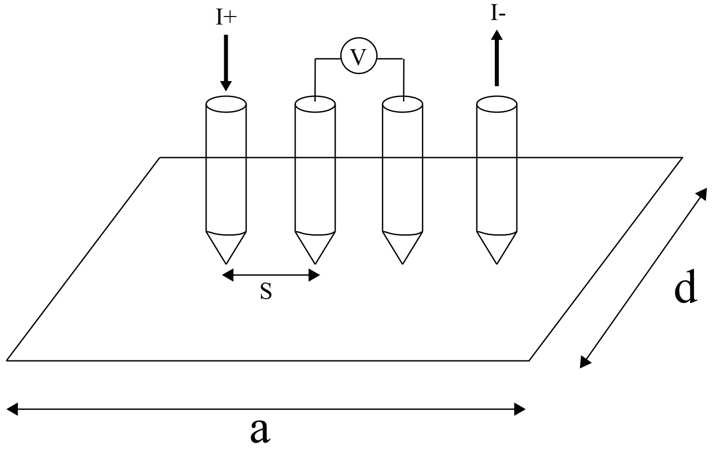

Figure 5.3: The typical arrangement of contacts on the surface of a sample for the linear four terminal measurement.

$$E = \frac{\rho i}{\pi r d}. \tag{5.21}$$

The electric potential developed at points N, O and P due to charge insertion at M can be determined using Poisson's equation. For example, the potential between points O and P is

$$V_P - V_O = \int_P^O E dr = \frac{\rho i}{\pi d} \int_P^O \frac{dr}{r}, \tag{5.22}$$

where the distances between points is shown in figure 5.5. This leads to the following potential between points P and O:

$$V_{PO} = \frac{\rho i}{\pi d} \ln \frac{a+b}{a+b+c}. \tag{5.23}$$

This expression for the potential between points P and O remains true if the current is reduced to i, half of the plane is omitted, and the contacts are placed at the perimeter (figure 5.6). The potential, V_{PO}, for a current flowing out of N is

$$V_{PO} = \frac{\rho i}{\pi d} \ln \frac{b+c}{b}. \tag{5.24}$$

Superposition of these two potentials, shown in figure 5.6, yields the potential developed between points P and O for current, i, entering at M and exiting at N:

$$V_{PO} = \frac{\rho i}{\pi d} \ln[\frac{a+b}{a+b+c} + \frac{b+c}{b}]. \tag{5.25}$$

This expression yields the four point resistance $R_{MN,PO}$, where current is sent into M, taken out of N, and the voltage, V_{PO}, is measured between points P and O:

$$R_{MN,PO} = \frac{\rho}{\pi d} \ln \frac{(a+b)(b+c)}{b(a+b+c)} \Rightarrow \frac{b(a+b+c)}{(a+b)(b+c)} = \exp\left(\frac{-\pi d}{\rho} R_{MN,PO}\right). \tag{5.26}$$

Similar calculations show that for $R_{NO,PM}$,

$$\frac{ac}{(a+b)(b+c)} = \exp\left(\frac{-\pi d}{\rho} R_{NO,PM}\right). \tag{5.27}$$

Addition of equations 5.27 and 5.28 yields the van der Pauw formula:

$$1 = \exp\left(\frac{-\pi d}{\rho} R_{MN,PO}\right) + \exp\left(\frac{-\pi d}{\rho} R_{NO,PM}\right). \tag{5.28}$$

The VDP formula can also be written in terms of the sheet resistance, R_s:

$$1 = \exp\left(\frac{-\pi R_{MN,PO}}{R_s}\right) + \exp\left(\frac{-\pi R_{NO,PM}}{R_s}\right). \tag{5.29}$$

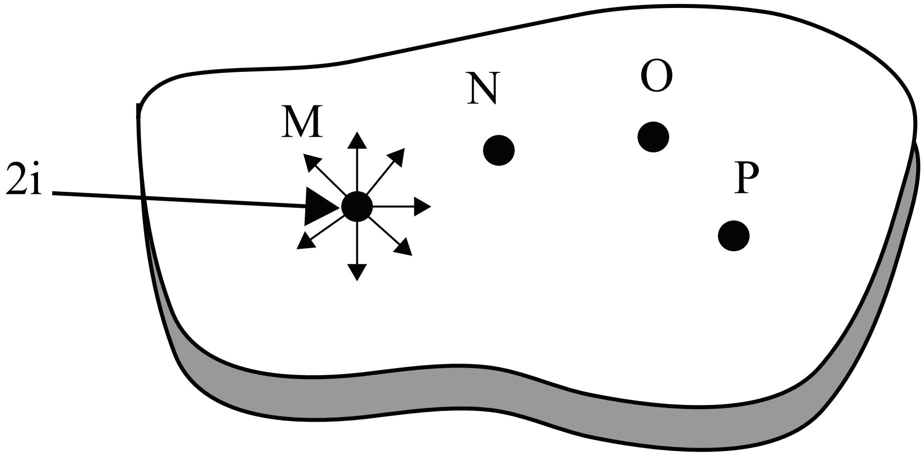

Figure 5.4: The van der Pauw technique places contacts at the perimeter of the sample, and works for arbitrary sample geometries.

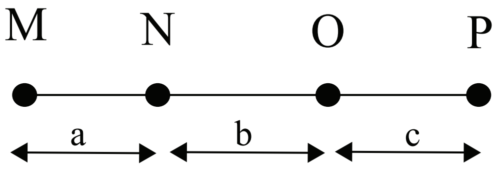

Figure 5.5: Separation distances used for the van der Pauw formula derivation

To use the van der Pauw method to measure sheet resistance accurately, many different permutations (such as $R_{MN,PO}$) need to be measured. For a

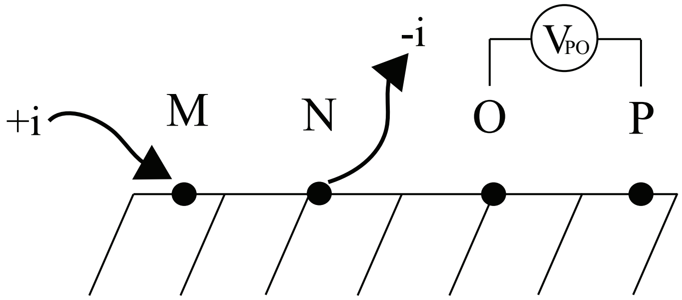

Figure 5.6: Once the infinite surface is reduced in half, the current is reduced by half, and the contacts are placed on the perimeter, the potential between points P and O remains the same as in equation 5.23.

square sample, the standard probe configuration is shown in figure 5.7, where the contacts are placed at the corners of the samples and labeled 1-4 [53].

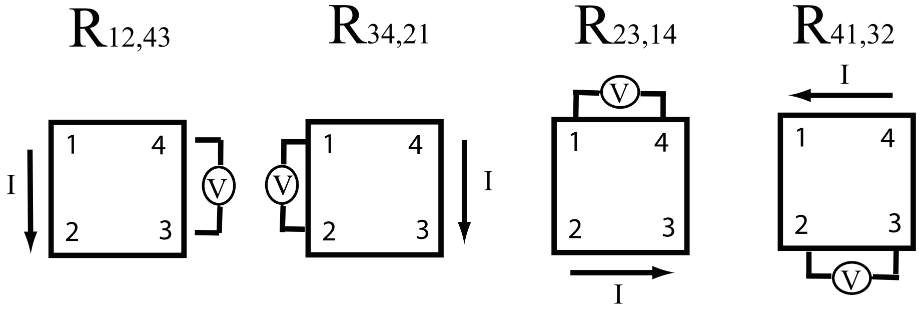

Figure 5.7: The four main permutations that are used for the standard probe placement on a square sample for the VDP configuration.

In one of the examples shown in figure 5.7, the current is sent from contact 1 and withdrawn from contact 2 (referred to as I_{12}), and the voltage is measured between contacts 3 and 4 (referred to as V_{43}), which results in the resistance $R_{12,43}$. At minimum, four measurements need to be taken: two along the vertical edges of the substrate ($R_{12,43}$ $R_{34,21}$) and two along the horizontal edges ($R_{23,14}$ $R_{41,32}$). For improved accuracy four additional measurements are taken with the current reversed from the four previous configurations, i.e., $R_{12,43}$ reversed becomes $R_{21,34}$ (note: current reversal should yield the same value as the normal direction, and more than a 5% difference between the normal and reversed currents indicates a problem that needs to be resolved) [53]. The four vertical measurements are averaged to yield R_V, and likewise, the four horizontal measurements are averaged to yield R_H (not to be confused with the Hall resistance or Hall coefficient). The VDP equation is then solved numerically for the sheet resistance using R_V and R_H:

$$R_H = \frac{R_{23,14} + R_{41,32} + R_{32,41} + R_{14,23}}{4}, \tag{5.30}$$

$$R_V = \frac{R_{12,43} + R_{34,21} + R_{21,34} + R_{43,12}}{4}, \tag{5.31}$$

$$1 = \exp\left(\frac{-\pi R_H}{R_s}\right) + \exp\left(\frac{-\pi R_V}{R_s}\right). \tag{5.32}$$

5.4 van der Pauw method for measuring V_H

One of the advantages of the van der Pauw configuration is that the same probe placement used to measure sheet resistance can be used to measure the Hall effect. The only difference between the two measurements is that in the Hall effect current is sent diagonally across the sample, and the transverse voltage is measured across the other diagonal. There are four configurations for the Hall effect that need to be measured for both positive and negative magnetic field (figure 5.8).

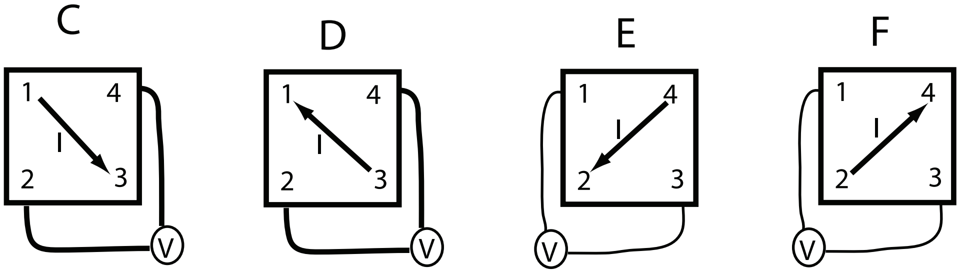

Figure 5.8: The four configurations used to measure the Hall effect using the van der Pauw method. These configurations are commonly labeled C, D, E and F.

The standard labeling for the Hall effect using the van der Pauw configuration is as follows:

$$R_{13,24} \rightarrow V_{24P} \text{ and } V_{24N}, \tag{5.33}$$

where the P and N refer to positive and negative magnetic fields, respectively. Similarly, $R_{31,42} \rightarrow V_{42P,N}, R_{42,13} \rightarrow V_{13P,N}$, and $R_{24,31} \rightarrow V_{31P,N}$. The four permutations lead to four voltages, $V_C = V_{24P} - V_{24N}, V_D = V_{42P} - V_{42N}, V_E = V_{13P} - V_{13N},\ and\ V_F = V_{31P} - V_{31N}$; therefore, the Hall voltage is

$$V_H = (V_C + V_D + V_E + V_F)/8. \tag{5.34}$$

If the Hall voltage, V_H, is greater than zero, the material is p-type and if it is less than zero, the material is n-type. Once the Hall voltage and sheet resistance are known, the carrier concentration and mobility can be calculated using equations 5.16 and 5.17.

5.5 VDP contact size and placement errors

The VDP method, while the most reproducible method for measuring sheet resistance and Hall voltage, does have some limitations. First, the previous derivation for the van der Pauw formula and the Hall voltage assumes that the contacts are infinitesimal points placed at the extreme perimeter of the sample. Placing the contacts at the very corners and creating infinitesimal point contacts is impossible. There are errors associated with both finite size contacts and contact placements inside the perimeter.

For a square sample of length l_s, with square contacts of length l_c (as shown in figure 5.9), the error per contact for resistivity is [54]

$$\frac{\Delta\rho}{\rho} = -\frac{1}{16\ln 2}\frac{l_c^2}{l_s^2}. \tag{5.35}$$

For the Hall effect, the error per contact is

$$\frac{\Delta\mu_H}{\mu_H} = \frac{\Delta R_H}{R_H} = \frac{2l_c}{\pi^2 l_s}. \tag{5.36}$$

The contact size errors are negligible in the case of wire bonded contacts, which are approximately 30μm squares, that produce an error of $\Delta\rho/\rho = 4x10^{-7}$. However, if future measurements create contact with the buried interface by different means, then these errors should be considered.

The more relevant situation is when the contacts are not placed at the exact corners of the sample, as shown in figure 5.10. Wire-bonding creates

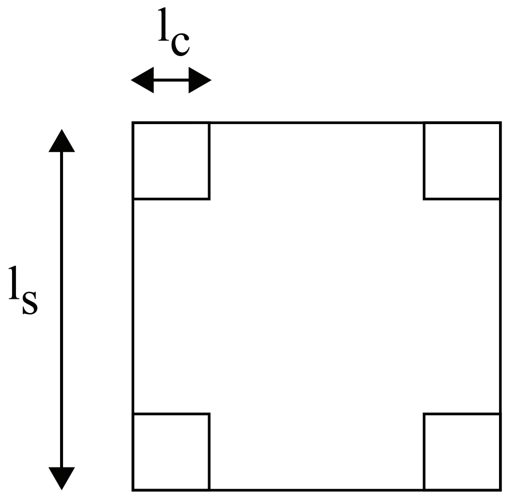

Figure 5.9: Dimensions for equations 5.34 and 5.35

small contacts, but placing the contacts at the edge is close to impossible to achieve. If all of the contacts are a distance d away from the corners for a square sample of length D, then

$$\frac{\Delta\rho}{\rho} = -8.5\left(\frac{d}{D}\right)^4 \tag{5.37}$$

and

$$\frac{\Delta R_H}{R_H} = -4.4\left(\frac{d}{D}\right)^2 \tag{5.38}$$

are the errors associated with resistivity and Hall coefficient, respectively [55, 56].

So what is the advantage to the van der Pauw technique if there are still errors associated with contact placement just as in the linear four probe

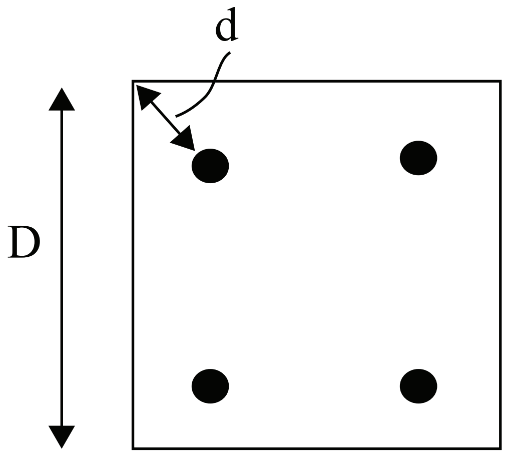

Figure 5.10: Dimensions for equations 5.37 and 5.38

method? First, in practice, using a wire-bonder, it is easier to control the distance that contacts are placed away from the corners than it is to place four equally spaced contacts at a set distance from the edge of a sample. However, and more importantly, for measurements of sheet resistance using the VDP method, there is an altered VDP formula for contacts that are placed very far from the edges of the sample. This method eliminates the need to perform any error adjustments, as long as the contacts are placed at points distant from the sample boundary [51]. The VDP formula for a sample with distant boundaries is

$$1 = \exp\left(\frac{-2\pi R_H}{R_s}\right) + \exp\left(\frac{-2\pi R_V}{R_s}\right). \tag{5.39}$$

This is the most consistent way to measure sheet resistance using the VDP method; however, placing the contacts near the center of the sample does not always work for the Hall effect. If the contacts are placed far away from the edges of a sample, then there are risks of errors in both carrier concentration and carrier type if the sample contains any inhomogeneities [57, 58].

In conclusion, the van der Pauw method offers a reproducible way to measure both sheet resistance and the Hall effect. To measure sheet resistance, the contacts should be placed near the center of the sample, and to measure the Hall effect the contacts should be placed near the corners.

Chapter 6

VDP experiment

In this chapter the experiment and procedures for the van der Pauw measurements of sheet resistance and the Hall effect are described. The various methods that have been used to create contact with the buried interface are discussed, and the experimental setup, including the resistance and Hall effect probes, LabVIEW programs, and the home built switch box are described in detail.

6.1 Wire-bonding: contacting the buried interface

The most difficult part of measuring the transport properties of the 2DEG between polar perovskites and STO is creating contact with the buried interface. There are numerous reported methods that claim to create ohmic contacts with the 2DEG: some that require complicated procedures and some that are very simple [2, 59]. We have attempted to create ohmic contacts by five separate means: silver epoxied platinum wires, bright brushing gold contact pads, thermally evaporated chromium contact pads, pogo-pins, and aluminum wire-bonding.

The first attempt to create contact pads was done using Epotek H21D silver epoxy to connect fine gauge platinum wires to the surface of the film. This procedure worked once out of dozens of attempts and allowed the 2DEG's sheet resistance to be measured. The next method used Alfa Aesar's bright brush gold, which was painted onto the surface of the film and annealed at various temperatures to create contact pads. We had hoped that the gold would diffuse through defects or dislocations in the film; however, this method never worked. We then created chromium contact pads using the Denton-thermal evaporator at the Larry R. Faulkner Nano Science and Technology Building (FNT). A contact shadow mask was designed for this thermal evaporator that held four substrates and created four 0.5 mm diameter contact pads for various configurations (see figure 6.1). This method, although promising from reported success, never worked [59].

During the process of trying to measure the transport properties of the interface, I noticed that measuring resistance by pressing the pointed contacts of a digital multimeter probe into the surface of the film always yielded finite resistance values for LAO/STO. This discovery led me to design a stage that incorporated pogo-pins that would press into the surface of the film, penetrating to the 2DEG[1]. Although this method did make contact with the buried interface, it was difficult to keep all four pogo-pins in direct contact with the film. Thus, stable temperature dependent measurements were never recorded.

Wire-bonding proved to be the most successful way to reproducibly

---

[1] A pogo-pin is a gold coated, spring loaded device with various shaped contact pads that are used to create ohmic contact with a metal pad.

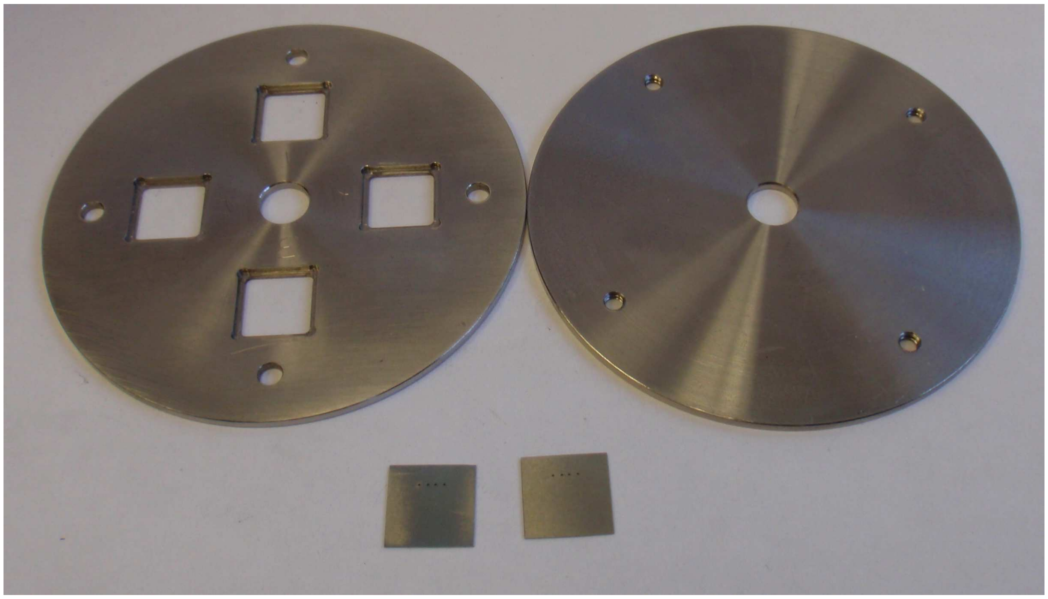

Figure 6.1: This picture shows the shadow mask that was used to thermally evaporate chromium contact pads onto the film's surface.

make contact with the buried 2DEG. We use Dr. Zen Yao's West Bond Inc model 7476D manual aluminum wedge-wedge wire-bonder. This type of wire-bonder operates by pressing a thin gauge wire onto a surface, then ultrasonically heating the wire, which creates the bond[2]. The theory behind the wire-bonder's success is that the ultrasonic energy supplied to the wire-bonder's tip creates micro-cracks in the film and thus allows the melted aluminum to penetrate to the buried interface. The downside to this method is that the operation of the wire-bonder is extremely difficult and requires a lot of practice to perfect the technique. A schematic of the wire-bonder is shown in figure

---

[2] note: Dr. Yao's wire-bonder should only be used after receiving proper training and permission from Dr. Yao or one of his graduate students.

Figure 6.2: The pogo-pin setup used to measure sheet resistance.

6.3, where the fine wire enters from the rear of the setup and is held in place via a pneumatic clamp. The settings that have worked the best are: bond 1 (gold contact pad) power = 400, time = 80 ms, bond 2 (film surface) power = 450, time = 90 ms.

A side-brazed chip carrier (Spectrum Semiconductor Materials, Inc model: SSM P/N CSB04075) that has a cavity size of 0.4 x 0.4 inches is used in the wire-bonding process. This chip carrier (see Appendix B) holds the substrate in the cavity, has 40 gold contact pads specifically intended for wire-bonding, and uses the standard dual-in-line packaging (DIP), which makes the connections to the different probes very easy.

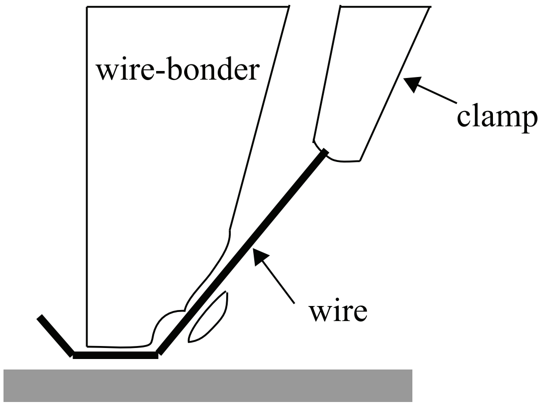

Figure 6.3: This is a side view of the wedge-wedge wire-bonder.

6.2 VDP sheet resistance and Hall effect probes and setup

Sheet resistance and the Hall effect measurements are done using two separate probes. The sheet resistance probe has a stainless steel can that covers the sample but is not secured tightly to the rest of the probe, allowing for cold gas to enter the sample space for temperature dependent measurements. The Hall effect setup is a room temperature experiment and uses a much skinnier probe that can fit between the pole faces of the electromagnet. Future experiments could utilize Quantum Design's MPMS SQUID magnetometer to perform temperature dependent Hall effect measurements using an extremely small leadless chip carrier (Spectrum Semiconductor model: LCC00603) or an existing probe in the lab that has 180° sample rotation capabilities and the 8 T magnet and tail dewar.

The chip carrier connects to a DIP socket located at the base of each probe, that makes electrical connections that are thermally connected to a

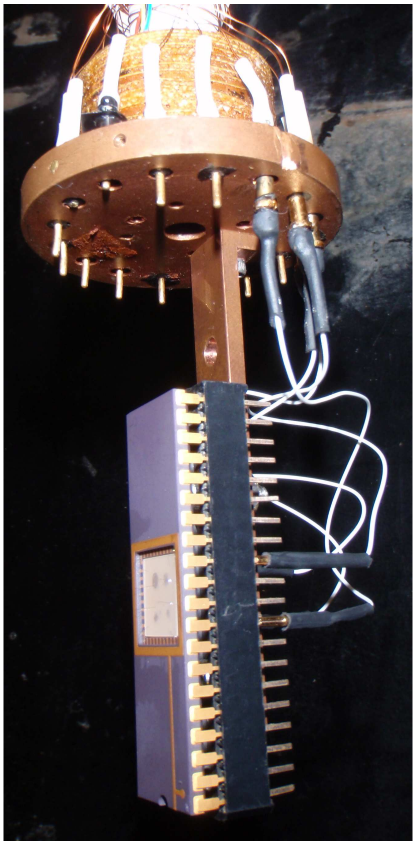

Figure 6.4: This picture shows the resistivity probe, that is connected to the side brazed DIP chip carrier, that has a wire-bonded sample attached to it.

copper block at the base of the probe. Two separate resistive thermometers (RTDs) measure the temperature of the copper block. A Pt100 RTD measures temperatures down to 73K, and then a Ge RTD measures temperatures from 73 to 4K. The wiring of the probe connects to a 24 pin connector at the top of the probe (see Appendix B), which then connects to a home built switch box. This switch box diverts the temperature sensing connections to a Lakeshore temperature controller and sends the various VDP configurations to a resistance bridge. A schematic of the experimental setup, shown in figure 6.5, displays the various elements involved in the sheet resistance experiment.

The various VDP configurations described in section 5.3.2 and 5.4 are controlled by a LabVIEW program that drives a home built switch box that switches the current and voltage inputs to a four wire AC resistance bridge. The LabVIEW program and switch box details are discussed in Appendix B. The output of the switch box connects the correct VDP configuration to a Linear Research LR400 four wire AC resistance bridge that has the capability to measure resistances up to 200 kΩ for various fixed current outputs. The output of the LR400 is a ± 2 V DC full-scale signal that is proportional to the set resistance range on the front panel. For example, if the resistance range on the LR400 is set to 20 kΩ and the output is 1.2 V, then the resistance measured is 12 kΩ. This voltage is measured by a Keithley model 195A digital multimeter that is connected to a computer via a GPIB cable.

To perform either sheet resistance or Hall effect experiments, the LR400 resistance and current settings have to be chosen to match the specific sample under investigation. Typically, the lowest resistance range and lowest current possible are used to increase resolution and reduce heating, respectively. Then the LR400 settings are entered into a LabVIEW program, and the switching between VDP configurations is controlled automatically via the data acquisition card's (DAQ card) digital I/O ports (the user can set the delay time between measurements). The sheet resistance is then solved numerically in the LabVIEW program for the 8 different VDP configurations. Temperature dependent resistance measurements are done on the warm up, rather than the cool down, due to the temperature gradient and different cooling rates between the copper block and the sample. Slow cooling is possible but difficult to achieve and is especially hard when dealing with liquid helium. Therefore, cooling to 4 K is done over the course of at least 1 hour, and warming up is done over the course of 6-12 hours. The slow warm up ensures that the temperature gradient between the copper block and the sample is minimized.

The Hall effect measurement uses the same configuration as in figure 6.5, except a skinnier probe that fits inside the electromagnet is used. The electromagnet's magnetic field is horizontal and points east. This experiment uses a separate LabVIEW program that allows the user to indicate when a measurement should be recorded. This allows the user to rotate the Hall effect probe between positive and negative magnetic fields manually and then record the Hall voltage. Careful alignment of the sample with respect to the magnet is crucial, as is making sure that the height of the sample is the same as the Gauss meter that measures the electromagnet's magnetic field. Typically, the highest values of current available using the LR400 must be used in order to read a stable Hall voltage.

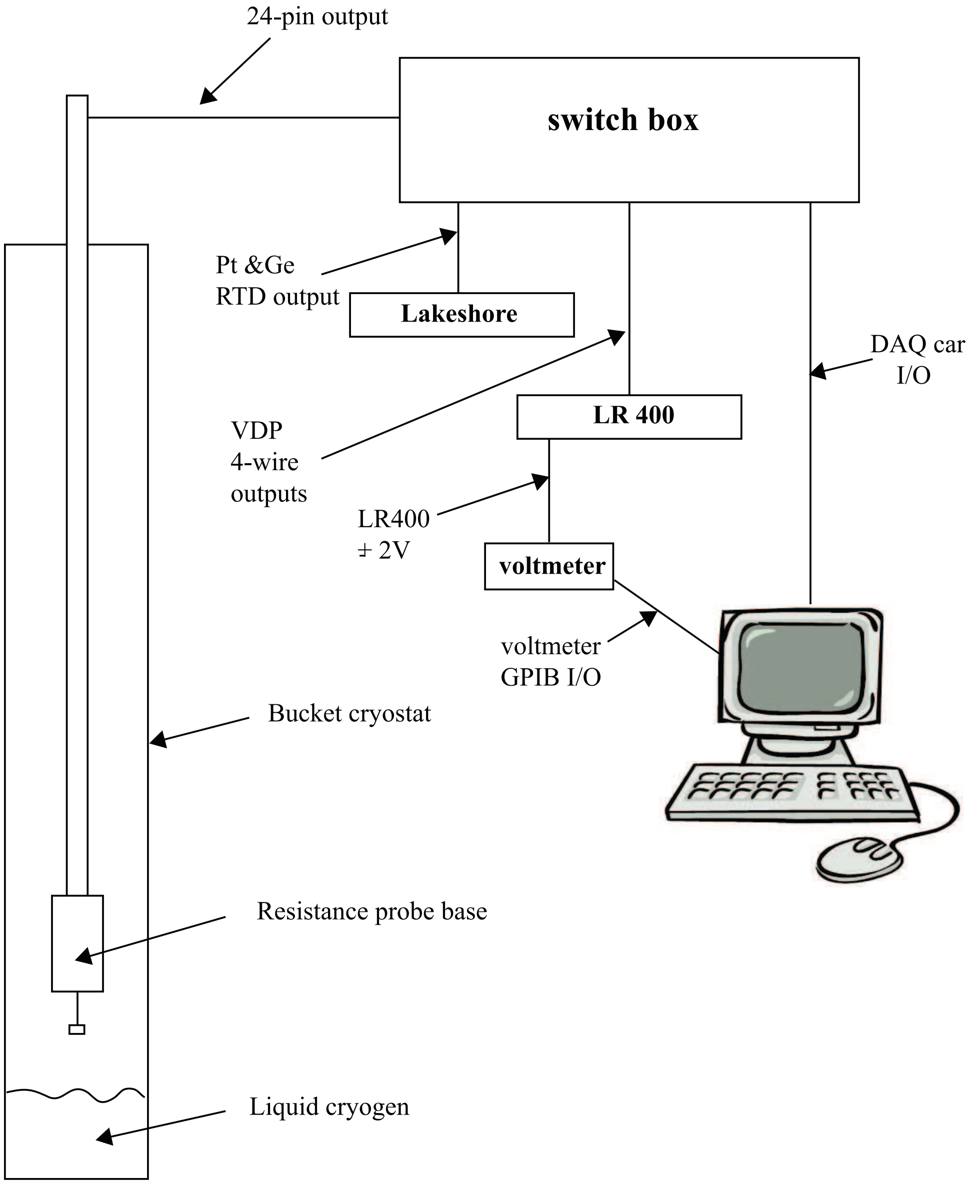

Figure 6.5: Displays the various components involved in the sheet resistance experiment. The Hall effect experiment is identical except that the bucket cryostat is replaced by an electromagnet, and a skinnier probe is used.

6.3 Experimental difficulties

There are many experimental difficulties encountered in this part of the experiment. First, creating good contact with the interfacial 2DEG using the wire-bonder is difficult to achieve. Wire-bonding is an extremely tedious process that requires precision and patience, and, most importantly, the ability to feed the fine gauge wire into the hole (shown in figure 6.3) at the back of the wire-bonder's needle when things go wrong. Furthermore, once the contacts are created, and decent two wire resistances can be measured between wire-bonds, the LR400 often has a difficult time stabilizing for a given VDP configuration. This is likely due to a high contact resistance between the wire-bonded lead and the 2DEG, and repeated wire-bonding can sometimes remedy the problem. Also, during the warm up on a resistance measurement, raising the probe too quickly creates jumps in the sheet resistance data. Thus these measurements are simple in principle but can be difficult in practice.

Chapter 7

Transport property measurements

This chapter presents the experimental data for the transport properties for various $RAlO_3$ perovskites grown on STO. The van der Pauw method was used to measure the temperature dependent sheet resistance and the room temperature Hall effect. Measurements verify that our samples of $LaAlO_3$ / STO and $LaGaO_3$ / STO have metallic interfaces, and the first transport properties of polar perovskite other than LAO and LGO are reported. The effect of magnetism and epitaxial strain on the interface transport properties between $RAlO_3$ and STO are discussed.

7.1 Sheet resistance of $RAlO_3$ perovskites

The literature on the 2DEG between polar perovskites and STO has focussed solely on the LAO/STO heterostructure (with the exception of a few studies on $LaGaO_3$ / STO), and thus little is known about the effect of epitaxial strain or magnetism on the 2DEG transport properties [2, 33, 60, 61, 62]. A recent study explored the effect of strained STO on the 2DEG properties between LAO/STO by first growing STO on various substrates and then growing LAO on the STO film [63]. However, the polar film has not been varied to determine if the strain on the polar film affects the transport properties. This section presents the first temperature dependent sheet resistance measurements of $RAlO_3$ on STO where $R \neq La$.

First we created epitaxial films of both LAO and LGO on STO to reproduce the known behavior of these polar perovskites. The R_s data for LAO is shown in figure 7.1, where it is clear that a metallic interface was formed for this heterostructure. The temperature dependent behavior for a metal decreases with temperature due to reduced phonon scattering, as described in section 5.1, and approaches the material's residual resistance, ρ_0, at low temperatures (recall that ρ_0 is due to impurities and defects). Once the metallic nature of the interface was verified for LAO/STO and LGO/STO, Hall effect experiments were performed to determine the carrier type, carrier concentration, and mobility of the conducting layer. Figure 7.2 shows an example of the Hall voltages recorded for the LAO/STO interface. The room temperature Hall effect data for this interface yield an n-type charge carrier, with $n_S = 1.1$ x 10^{14} cm^{-2} at room temperature, and $\mu = 3.7$ $cm^2V^{-1}s^{-1}$. For LGO/STO the Hall effect yielded $n_S = 4.5$ x 10^{14} cm^{-2}, and $\mu = 0.7$ $cm^2V^{-1}s^{-1}$. These results are consistent with the literature on LAO/STO and LGO/STO, where the carrier densities are commonly in the 10^{14} cm^{-2} range and the mobilities are near 1-5 $cm^2V^{-1}s^{-1}$ at room temperature, for both heterostructures [33, 15]. The slight upturn in the sheet resistance for the LAO/STO sample is most likely due to the relatively high oxygen pressures used during growth [4]. These experiments on LAO/STO and LGO/STO confirmed that our procedures and techniques were capable of reproducing the known results to a high degree of accuracy. Thus, the results obtained for other $RAlO_3$ perovskites on STO can be compared with some confidence.

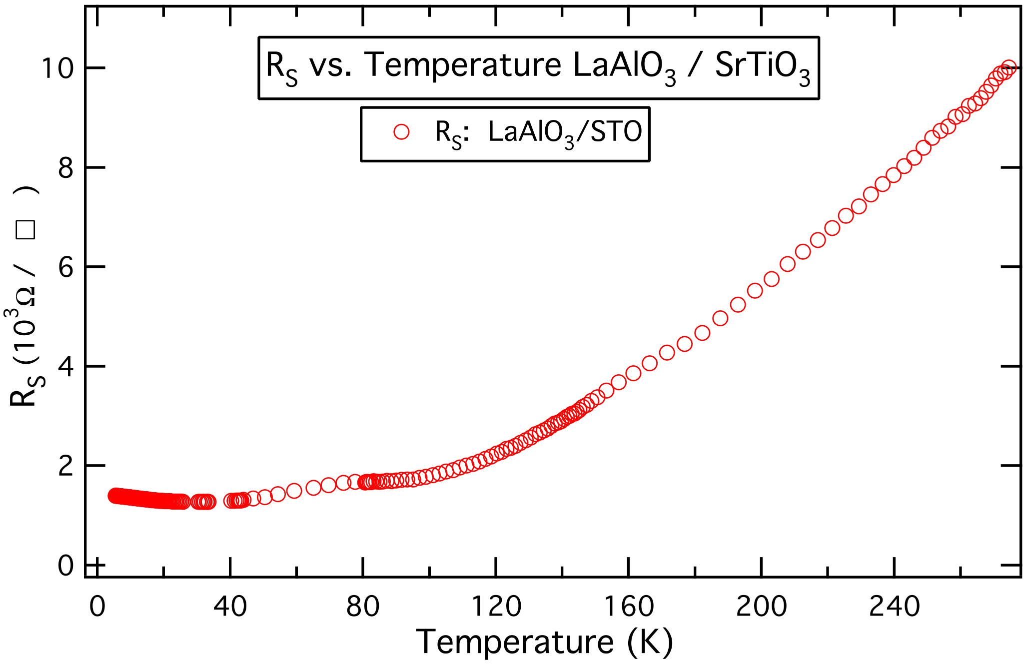

Figure 7.1: Sheet resistance of the LAO/STO interface that shows metallic behavior down to liquid helium temperatures.

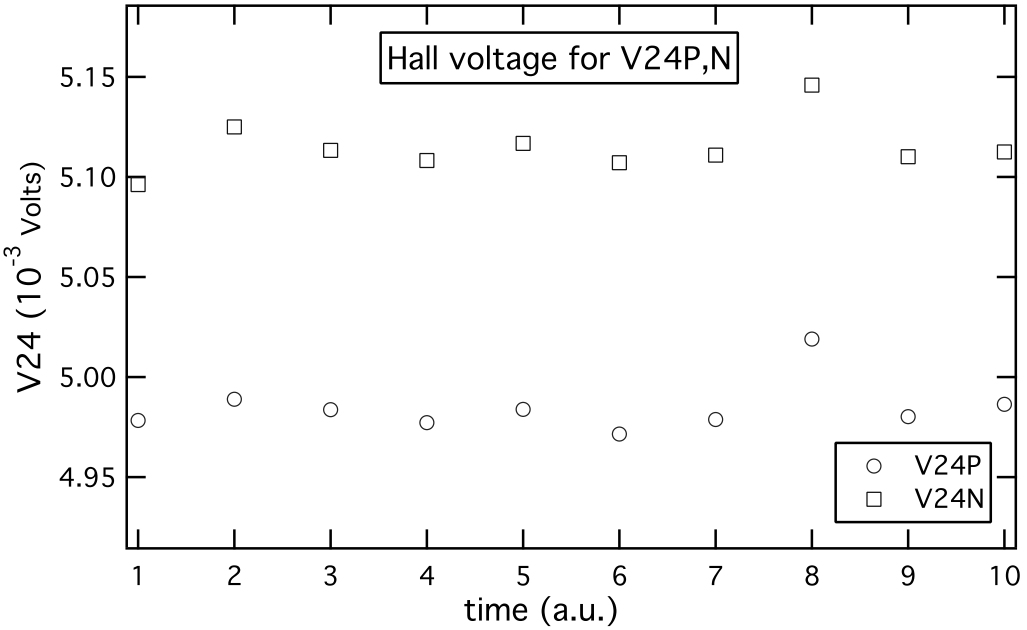

Figure 7.2: One VDP configuration for the Hall voltage measured for the LAO/STO interface. Using this and the other VDP configurations, n_S and μ can be determined.

We next performed measurements on the lanthanide series aluminates ($RAlO_3$, R =Ce, Pr, Nd, Sm, Eu, Gd, Tb) as well as on the two mixed compounds $La_{0.75}Eu_{0.25}AlO_3$ and $La_{0.4}Y_{0.6}AlO_3$. Figure 7.3 plots the XRD data for the (001) film peaks of various $RAlO_3$ films on STO (the large double peaks around 22.77° are the STO substrate peaks, which have saturated the detector). The films of $NdAlO_3$, $SmAlO_3$, and $La_{0.75}Eu_{0.25}AlO_3$ all display broad film peaks that correspond to either a distribution of c-axis lengths or an amorphous crystal structure. The FWHM of the θ-curves for these broad film peaks are in the $0.2-0.3$ ° range, indicating that the film is only somewhat aligned with the substrate, and thus, the quality of epitaxial growth is not excellent. Sharp film peaks with θ-curve FWHM near 0.1 ° exist for $LaAlO_3$, $PrAlO_3$, $EuAlO_3$, and $LaGaO_3$. The XRD data for these four films indicate that they all have very high quality epitaxial growth.

Out of all of the $RAlO_3$ films deposited on STO, the following yield conducting interfaces: $LaAlO_3$, $PrAlO_3$, $NdAlO_3$, and $GdAlO_3$. The rest of the films, including the mixed LaY and LaEu films, were found to be insulating. The temperature dependent sheet resistance results for the various films are shown in the following figures.

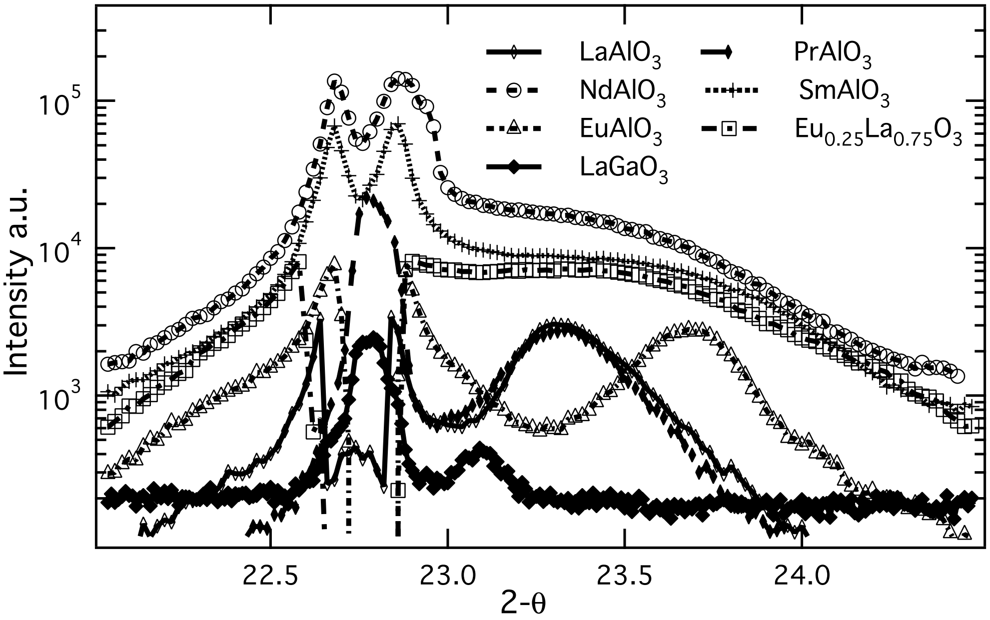

Figure 7.3: XRD data for the RAO_3 perovskites grown on STO. Broad film peaks correspond to a distribution of c-axis lengths, while the sharp film peaks correspond to high quality epitaxial growth.

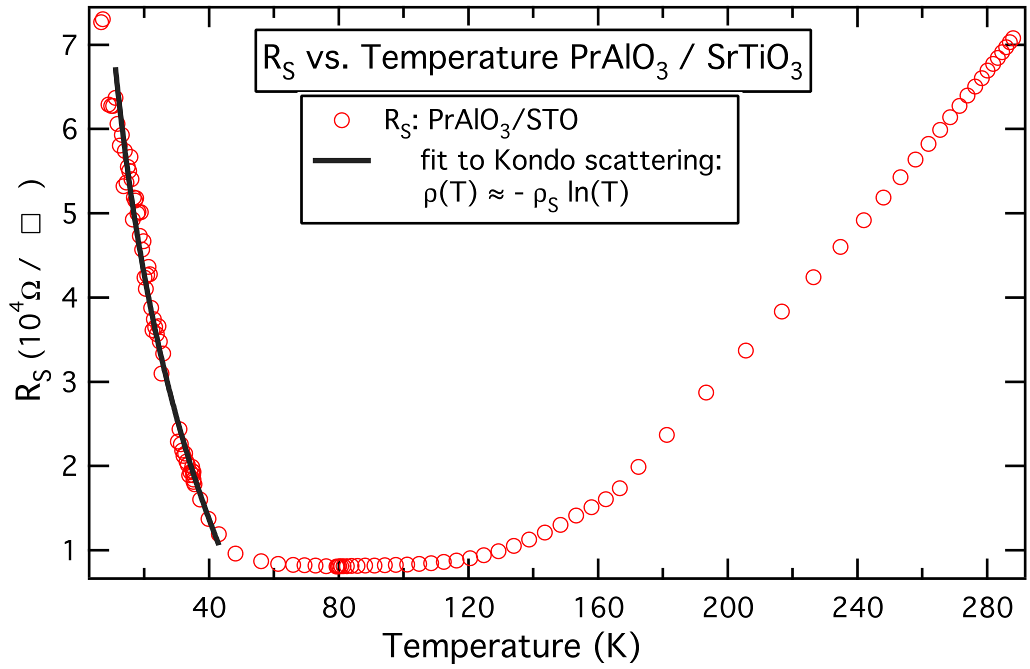

Figure 7.4: Sheet resistance of $PrAlO_3$/STO, which shows metallic behavior down to a transition to increased scattering at 50 K

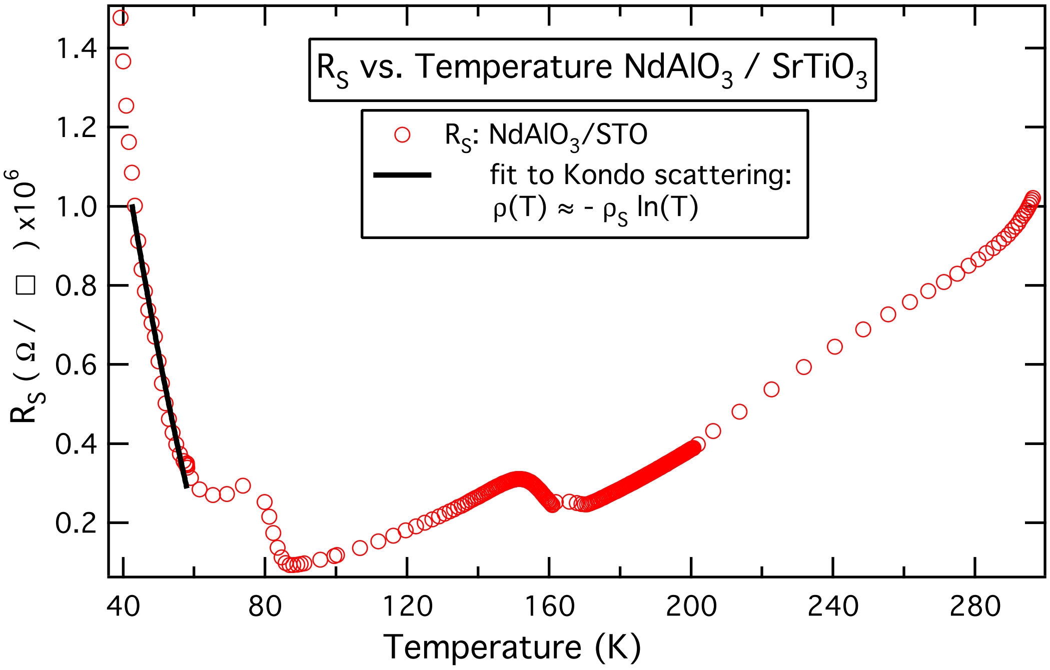

Figure 7.5: Sheet resistance of $NdAlO_3$/STO , which shows a similar transition to higher scattering, as well as two other transitions that could be due to a structural changes.

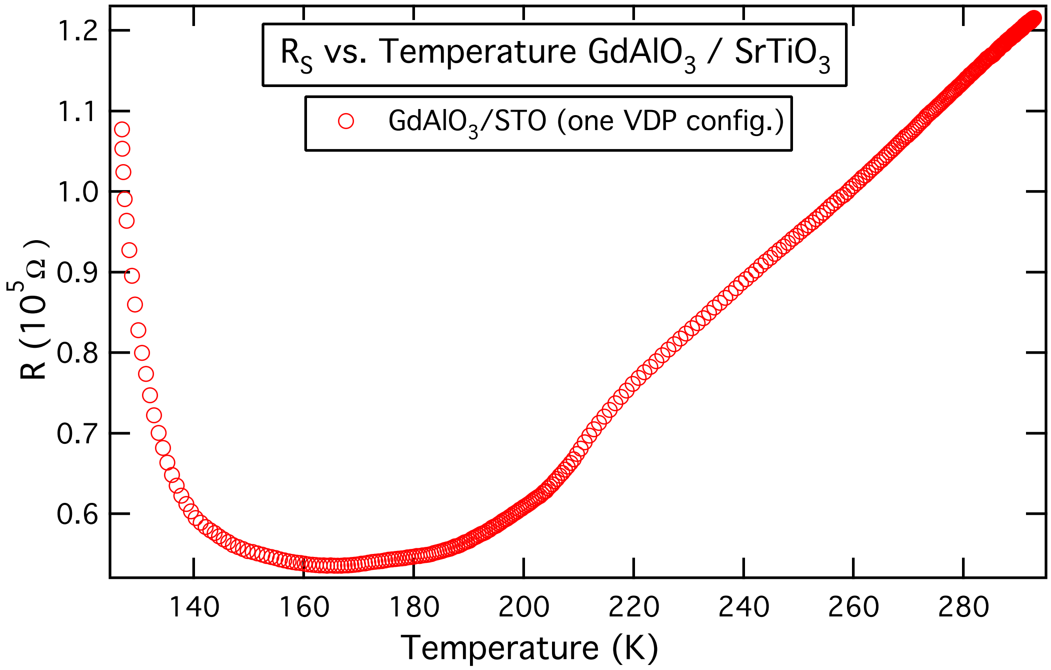

Figure 7.6: Resistance of $GdAlO_3$/STO for only one VDP configuration.

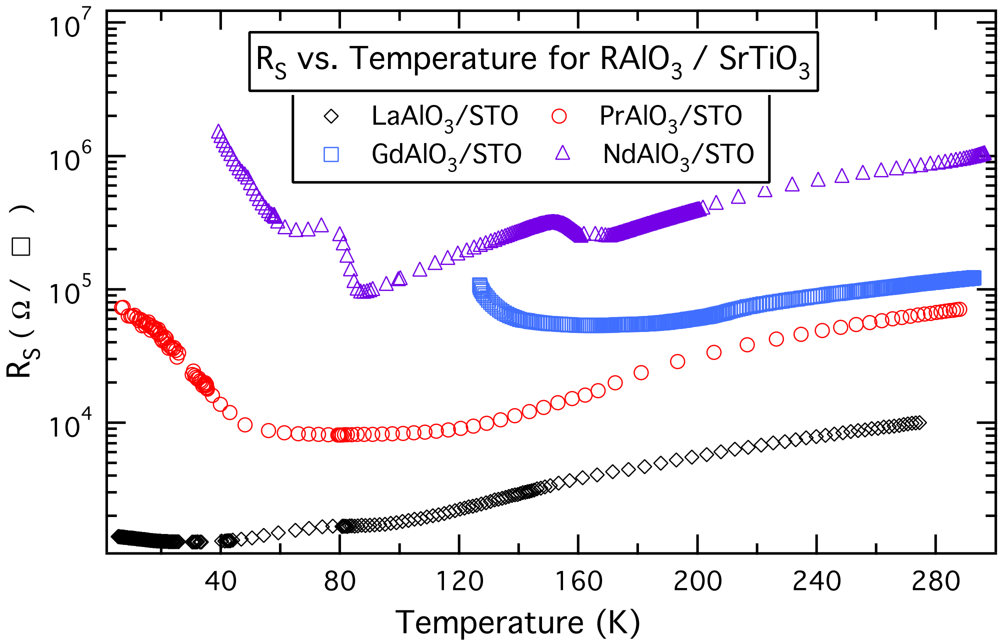

Figure 7.7: A combined plot of the sheet resistances for all $RAlO_3$/STO.

The data suggest that these four $RAlO_3$ heterostructures have metallic interfaces, due to the reduced R_S with decreasing temperature; however, there is an interesting transition for each $RAlO_3$ other than R=La. There is a transition to increased scattering that occurs in each heterostructure that contains a rare-earth ion with f-electrons (magnetic $RAlO_3$) .

The $PrAlO_3$ / STO heterostructure, shown in figure 7.4, displays metallic behavior down to 50 K where it undergoes a possible metal-insulator (M-I) transition. This transition could possibly be due to increased scattering from the presence of magnetic ions, explained by the Kondo effect. In 1933 de Hass discovered an anomalous resistance and the presence of a resistance minimum at low temperatures in metallic samples [64]. This phenomena was later described by Kondo to be a result of the scattering of conduction electrons from magnetic impurities [65]. The relationship that governs the effect of these magnetic impurities, known as the Kondo effect, on the resistivity of a metal is

$$\rho(T) = \rho_0 - \rho_S \ln(T), \tag{7.1}$$

where ρ_0 is the residual resistance, and ρ_S is the contribution of spin-scattering due to the magnetic impurity. In figure 7.4 the black curve is a fit to equation 7.1, indicating Kondo-like scattering in the low temperature region of the sheet resistance. Also, the sheet resistance is an order of magnitude higher than that of $LaAlO_3$, which could be due to increased tensile strain at the interface. Room temperature Hall effect measurements were performed on the $PrAlO_3$ heterostructure, yielding $n_S = 4.5 \text{ x } 10^{13}$ cm^{-2} and $\mu = 1.7$ cm^{2}V^{-1}s^{-1}. Thus, the carrier concentration is lower than that of $LaAlO_3$, the mobility is reduced, R_S is increased, and there is a transition to increased scattering at low temperatures. These effects are likely due to the magnetic nature of the Pr^{3+} ion and the smaller crystal structure of this aluminate that provides an increased tensile strain at the interface.

The $NdAlO_3$ / STO heterostructure, shown in figure 7.5, shows a similar transition to increased scattering at 60 K as well as in two regions (85 K and 165 K) where a kink in R_S is evident. The kinks in R_S are possibly due to structural changes in the $NdAlO_3$ film during cooling; perovskites often experience small transitions from cubic symmetry due to oxygen octahedra distortions. The transition at 60 K is not in great agreement with the Kondo scattering fit (black curve in figure 7.5); however, the fit is sufficient to claim that Kondo scattering is present in this heterostructure. Similar to the case of $PrAlO_3$, the sheet resistance of the $NdAlO_3$ heterostructure is higher than that of $LaAlO_3$ but by two orders of magnitude. Hall effect measurements were unsuccessful on this sample due to the large sample resistance.

The $GdAlO_3$ / STO heterostructure shows room temperature conductivity; however, upon cooling, the sample becomes insulating quite quickly. The data shown in figure 7.6 displays only one of the eight VDP configurations and is therefore not a measure of sheet resistance but displays the general behavior of this film. Little can be concluded from this sample because the

XRD data was unsuccessful in finding a film peak, and resistivity measurements were unsuccessful in determining temperature dependent R_S. However, it is apparent that this structure undergoes a similar transition to the $PrAlO_3$ and $NdAlO_3$ heterostructures at 140 K.

We also created a mixed $RAlO_3$ / STO heterostructure with R = $La_{0.75}Eu_{0.25}$ in order to study the effect of a diluted magnetic film on the transport properties of the interface. We were successful in growing decent films of this compound, but all of the films were insulating. A detailed study of $La_{1-x}Eu_xAlO_3$, for small x, needs to be performed in order to determine the effect of this dilute magnetic material on the transport properties between $RAlO_3$ / STO heterostructures.

In conclusion, films of $RAlO_3$ on STO show a transition to increased scattering that occurs for R^{3+} ions that have f-electrons, where the transition temperature increases with decreasing ion size. Also, the sheet resistance of the interface increases with decreasing R^{3+} ion size, and it is possible that the carrier concentrations decrease with decreasing R^{3+} ion size; however, Hall effect data for the $NdAlO_3$ sample is needed to confirm the latter.

7.2 Effect of magnetism on 2DEG between $RAlO_3$ and $SrTiO_3$

The effect of magnetism on the transport properties between polar perovskites and STO has not been studied previous to this work nor has any $RAlO_3$ / STO interface other than R = La been shown to have a conducting interface. This work is the first systematic study of the effect of R^{3+} magnetism on the 2DEG between polar perovskites and STO, and therefore, it offers a perspective yet to be seen on these fascinating heterostuctures. Furthermore, the implications of the Kondo effect due to a strictly 2DEG have not been studied[1], and there is much controversy over how the Kondo effect affects diluted alloys for thin films.

Kondo scattering is a simple framework in which to describe the effect of magnetism on the conducting properties of the 2DEG between magnetic $RAlO_3$ films and STO. The Kondo effect, as previously mentioned, describes the scattering mechanism of conduction electrons with magnetic scattering centers. The resistivity of a metal has contributions from both the scattering of conduction electrons with the vibrating nuclei (lattice phonons) as well as a contribution from defects or impurities (residual resistance at low temperatures). The lattice contributions decrease with decreasing temperature, and in most metals the low temperature behavior is governed by defects and impurities, which contribute a temperature-independent contribution. However, in some metals a resistance minimum can be found that indicates that there is another scattering mechanism responsible for the observed upturn in resistivity at low temperatures. In 1964 Kondo showed that this resistance minimum was due to the presence of magnetic impurities coupling to conduction electrons and described the resistance relationship with a logarithmic dependence

---

[1] The Kondo effect has been examined in the 2D limit for quantum-dots and 2D molecular assemblies but not for a pure 2DEG [66].

on temperature (equation 7.1). The physical interpretation of the Kondo effect is that the magnetic impurity atom induces the formation of a screening cloud of conduction electrons, which as T→0 completely screens the magnetic spin. The quantitative explanation involves a spin-flip process where both the spin of the magnetic impurity and the scattered electron are flipped. Studies of thin films with magnetic impurities have shown that the Kondo effect is reduced as the thickness of the film decreases [67, 68, 69]. This is explained by surface anisotropy that reduces the motion of the Kondo spins, causing a reduction in the Kondo effect [70]. However, not all experimental results are consistent with this thickness dependence of the Kondo effect, and there have been many studies that are aimed at determining the Kondo interaction for thin samples [71, 72]. Therefore, the 2DEG between $RAlO_3$ and STO is a novel system that could help clarify the thickness dependence of the Kondo effect.

Figure 7.8 displays the region of the resistivity for $PrAlO_3$ / STO in which Kondo scattering is thought to be present. The black curve shows a fit to equation 7.1, and from this fit the residual resistance and the spin scattering coefficient are determined to be 1.6 x 10^5 Ω and 40116 Ω, respectively. Figure 7.9 displays the Kondo scattering region for the $NdAlO_3$ / STO heterostructure. The fit is not as clean as in the case of $PrAlO_3$ but does indicate that Kondo scattering may be present. The residual resistance and the spin scattering coefficient for $NdAlO_3$ are determined to be 1.1 x 10^7 Ω and 2.6 x10^6 Ω, respectively. The spin scattering coefficient (also referred to as the Kondo slope) is a rough measure of the concentration of magnetic impurities for dilute metals with magnetic impurities below 100 ppm. However, in systems with higher concentrations of magnetic impurities the interaction between impurities must be considered. These impurity interactions are described by the Ruderman-Kittel-Kasuya-Yosida (RKKY) interaction that explains the effects of spin ordering on the resistivity at low temperatures. In the RKKY model if $k_B T \gg g\mu_B H$, where g is the Landé g factor, μ_B is the Bohr magneton, and H is the internal field caused by all other moments, then the impurity interactions can be neglected and the resistivity can be explained by the Kondo effect. When $k_B T \ll g\mu_B H$, then the Zeeman splitting of the impurity states is large and the spin-flip scattering becomes inelastic, quenching the Kondo effect [73]. The Landé g factor is given by the equation

$$g = 1 + \frac{J(J+1) + S(S+1) - L(L+1)}{2J(J+1)}, \tag{7.2}$$

where the total angular momentum J is the sum of the orbital L and spin S angular momenta. The Bohr magneton, μ_B, is defined as $e\hbar/2m_e c$ and is equal to 9.274 x10^{-24} J/T. The Pr^{3+} ion has 2 f-electrons with $S = 1$, $L = 5$, and $J = 4$, yielding $g = 0.80$. The Kondo effect for $PrAlO_3$ appears to be present between 15−50 K, which corresponds to $k_B T$ between 1−4 meV. If the Kondo effect is the dominant scattering mechanism then the above inequality imposes an upper limit on the local field H. In $PrAlO_3$ / STO for temperatures between 15−50 K the upper limit on H is 250−1000 Oe. The Landé g factor value for Nd^{3+} is 0.727, which yields a similar upper limit on the local field. Therefore, it is unlikely that inter-magnetic impurity interactions are responsible for the upturn in resistivity, and the scattering mechanism is most likely due solely to the Kondo effect.

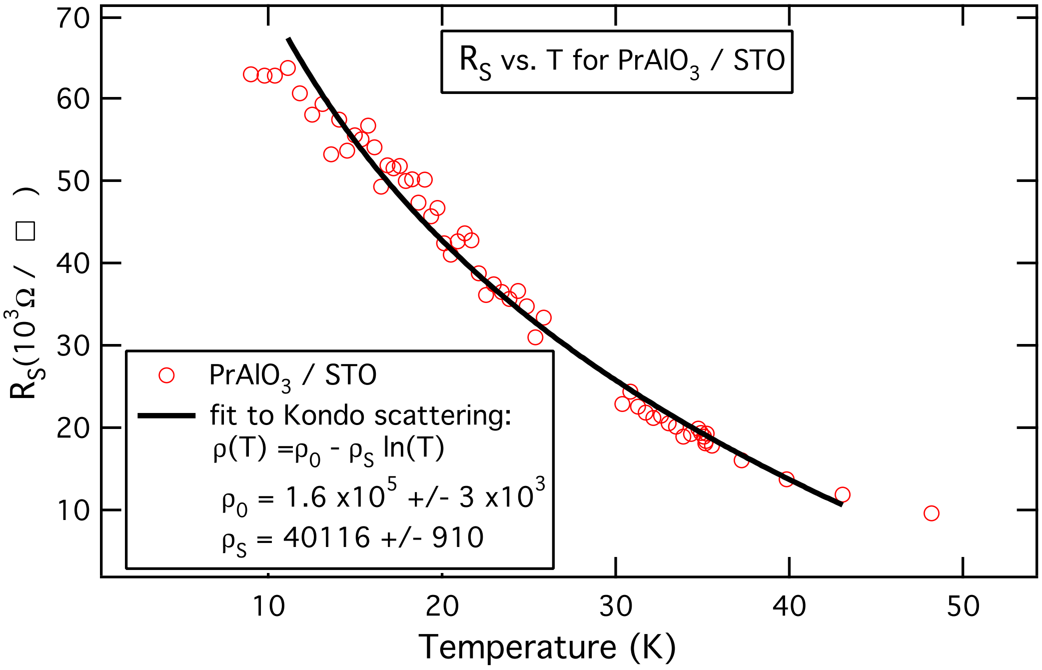

Figure 7.8: This figure displays the region of Kondo scattering in the $PrAlO_3$ / STO heterostructure.

It appears that the existence of magnetic ions in the polar film causes a transition to increased scattering at low temperatures that is described by the Kondo effect. However, the increased sheet resistance and different transition temperatures cannot be explained by Kondo scattering. A study by Torrance of rare-earth nickelates suggests the existence of a size dependent metal-insulator transition. Figure 7.10a displays the temperature dependent

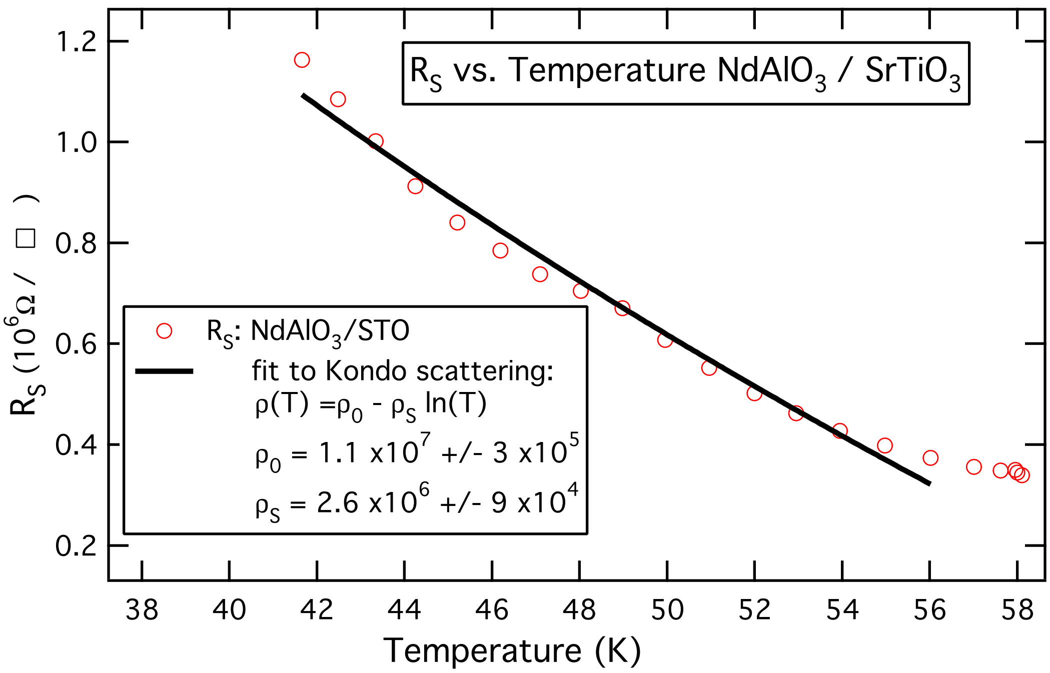

Figure 7.9: This figure displays the region of Kondo scattering in the $NdAlO_3$ / STO heterostructure.

resistance data for a series of $RNiO_3$ [74]. This data indicates that for the magnetic nickelates (R = Pr, Nd, Sm) there is a metal-insulator transition that increases in temperature and an increased resistance for nickelates with decreasing R^{3+} size. Furthermore, this transition is accompanied by a structural change in the nickelate (figure 7.10b). Even though this data is for the bulk properties of these $RNiO_3$, it suggests that the sheet resistance and transition temperatures are size dependent. Thus, the similar effects present in our $RAlO_3$ / STO heterostructures (R = La, Pr, Nd) are likely due to the size of the R^{3+} ion and the epitaxial strain at the interface.

Furthermore, a very recent study on doped STO found that there exists metal-insulator transitions that increase in temperature with decreasing sheet carrier density [75]. These results are shown in figure 7.11 (the carrier concentrations are in units of 10^{13} cm^{-2}). The carrier concentration of our $PrAlO_3$ sample was lower than that of our $LaAlO_3$ sample, and thus this study offers another explanation for the transition based on a decreasing carrier concentration. Future work could study the temperature dependent Hall effect that would reveal if carriers are freezing out, contributing to metal-insulator transition effects.

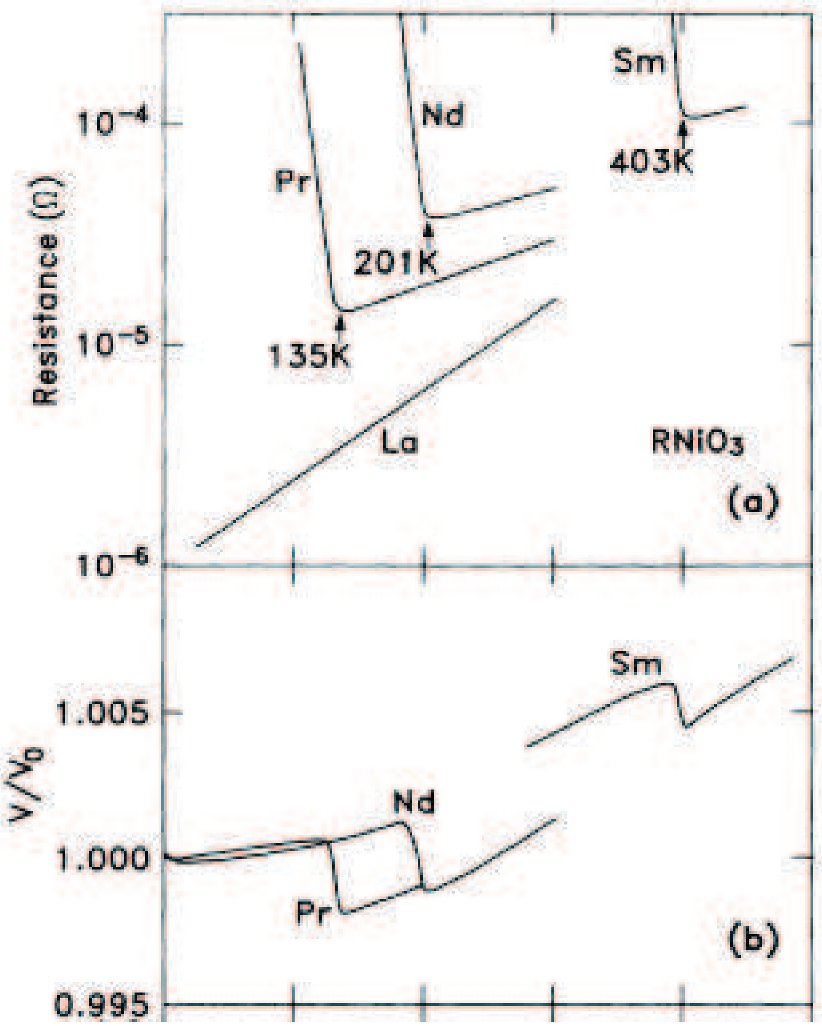

Figure 7.10: A study of the rare-earth nickelates that shows a metal-insulator transition that is accompanied by a structural change in the nickelate perovskite. Figure taken from Ref: [74].

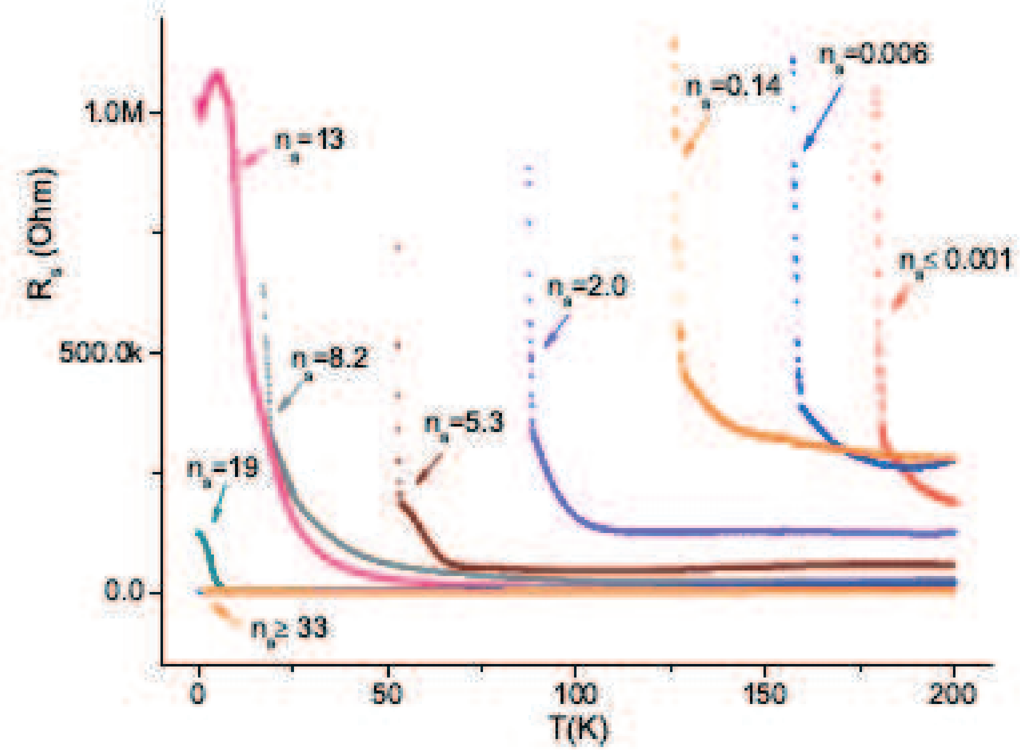

Figure 7.11: Metal insulator transitions in doped STO that show a dependence on the carrier concentration. Figure taken from Ref: [75].

7.3 Insulating $RAlO_3$ /STO heterostructures: epitaxial strain

The formation of epitaxial films for the $RAlO_3$ is a complex process, and it becomes increasingly more difficult with decreasing R^{3+} cation radii. This is partly due to the fact that the compounds become increasingly less thermodynamically stable as the size of the cation decreases [76]. The smallest R-cations of the lanthanide series (Dy, Ho, Er, Tm, Yb, and Lu) require high pressure synthesis in the GPa range in order to create single crystals [77]. An exception to the above is $CeAlO_3$, which is stable in reducing atmospheres but decomposes upon heating in oxidizing atmospheres into Ce_2O_3 and Al_2O_3 [78]. Thus, the creation of epitaxial films of aluminate perovskites has its difficulties, making a comparison of epitaxial strains at the interface difficult to achieve.

We find that the $RAlO_3$ / STO heterostructures containing R = Ce, Sm, Eu, Tb, $La_{0.4}Y_{0.6}$, and $La_{0.75}Eu_{0.25}$ are insulating. Even in the case of high quality epitaxial growth for $EuAlO_3$ and the existence of film peaks for $La_{0.75}Eu_{0.25}AlO_3$ and $SmAlO_3$, we find insulating interfaces (no film peaks were seen for R = Ce, Tb or $La_{0.4}Y_{0.6}$). Tolerance factors and lattice sizes (300 K and 1000 K) for all $RAlO_3$ studied are shown in table 1[2]. The tolerance factor t is a measure of the stability of a perovskite:

---

[2] The tolerance factors were taken from Ref: [79] and the lattice parameters were taken from Ref: [78, 32, 80, 81, 82, 83, 84]

R =	La	Ce	Pr	Nd	Sm	Eu	Gd	LaEu	LaY
t	0.886	0.878	0.871	0.867	0.860	0.857	0.853	x	x
a (300)	3.795	3.775	3.775	3.765	3.740	3.725	3.715	3.785	m-p
b	3.795	3.765	3.775	3.765	3.740	3.740	3.725	3.785	m-p
c	3.785	3.785	3.795	3.730	3.735	3.730	3.750	3.765	m-p
a(1000)	3.820	3.80	3.785	3.785	3.765	3.755	3.740	x	x
b	3.820	3.80	3.785	3.785	3.755	3.760	3.750	x	x
c	3.820	3.795	3.780	3.765	3.755	3.755	3.760	x	x
C or I	C	I	C	C	I	I	C	I	I

Table 7.1: Tolerance factors t and lattice parameters for $RAlO_3$ perovskites at 300 and 1000 K. x = data not available, m-p = mixed-phase: orthorhombic and rhombohedral, C = conducting interface with STO, I = insulating interface with STO

$$t = \frac{r_A + r_O}{\sqrt{2}(r_B + r_O)}, \tag{7.3}$$

where r_A, r_B and r_O are the ionic radii of cation A, B and oxygen, respectively. For an ideal perovskite the ratio of d_{A-O}, the bond length between A-O, to d_{B-O}, the bond length between B-O, is $\sqrt{2}$:1. Therefore, an ideal perovskite has a tolerance factor, t, equal to 1.00; however, experimentally the tolerance factors for many cubic perovskites are in the range of 0.8-0.9, and most compounds that can form perovskite structures have t in the range of 0.75-1.00 [79, 85]. Thus, the perovskites in table 1 all display tolerance factors that correspond to compounds that should form the perovskite structure.

Understanding the effect of epitaxial strain for these heterostructures is important, because strain effects can alter the electrical properties of materials. For example, it has been shown that strain can increase mobility in semiconductors and increase the transition temperature of ferroelectrics and superconductors [86, 87, 88, 89, 90, 91, 92]. Thus, understanding the role of epitaxial strain at the interface for $RAlO_3$ / STO heterostructures could yield possibilities to engineer unique properties. A recent study concluded that the LAO/STO system is conducting if the STO is under tensile strain but becomes insulating if the STO is under compressive strain (performed by growing STO on various substrates to control STO strain) [63]. This study on strained STO also claims that with compressively strained STO the critical thickness of the LAO film increases and the carrier concentration decreases with increasing strain. Furthermore, another study noticed a thickness dependent metal-insulator transition for $LaVO_3$ / STO heterostructures, which they claim is driven by a reduction in the density of charge carriers at low temperatures; however, the mechanism for the reduction in n_s is not discussed [93].

The comparison of LAO / STO to $PrAlO_3$ / STO indicates that an increase in tensile strain in the film both reduces the carrier concentration and increases the sheet resistance; however, this effect could be simply due to the magnetic behavior of the Pr^{3+} cation. However, the increase in sheet resistance of $NdAlO_3$ over that of $PrAlO_3$ is most likely due to epitaxial strain, due to the similar magnetic nature of Pr^{3+} and Nd^{3+} described in the previous section. Thus, we conclude that epitaxial strain is responsible for the increase in sheet resistance and the increase in the transition temperature to increased scattering for the heterostructure $PrAlO_3$ / STO compared $NdAlO_3$ / STO (see figures 7.12 and 7.13).

In order to isolate the effect of epitaxial strain from the R^{3+} magnetism, we created the heterostructure $La_{0.4}Y_{0.6}AlO_3$ / STO, that mimics the lattice size of $EuAlO_3$. All samples of $La_{0.4}Y_{0.6}AlO_3$ / STO were insulating, and furthermore, no XRD film peaks were detected. As can be seen in table 1, the mixed aluminate $La_xY_{1-x}AlO_3$ has a mixed-phase consisting of orthorhombic and rhombohedral structures for $x = 0.4$ (the mixed-phase occurs for $0.25 \leq x \leq 0.85$). Thus, epitaxial growth of a single crystal phase of this compound may not be possible for a lattice size that mimics $EuAlO_3$. In order to determine the effect of epitaxial strain on the interface between polar perovskites and STO other non-magnetic polar films must be created and compared to similar sized magnetic films. A candidate for such a comparison is between $PrAlO_3$ and $La_{0.85}Y_{0.15}AlO_3$. The substituted compound $La_{0.85}Y_{0.15}AlO_3$ should form a single phase rombohedral perovskite crystal with a size that closely resembles that of $PrAlO_3$. In conclusion, it is likely that epitaxial strain plays a direct role in the transport properties between $RAlO_3$ / STO. However, a systematic study between magnetic and non-magnetic polar films of the same size is needed to make definite claims about the effect of epitaxial strain.

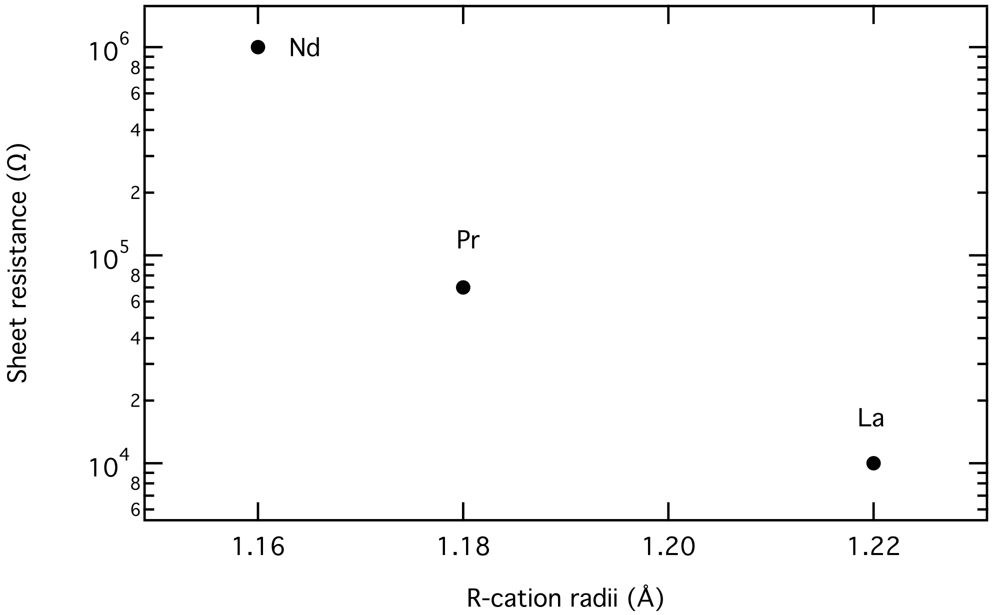

Figure 7.12: The dependence of R-cation radii on sheet resistance. Decreasing R-cation radii corresponds to an increase in sheet resistance in $RAlO_3$ / STO heterostructures.

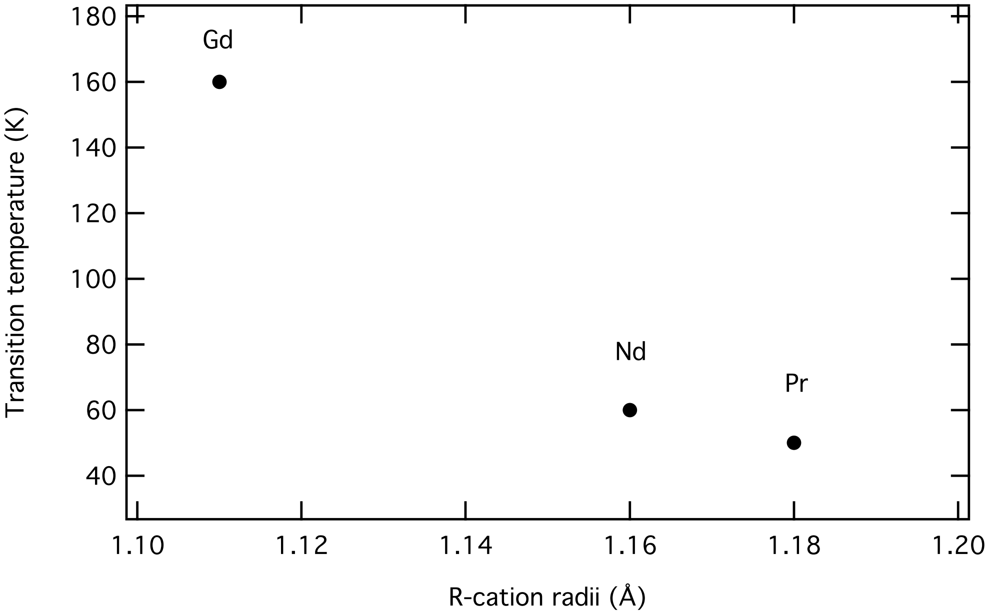

Figure 7.13: The dependence of R-cation radii on the transition temperature to increased scattering. Decreasing R-cation radii corresponds to an increase in the transition temperature in $RAlO_3$ / STO heterostructures.

Chapter 8

Future studies using a nuclear magnetic resonance force microscopy

This chapter will describe an experiment that used a nuclear magnetic resonance force microscope (NMRFM) to study ammonium sulfate $(NH_4)_2SO_4$ as well as a future study that could use NMRFM to image an oxide interface. The experiment performed on $(NH_4)_2SO_4$ was a room temperature proof of viability study for a newly constructed ^{3}He NMRFM probe. An NMR signal was detected for ^{1}H nuclei, and both nutation and spin echo experiments were performed. The future study of an oxide interface focuses on ^{27}Al NMR in $RAlO_3$ thin films grown on $SrTiO_3$.

8.1 Basic Theory of NMRFM

Nuclear magnetic resonance force microscopy (NMRFM) is a technique that detects an NMR signal via a force on an ultrasensitive mechanical oscillator. Conventional nuclear magnetic resonance (NMR) is an inductive detection technique that has a sensitivity of roughly 10^{12} nuclear spins at low temperatures. However, NMRFM could be capable of detecting a single nuclear spin by coupling the nuclear magnetization of a sample to a cantilever that is capable of detecting extremely small forces [94]. Other common imaging techniques, such as atomic force microscopes (AFM) and scanning probe microscopes (SPM), are only capable of imaging the surface [95, 96]; however, NMRFM is a technique that combines both NMR and SPM techniques to yield 3D images.

The basic premise of NMRFM is that a sample's magnetization is coupled to a AFM-like cantilever that produces a force on the cantilever due to the presence of a large magnetic field gradient [97, 98, 99][1]. The setup for the NMRFM experiment is shown in figure 8.1, and a picture of the area outlined in the schematic is shown in figure 8.2. In this configuration, the sample is attached to the cantilever and is placed in a large external field, H_o. The sample's magnetization is manipulated using a radio frequency (RF) magnetic field, H_1, that is perpendicular to H_o. The gradient magnet produces a force on the cantilever,

$$\mathbf{F} = \mathbf{M}(t) \cdot \nabla \mathbf{B}, \tag{8.1}$$

where the sample's magnetization, $\mathbf{M}(t)$, is manipulated by the RF coil so that the force on the cantilever oscillates at the cantilever's resonant frequency. The vibration amplitude of the cantilever is measured by a fiber optic interferometer. Thus, using conventional NMR spin manipulation techniques,

---

[1] The entire theory will not be discussed in this thesis but can be found in the following dissertations [100, 101, 102, 103, 104]

and coupling the nuclear magnetic moments of a sample to an ultrasensitive cantilever, an NMRFM signal can be detected.

The resolution of NMRFM comes from the gradient magnet, which produces a region in space where the spins are on resonance known as the resonance slice,

$$\Delta z = \frac{2\Omega}{\gamma \nabla B}. \tag{8.2}$$

.

Here, the thickness of the resonance slice, Δz, depends on the modulation amplitude of the RF field, Ω, the gyromagnetic ratio, γ, and the strength of the gradient magnet, ∇B. There are two main conditions that must be satisfied in order to detect an NMRFM signal. First, the modulation amplitude of the RF field must obey the adiabatic condition such that

$$(\gamma H_1)^2 \gg \omega \Omega, \tag{8.3}$$

where ω is the cantilever's resonance frequency. As long as the adiabatic condition is satisfied, the nuclear spin magnetization will follow the effective field. Second, the force on the cantilever due to equation 8.1 must be greater than the minimum detectable force of the cantilever (SNR $\geq$ 10 is desirable). The minimum detectable force for a given cantilever is the force needed to overcome the thermal noise level, and is equal to

$$F_{min} = \sqrt{\frac{4k_{osc}k_B T\Delta\nu}{\omega_{osc}Q}}, \tag{8.4}$$

where k_{osc} is the spring constant of the cantilever, ω_{osc} is the cantilever's resonant frequency, and $\Delta\nu$ is the bandwidth of the lock-in detector. Using equation 8.1 and Curie's law, the force on the cantilever is

$$F = N\frac{\gamma^2\hbar^2 I(I+1)H_o}{3k_B T}\nabla B, \tag{8.5}$$

where I is the spin quantum number and N is the number of spins [105].

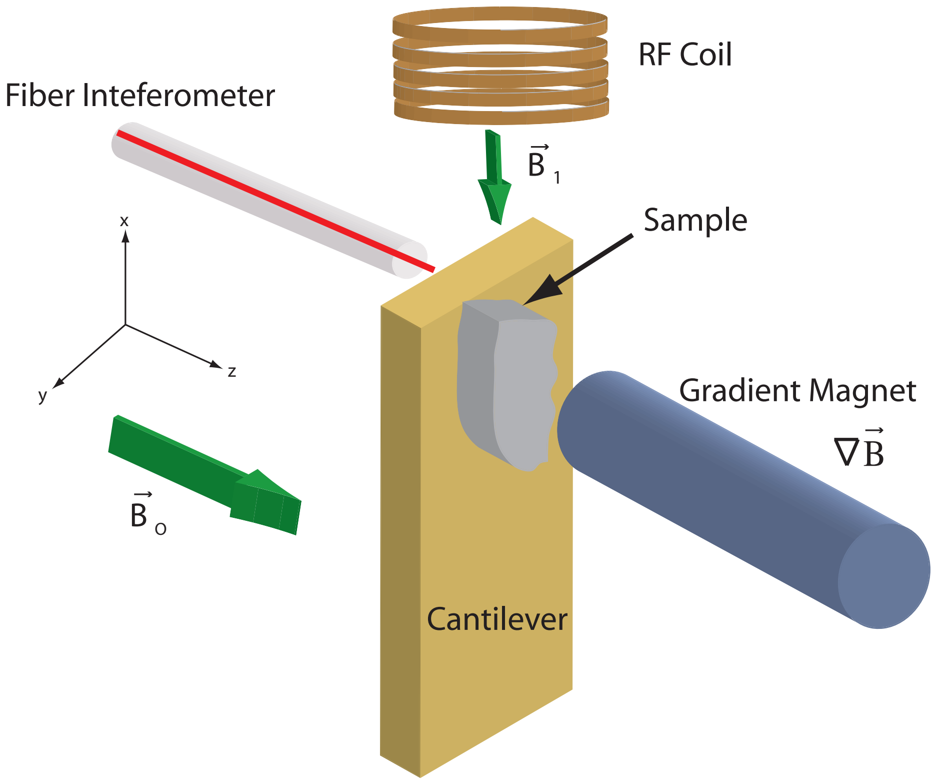

Figure 8.1: This schematic illustrates the various components of the NMRFM experiment.

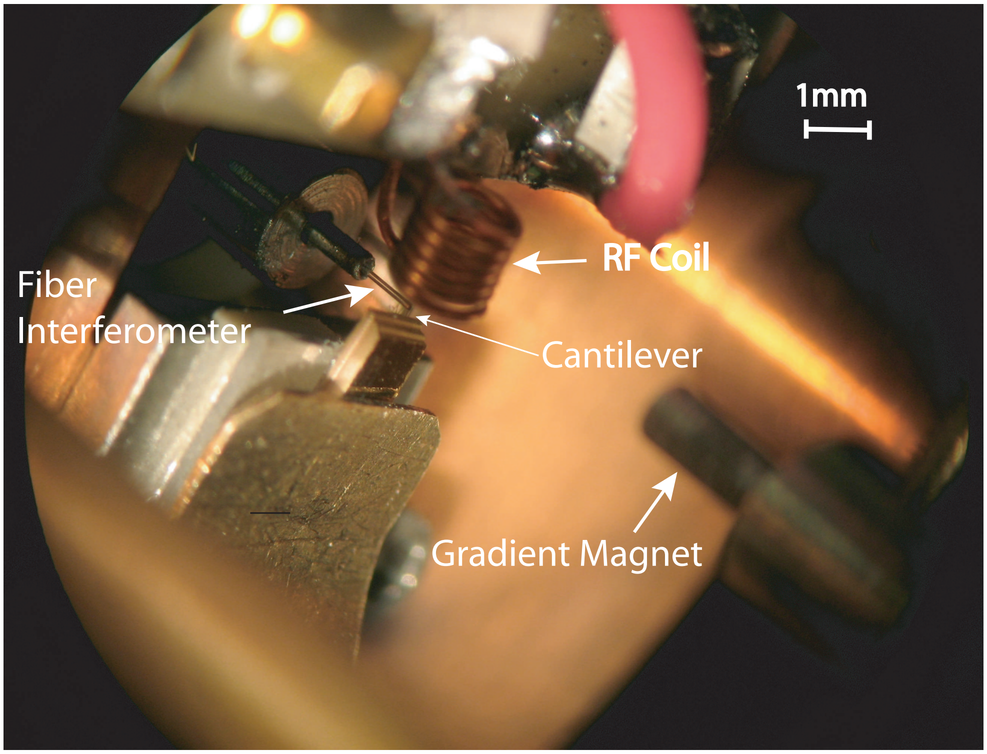

Figure 8.2: A picture taken through an optical microscope of NMRFM probe.

8.2 Experiments on $(NH_4)_2SO_4$ using a ^{3}He probe

One of the main difficulties encountered in NMRFM is the unknown value of the gradient magnetic field. Thus, in order to achieve nuclear resonance and detect an increased amplitude of vibration on the cantilever, the gradient magnet's position must be scanned with respect to the sample. The gradient magnet is attached to a positioning stage that allows adjustment of the gradient magnet to sample distance. If the gradient magnet is at the correct position, then the spins will satisfy the resonant condition

$$\omega = \gamma(B_{gradient} + B_0) \tag{8.6}$$

where ω is the larmor frequency of the nuclei, $B_{gradient}$ is the gradient magnet's field strength at the sample, and B_0 is the field of the external magnet. Once the spins are on resonance they can be manipulated using the RF magnetic field (B_1). Figure 8.3 shows the detection of an NMR signal for two frequencies. The magnet's position is varied, and thus, the resonant field is scanned through the sample. When the resonant field is inside the sample a clear peak in the cantilever's amplitude is evident. Shifting the frequency provides proof that the increased cantilever vibration is truly due to an NMR signal.

Next, a nutation experiment was performed to quantify the strength of the B_1 field. In this experiment, the gradient magnet is fixed so that the spins are on resonance, and the amount of time that the B_1 RF field is on is varied. The amount of time that B_1 is on determines the extent that the

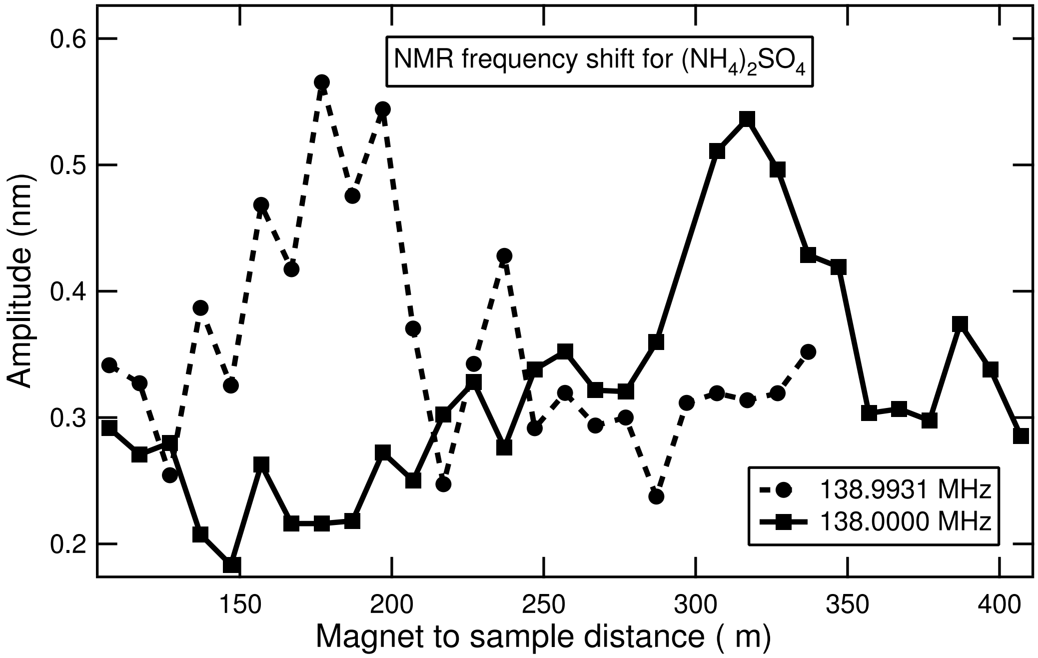

Figure 8.3: NMRFM frequency shift data for $(NH_4)_2SO_4$, that indicates that a true NMR signal was detected.

nuclear spins are tilted and allows for the strength of B_1 to be determined. Figure 8.4 shows the nutation experiment that determined that our B_1 field was 13.6 gauss. Knowing the strength of B_1 is important, because B_1 must be larger than the local field within the sample (3 G).

We then performed a spin-echo experiment which allows determination of T_2^*, that indicates the inhomogeneity of the magnetic field at the sample. The echo decays as $\exp\left(-t/T_2^*\right)$ and yielded $T_2^* = 3\ \mu$s, or $\Delta B = 80$ G.

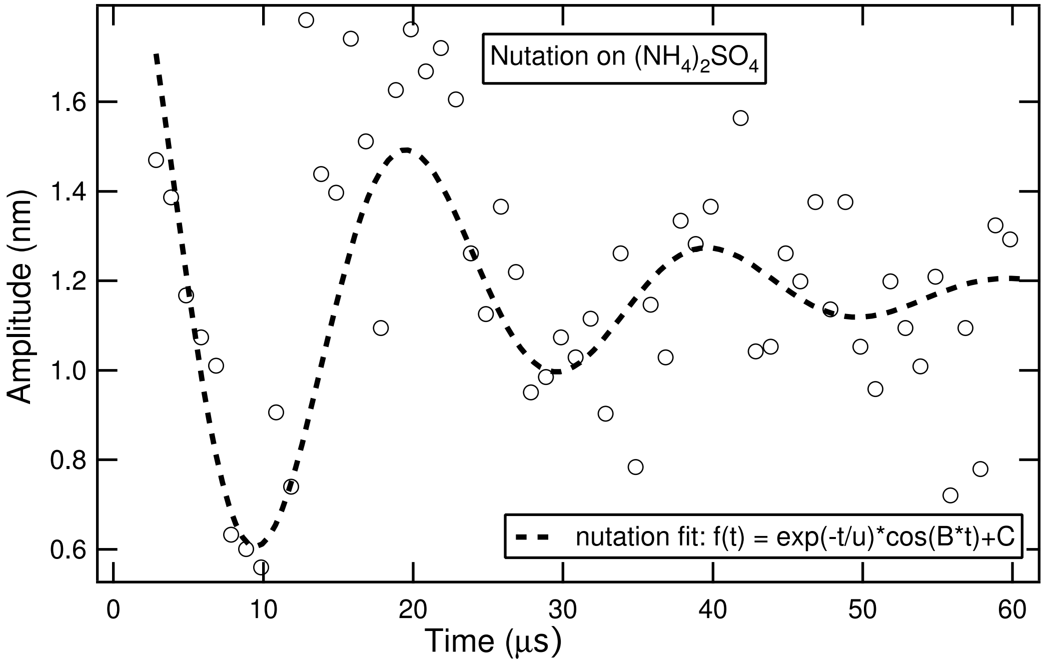

Figure 8.4: A nutation experiment on $(NH_4)_2SO_4$, that quantifies the strength of the magnetic field from the RF coil (H_1 14gauss).

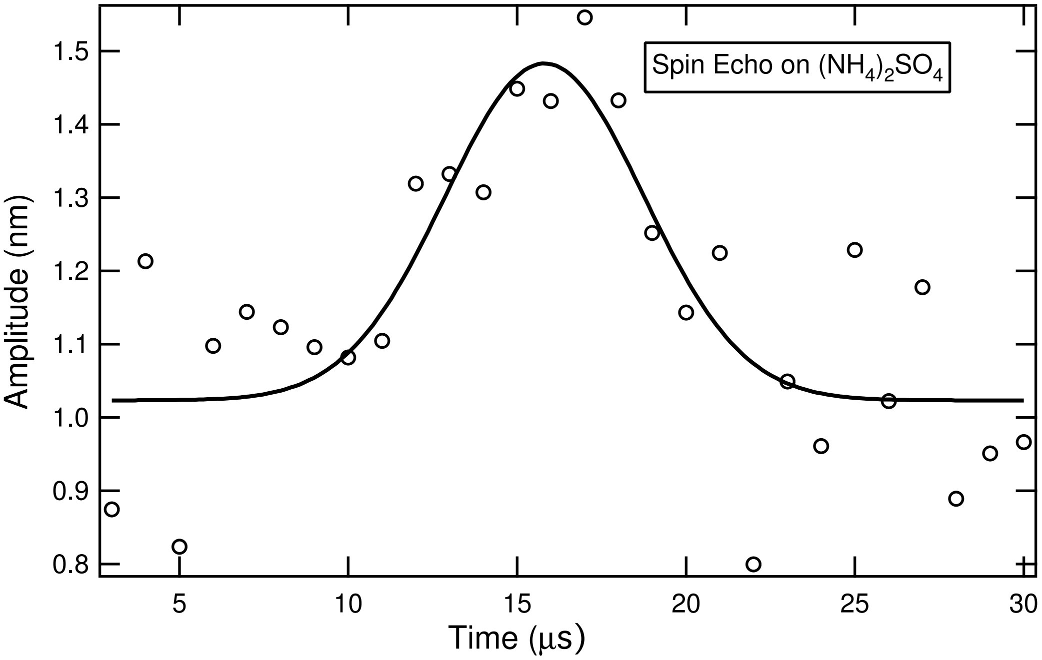

Figure 8.5: A spin-echo experiment on $(NH_4)_2SO_4$.

8.3 Future studies involving oxide interfaces

NMR has been performed on perovskite aluminates such as $PrAlO_3$ and $NdAlO_3$, where the ^{27}Al nuclei was investigated [106, 107]. The ^{27}Al nuclei is 100% abundant, with γ=11.09 MHz/T and $I = 5/2$. The aluminum atoms in the perovskite crystal are surrounded by an oxygen octahedra and interact with the surrounding electric charges via the electric quadrupole interaction. For symmetries lower than the cubic, splitting occurs that produce five separate lines. However, in the case of $PrAlO_3$ a low temperature structural change from orthorhombic to monoclinic increases the crystal symmetry and the splitting between lines vanishes (see figure 8.6). Thus, structural changes in the crystal can be verified using NMR to probe the local environment of aluminum. Also, if an NMR signal could be detected for the ^{27}Al nuclei within the $RAlO_3$ / STO heterostructures, the spin-lattice relaxation times could be determined. The presence of a conducting layer at the interface between the polar perovskite and STO would significantly reduce the spin-lattice relaxation time, T_1, and create a separate measure of the quality of the conducting interface.

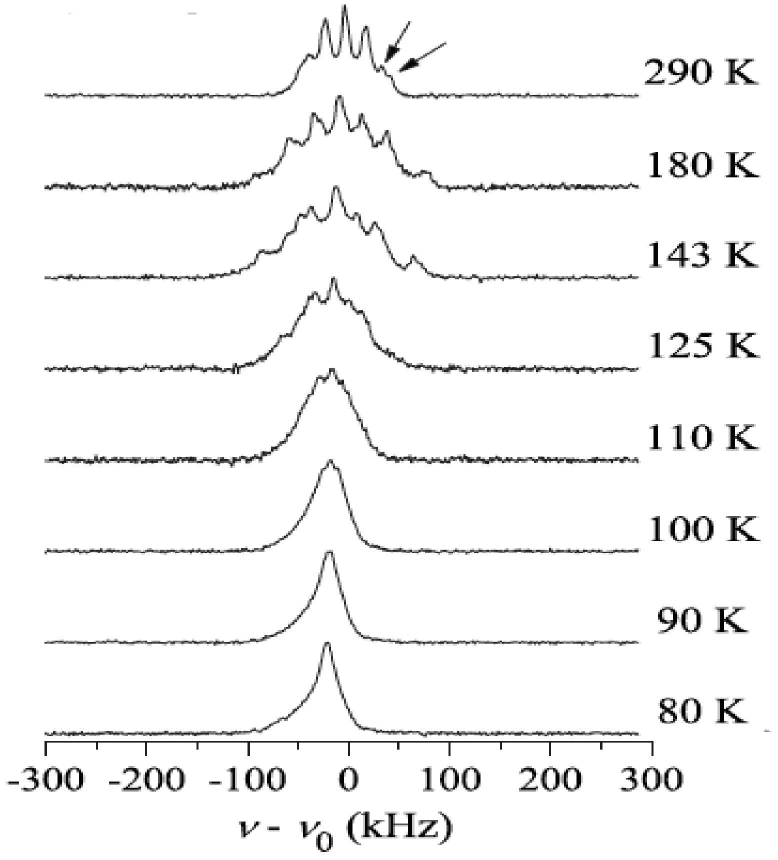

Figure 8.6: This figure shows the splitting of the ^{27}Al nuclear lines in a single crystal sample of PrAlO$_3$. The splitting vanishes once the crystal undergoes a structural transition from orthorhombic to monoclinic. This was taken from Ref. [107].

8.3.1 Feasibility calculations

Here we present calculations to determine the feasibility of using NMRFM to measure the ^{27}Al NMR in PrAlO$_3$ / STO heterostructures. The magnetization from Curie's Law

$$M = N\frac{\gamma^2\hbar^2 I(I+1)H_o}{3k_BT}, \tag{8.7}$$

where $\gamma = 2\pi$ x 11.09 MHz/T and $I = 5/2$. In PrAlO$_3$ there is one aluminum atom per unit cell, and thus the density of ^{27}Al is n = 1.85 x 10^{28} ^{27}Al/m^3. If a gradient magnet of 10 μm x 10 μm is chosen, then ∇B =10^5 T/m and Δz = 30 nm; this is an ideal choice for thin films that are typically 10−20 nm thick. Using Δz for this magnet, $N = n \cdot volume$ = 5.3 x 10^{10} ^{27}Al. The minimum detectable force (equation 8.4) was calculated for $k_{osc} = 10^{-4}$, ω_{ocs} = 2π x 1000 Hz and $Q = 10^3$. Table 8.1 summarizes the temperature dependent results for the feasibility calculations, and this indicates that NMRFM is highly capable of detecting the ^{27}Al nuclei, with SNR values skyrocketing at low temperatures. The adiabatic condition (equation 8.3) is satisfied using a modulation amplitude Ω = 100 kHz and H_1 = 10 G; however, H_1 values up to 33 G have been achieved in our lab, so there is some flexibility on the modulation amplitude.

In conclusion, NMRFM is a promising tool to study the interface between PrAlO$_3$ and STO. The SNR calculations indicate that achieving a detectable signal is quite possible using relatively modest parameters. Moreover,

T (K)	M (J/T)	$F_{expected}$	F_{min}	SNR
77	6.4×10^{-20}	6.4×10^{-15}	2.9×10^{-16}	22
10	5.0×10^{-19}	5.0×10^{-14}	1.0×10^{-16}	473
4	1.2×10^{-18}	1.2×10^{-13}	6.6×10^{-17}	1870
1	5.0×10^{-18}	5.0×10^{-13}	3.3×10^{-17}	15000

Table 8.1: ^{27}Al NMRFM feasibility calculations including: magnetization of aluminum, expected force on cantilever, minimum detectable force, and SNR at various temperatures.

this would be the first NMRFM detection of ^{27}Al to date, and the first relaxation measurements performed on a conducting oxide interface. Such an experiment would also make evident the utility of NMRFM for study of very thin films, which are traditionally not accessible using conventional NMR.

Appendices

Appendix A

Heater Assembly

This appendix provides the SolidWorks designs for the custom heater assembly used in the PLD system. The boron nitride (AX05 1"x1.5") was given to us by Steve Lyle (stephen.s.lyle@saint-gobain.com) at Saint-Gobain Boron Nitride (www.bn.saint-gobain.com, 716-691-2015). The heater is a delicate device and should be assembled (disassembled) with great care!

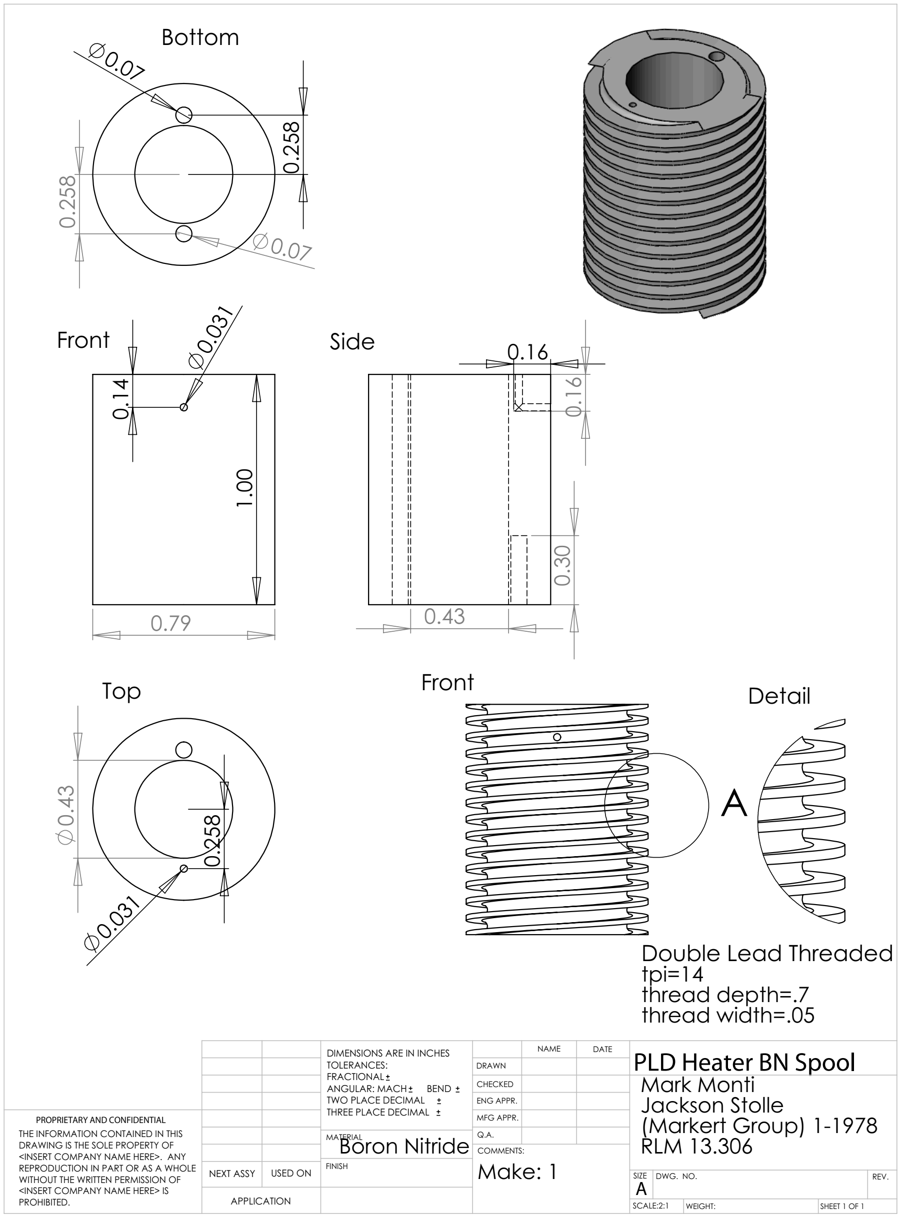

Figure A.1: SolidWorks drawing of the boron nitride double lead threaded heater spool.

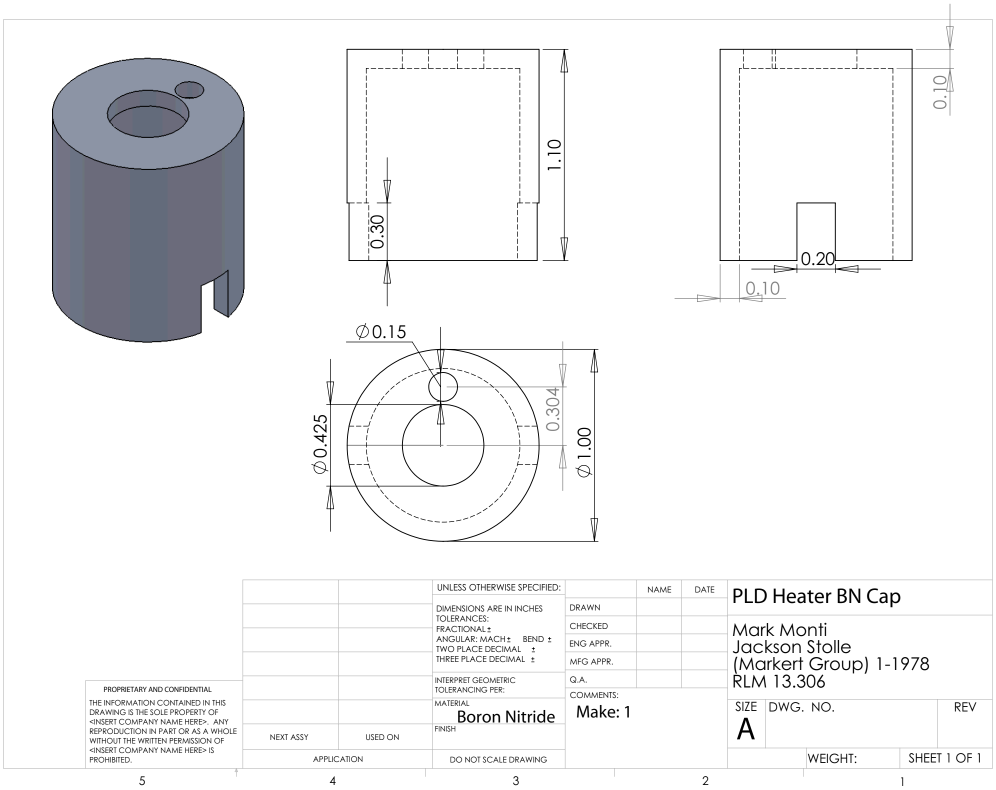

Figure A.2: SolidWorks drawing of the boron nitride heater cap.

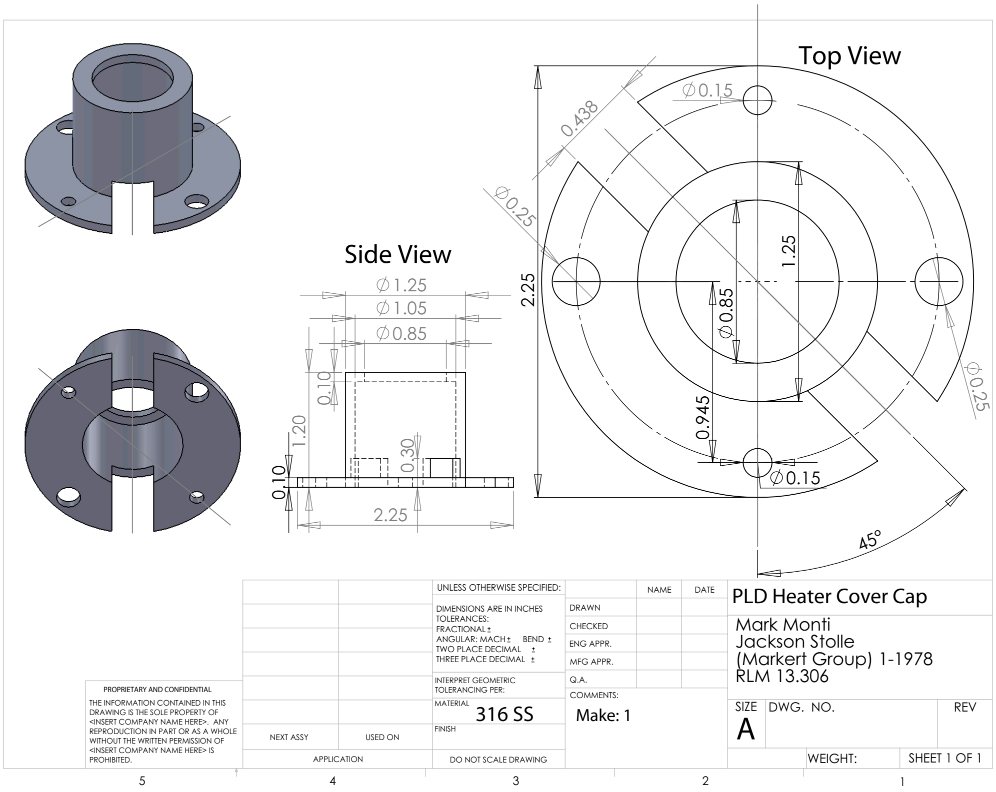

Figure A.3: SolidWorks drawing of the stainless steel cover cap.

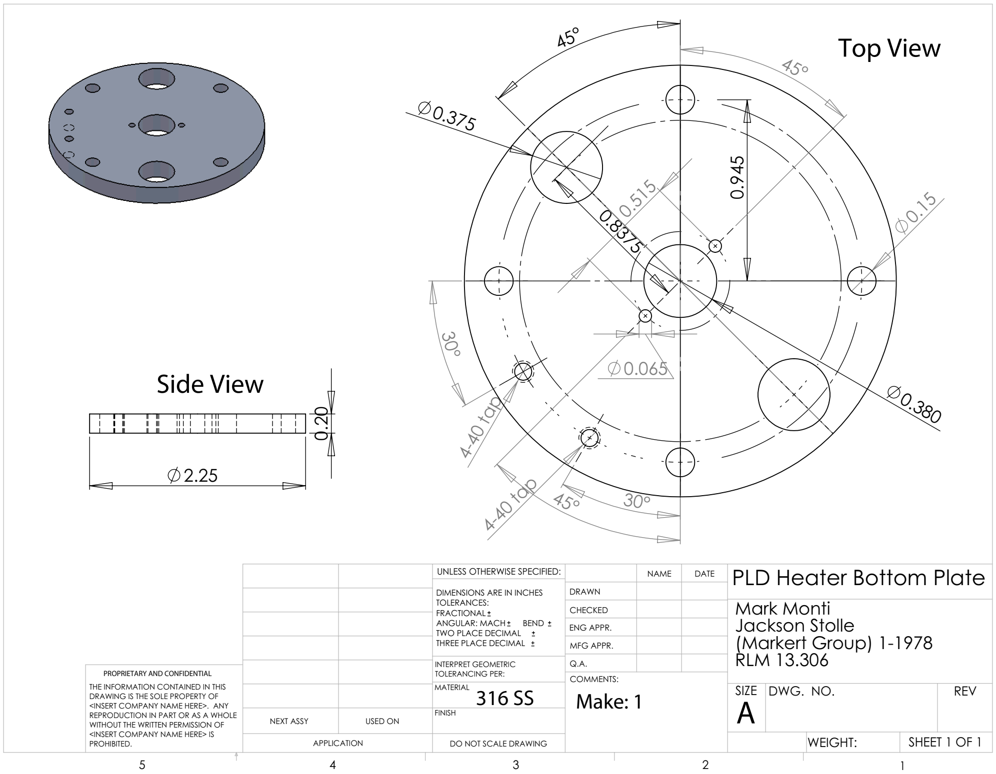

Figure A.4: SolidWorks drawing of the SS heater plate.

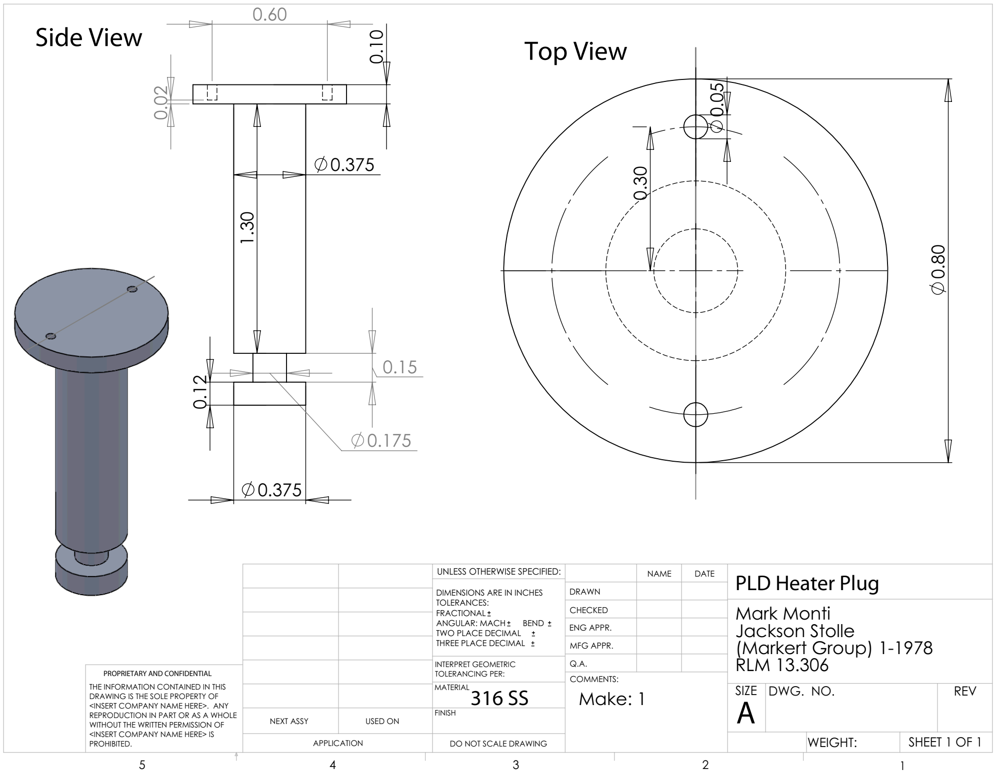

Figure A.5: SolidWorks drawing of the SS heater plug.

Appendix B

LabVIEW programs and switch box

The VDP configuration measurements for both sheet resistance and the Hall effect require switching the current and voltage leads on the sample for many different permutations. If done manually, this procedure would be extremely time consuming and very difficult to perform during temperature dependent measurements. A LabVIEW controlled switch box was designed to change the inputs to the LR400 four wire AC resistance bridge for the different VDP permutations.

The design of the switch box was centered around a polarized DIP single side stable mechanical relay (Zetler AZ832) that was chosen because it has a very short bounce and operating times, and it has a very low resistance of 50 mΩ. The pickup coil requires 128 mW and thus can be controlled using the standard 5V TTL output pulses from the digital I/O port of the computer's DAQ card. A solid state relay was not used because all solid state relays leak a finite amount of current and would thus affect the measurement accuracy. The relay's are controlled by acting as a pull-up resistor for the open collector output of a 7406 gate. The DAQ card sends a TTL voltage to the input of the 7406 gate (0 or 5V). A 0V signal causes the output of the 7406 to be open, and thus no current is drawn through the relays pick-up coil (see figure B.3). If the input to the 7406 is high (5V), then the output of the 7406 is low (0V), and current is drawn through the relay's pick-up coil, closing the switch. Thus, a high output from the DAQ card closes the switch of the mechanical relay.

The switch box contains separate PCB switching boards for the resistance and the Hall effect experiments. The schematic of the box is illustrated in figure B.1. The 24-pin connector plugs into the back of the box, and the sensing wires for the Pt and Ge RTD's are directly output to two separate 5 pin connectors that connect directly to a Lakeshore temperature controller. The four channels, I_1, I_2, V_1 and V_2, from the sample are then sent to four single-pole, double-throw mechanical switches on the front panel of the box, allowing the user to manually switch between resistance and Hall effect measurements. These four channels are then sent to either the resistance or the Hall effect PCB board that output the correct VDP configuration to the LR400. The DIP relays can be individually removed if one fails, but given the 20 million cycle lifetime, it should not be necessary very frequently. Each PCB board can be removed from the box by unplugging it from the cinch connector and removing the screws that secure it to the box. The connections between the various components are all wire-wrapped and color coded (see figure B.2).

LabVIEW programs control the DAQ digital I/O signals that are sent to the switch box, record the temperature from the Lakeshore temperature controller, and record the output (± 2V) from the LR400. The voltage from the LR400 is converted to the correct resistance value, corresponding to the settings of the LR400. These values of resistance are then plugged into the VDP formula and solved numerically for the sheet resistance or converted into the correct Hall voltage, depending on experiment.

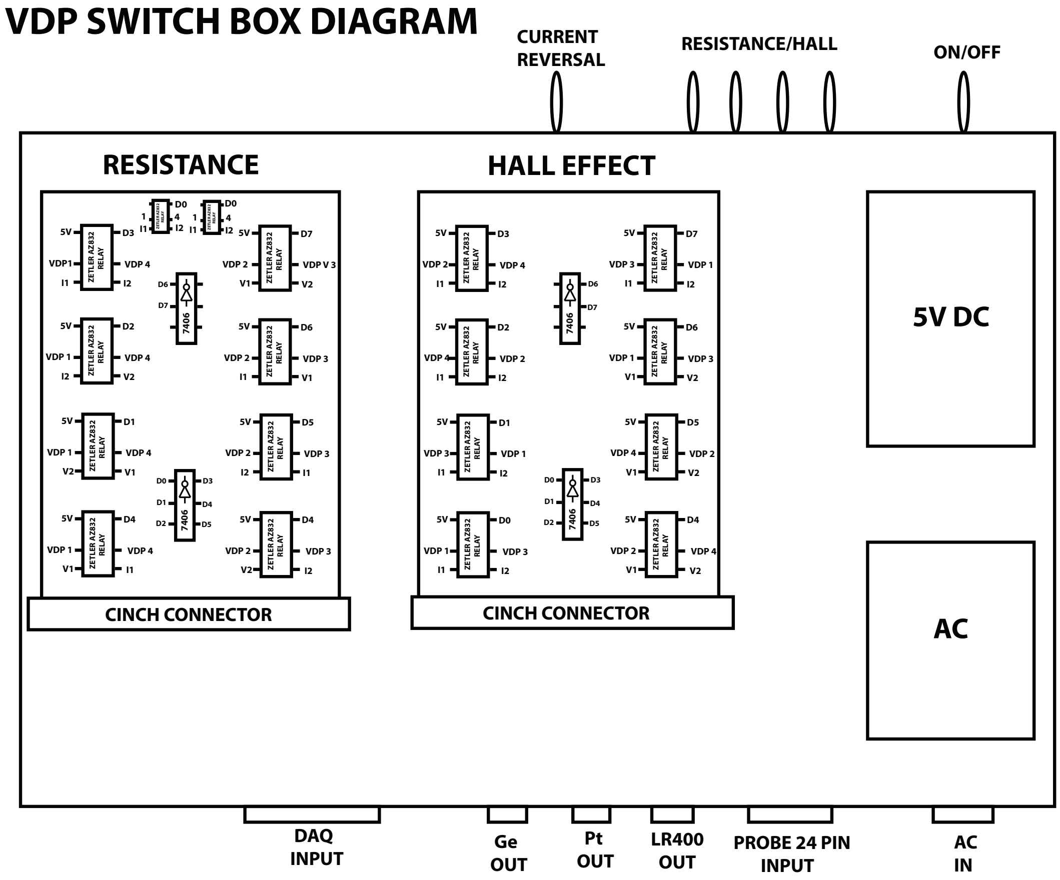

Figure B.1: A schematic of the switch box that controls the input channels to the LR400.

LR 400/ Pt/ Ge connectors

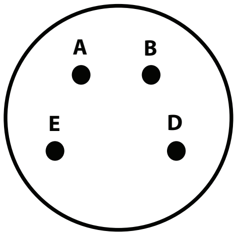

	PIN	SYMBOL	PCB CH	WIRE (to board)	WIRE WRAPING
LR 400	A	V2	19	white	blue-blue-blue
	B	V1	18	grey	red-red-red
	D	I2	20	yellow	black-black-blck
	E	I1	9	brown	green-green-green

		PROBE (24 PIN)
Ge	A	W
	B	V
	D	Y
	E	Z
Pt	A	U
	B	T
	D	a
	E	b

Resistivity configuration

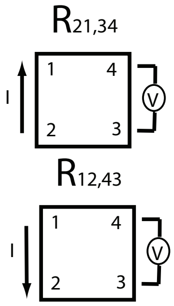

DAQ

DAQ CH	PCB CH	WIRE (to board)	WIRE WRAPPING
0	10	black	white
1	11	orange	white 1 stripe
2	12	brown	white 2 stripes
3	13	green	white 3 stripes
4	14	yellow	“ ”
5	16	white	“ ”
6	16	purple	“ ”
7	17	red	“ ”

Hall Effect configuration

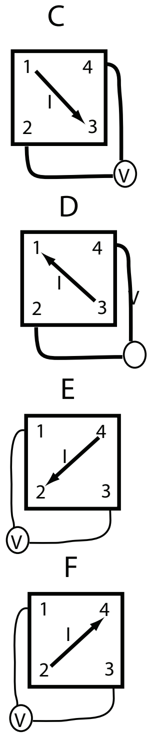

PROBE (24 PIN)

PROBE	VDP#	PCB CH	WIRE WRAPPING
C	1	1	green stripe
A	2	3	red stripe
B	3	4	blue stripe
D	4	2	black stripe

Resistivity Configuration	
R21,34 & R12,43	DAQ 2, 6
R32,41 & R23,14	DAQ 1, 5
R43,12 & R34,21	DAQ 0, 4
R14,23 & R41,32	DAQ 3, 7

Hall Configuration	
C	DAQ 0, 4
D	DAQ 1, 5
E	DAQ 2, 6
F	DAQ 3, 7

Figure B.2: The important wiring connections used in the switch box.

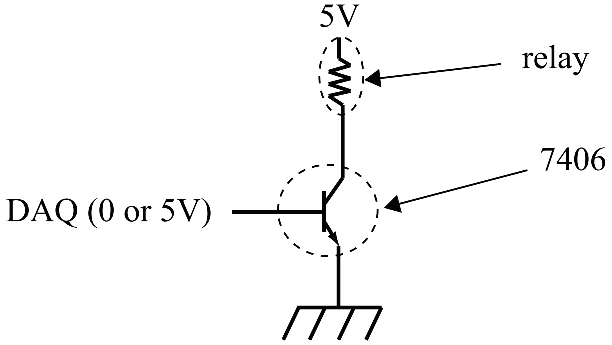

Figure B.3: The mechanical relay (model AZ832) is used as a pull-up resistor for the open collector output of the 7406 NAND gate. A high input from the DAQ card (5V) turns on a switch, which connects an input to the LR400 with the appropriate wire-bonded lead on the sample.

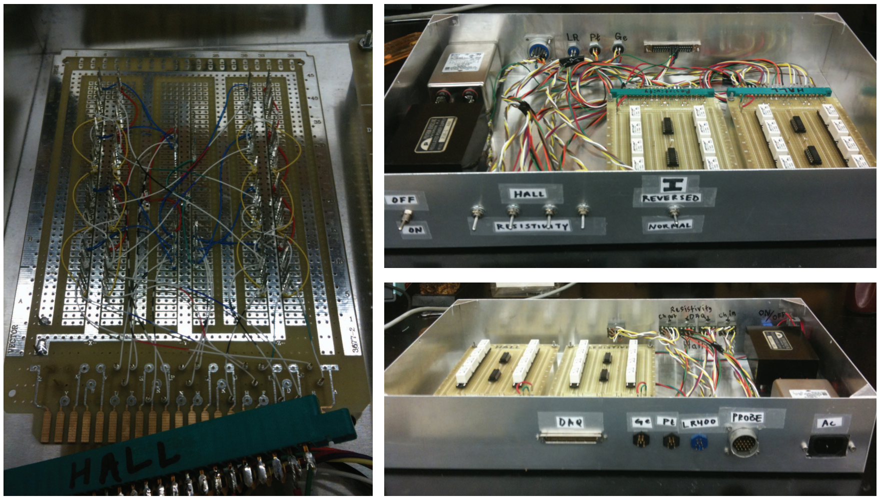

Figure B.4: Pictures of the switch box.

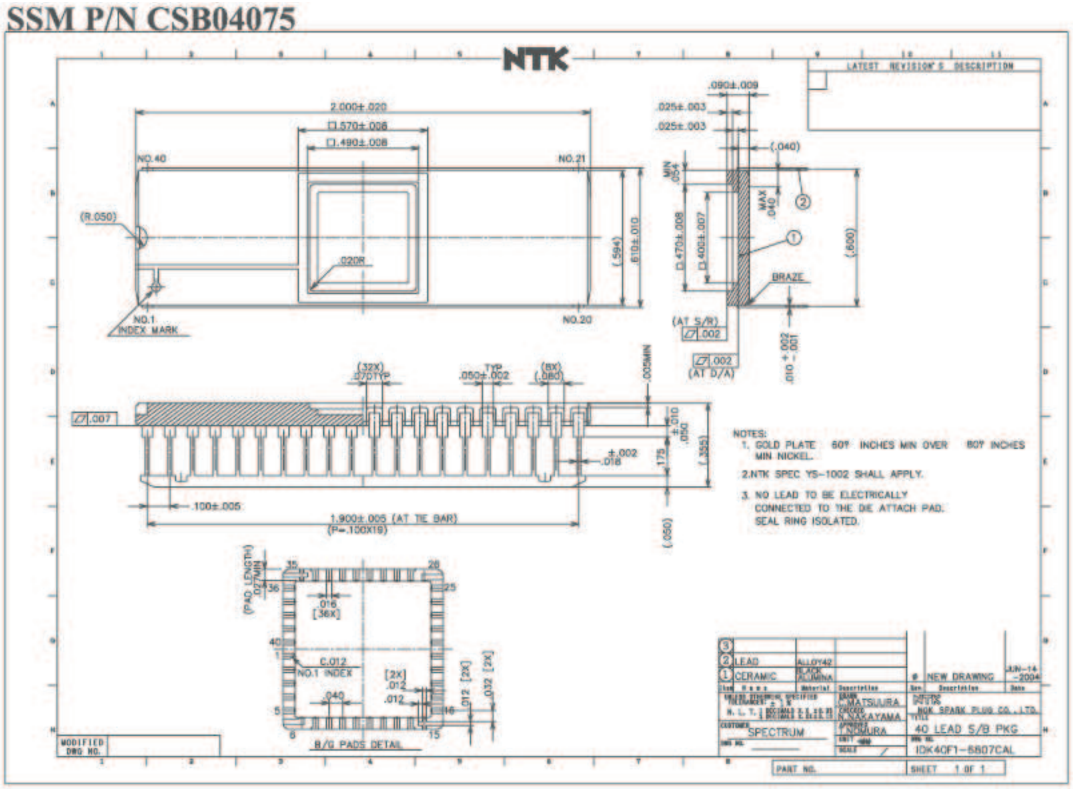

NOTES:
1. GOLD PLATE 60? INCHES MIN OVER 80? INCHES MIN NICKEL.
2.NTK SPEC YS-1002 SHALL APPLY.
3. NO LEAD TO BE ELECTRICALLY CONNECTED TO THE DIE ATTACH PAD. SEAL RING ISOLATED.

Figure B.5: This data sheet for Spectrum Semiconductor Materials, Inc. model SSM P/N CSB04075 chip carrier, shows the important correspondence between the gold contact pads and the DIP leads.

Bibliography

[1] H. Kroemer. http://nobelprize.org/nobel_prizes/physics/laureates/2000 /kroemer-lecture.html.

[2] A. Ohtomo and H. Hwang, *Nature*, vol. 427, p. 423, 2004.

[3] N. Reyren, S. Thiel, A. D. Caviglia, L. F. Kourkoutis, G. Hammerl, C. Richter, C. W. Schneider, K. T, A.-S. Ruetschi, D. Jaccard, M. Gabay, D. A. Muller, J.-M. Triscone, and J. Mannhart, *Science*, vol. 317, p. 1196, 2007.

[4] A. Brinkman, M. Huijben, M. V. Zalk, J. Huijben, U. Zeitler, J. C. Maan, W. G. van der Wiel, G. Rijnders, D. H. A. Blank, and H. Hilgenkamp, *Nat. Mater.*, vol. 6, p. 493, 2007.

[5] S. Thiel, G. Hammerl, A. Schmehl, C. W. Schneider, and J. Mannhart, *Science*, vol. 313, p. 1942, 2006.

[6] M. Takizawa, H. Wadati, K. Tanaka, M. Hashimoto, T. Yoshida, A. Fujimori, A. Chikamatsu, H. Kumigashira, M. Oshima, K. Shibuya, T. Mihara, T. Ohnishi, M. Lippmaa, M. Kawasaki, H. Koinuma, S. Okamoto, and A. J. Millis, *Phys. Rev. Lett.*, vol. 97, p. 057601, 2006.

[7] N. Nakagawa, H. Y. Hwang, and D. A. Muller, *Nat. Mater.*, vol. 5, p. 204, 2006.

[8] M. Huijben, G. Rijnders, D. H. A. Blank, S. Bals, S. V. Aert, J. Verbeeck, G. V. Tendeloo, A. Brinkman, and H. Hilgenkamp, *Nat. Mater.*, vol. 5, p. 556, 2006.

[9] W. Siemons, G. Koster, H. Yamamoto, T. H. Geballe, D. H. A. Blank, and M. R. Beasley, *Phys. Rev. B*, vol. 76, p. 155111, 2007.

[10] W. Siemons, G. Koster, H. Yamamoto, W. A. Harrison, G. Lucovsky, T. H. Geballe, D. H. A. Blank, and M. R. Beasley, *Phys. Rev. Lett.*, vol. 98, p. 196802, 2007.

[11] G. Herranz, M. Basletic, M. Bibes, C. Carretero, E. Tafra, E. Jacquet, K. Bouzehouane, C. Deranlot, A. Hamzic, J.-M. Broto, A. Barthelemy, and A. Fert, *Phys. Rev. Lett.*, vol. 98, p. 216803, 2007.

[12] A. D. Caviglia, S. Gariglio, N. Reyren, D. Jaccard, T. Schneider, M. Gabay, S. Thiel, G. Hammerl, J. Mannhart, and J. M. Triscone, *Nature*, vol. 456, p. 624, 2008.

[13] K. Yoshimatsu, R. Yasuhara, H. Kumigashira, and M. Oshima, *Phys. Rev. Lett.*, vol. 101, p. 026802, 2008.

[14] Z. S. Popovic, S. Satpathy, and R. M. Martin, *Phys. Rev. Lett.*, vol. 101, p. 256801, 2008.

[15] M. Basletic, J. L. Maurice, C. Carretero, G. Herranz, O. Copie, M. Bibes, E. Jacquet, K. Bouzehouane, S. Fusil, and A. Barthelemy, *Nat. Mater.*, vol. 7, p. 621, 2008.

[16] A. Kalabukhov, R. Gunnarsson, J. Borjesson, E. Olsson, T. Claeson, and D. Winkler, *Phys. Rev. B.*, vol. 75, p. 121404, 2007.

[17] J. Eckstein, *Nat. Mater.*, vol. 6, p. 473, 2007.

[18] G. Herranz, M. Basletic, O. Copie, M. Bibes, A. Khodan, C. Carretero, E. Tafra, E. Jacquet, K. Bouzehouane, A. Hamzic, and A. Barthelemy, *Appl. Phys. Lett.*, vol. 94, p. 012113, 2009.

[19] M. Shalom, C. Tai, Y. Lereah, M. Sachs, E. Levy, D. Rakhmilevitch, A. Palevski, and Y. Dagan, *Phys. Rev. B*, vol. 80, p. 140403, 2009.

[20] N. Reyren, S. Gariglio, A. Caviglia, D. Jaccard, T. Schneider, and J. Triscone, *Appl. Phys. Lett.*, vol. 94, p. 112506, 2009.

[21] O. Copie, V. Garcia, C. Bodefeld, C. Carretero, M. Bibes, G. Herranz, E. Jaquet, J. Maurice, B. Vinter, and S. Fusil, *Phys. Rev. Lett.*, vol. 102, p. 216804, 2009.

[22] A. Tukazaki, A. Ohtomo, T. Kita, Y. O. nd H. Ohno, and M. Kawasaki, *Science*, vol. 315, p. 1388, 2007.

[23] "Particle in a box." http://hyperphysics.phy-astr.gsu.edu/Hbase /quantum/pbox.html.

[24] J. Maurice, D. Imhoff, J. Contour, and C. Colliex, *Philosophical Magazine*, vol. 86, no. 15, p. 2131, 2006.

[25] D. Ligny and P. Richet, *Phys. Rev. B*, vol. 53, no. 6, p. 3013, 1996.

[26] T. Mitsui, S. Nouma, and L. Bornstein, eds., *Numerical Data and Functional Relations in Science and Technology-Crystal and Solid State Physics*, vol. 16. Springer Berlin, 1982. New Series Group III Pt a.

[27] H. Frederikse, W. Thurber, and W. Holser, *Physical Review*, vol. 134, no. 2A, p. 442, 1964.

[28] C. Koonce, M. Cohen, J. Schooley, W. Hosler, and E. Pfeiffer, *Phys. Rev.*, vol. 163, p. 380, 1967.

[29] T. Fix, J. MacManus-Driscoll, and M. Blamire, *Appl. Phys. Lett.*, vol. 94, p. 172101, 2009.

[30] M. Scullin, J. Ravichandran, C. Yu, M. Huijben, J. Seidel, A. Majumdar, and R. Ramesh, *Acta Materialia*, vol. 58, p. 457, 2010.

[31] R. Francis, S. Moss, and A. Jacobson, *Phys. Rev. B*, vol. 64, p. 235425, 2001.

[32] C. Howard, B. Kennedy, and B. Chakoumakos, *J. Phys.: Condens. Matter*, vol. 12, p. 349, 2000.

[33] P. Perna, D. Maccariello, M. Radovic, U. S. di Uccio, I. Pallecchi, M. Codda, D. Marre, C. Cantoni, J. Gazquez, M. Varela, S. Pennycook, and F. Granozio, *Appl. Phys. Lett.*, vol. 97, no. 15, p. 152111, 2010.

[34] W. A. Harrison, E. A. Kraut, J. R. Waldrop, and R. W. Grant, *Phys. Rev. B*, vol. 8, no. 8, p. 4402, 1978.

[35] S. Chambers, *Advanced Materials*, vol. 22, pp. 219–248, 2010.

[36] C. J. Stolle, "Methods for studying the interface of laalo3 grown on srtio3." Senior Honors Thesis UT Austin, 2010.

[37] M. Kawasaki, K. S. Takahashi, T. Maeda, R. Tsuchiya, M. Shinohara, O. Ishiyama, T. Yonezawa, M. Yoshimoto, and H. Koinuma, *Science*, vol. 266, p. 1540, 1994.

[38] M. Kareev, S. Prosandeev, J. Liu, C. Gan, A. Kareev, J. Freeland, M. Xiao, and J. Chakhalian, *Appl. Phys. Lett.*, vol. 93, p. 061909, 2008.

[39] G. Koster, B. Kropman, G. Rijnders, D. Blank, and H. Rogalla, *Appl. Phys. Lett.*, vol. 73, p. 2920, 1998.

[40] T. Ohnishi, K. Shibuya, M. Lippmaa, D. Kobayashi, H. Kumigashira, M. Oshima, and H. Koinuma, *Appl. Phys. Lett.*, vol. 85, p. 272, 2004.

[41] S. Thiel, *Study of Interface Properties in LaAlO3/SrTiO3 Heterostructures.* PhD thesis, University of Augsburg, 2009.

[42] S. Thiel, C. Schneider, L. Kourkoutis, D. Muller, N. Reyren, A. Caviglia, S. Gariglio, J.-M. Triscone, and J. Mannhart, *Phys. Rev. Lett.*, vol. 102, p. 046809, 2009.

[43] R. Eason, ed., *Pulsed Laser Deposition of Thin Films.* Hoboken, NJ: Wiley, 2007.

[44] "Loi de bragg." http://en.wikipedia.org/wiki/File:Loi_de_bragg.png.

[45] F. Brown, *The physics of solids.* New York: W.A. Benjamin, 1967.

[46] F. Smits, *The Bell System Technical Journal*, vol. May, pp. 711–718, 1958.

[47] D. Vaughan, *British Journal of Applied Physics*, vol. 12, pp. 414–416, 1961.

[48] D. Perloff, *Solid-State Electronics*, vol. 20, pp. 681–687, 1977.

[49] L. van der Pauw, *Philips Research Reports*, vol. 13, pp. 1–9, 1958.

[50] L. van der Pauw, *Phillips Technical Review*, vol. 20, pp. 220–224, 1959.

[51] S. Lim, D. McKenzie, and M. Bilek, *Review of Scientific Instruments*, vol. 80, 2009.

[52] J. Weiss, R. Kaplar, and K. Kambour, *Solid-State Electronics*, vol. 52, pp. 91–98, 2008.

[53] "Nist hall effect measurements." http://www.nist.gov/eeel /semiconductor/hall_resistivity.cfm.

[54] D. Look, *Electrical Characterization of GaAs Materials and Devices.* John Wiley and Sons, 1989.

[55] D. Koon, A. Bahl, and E. Duncan, *Review of Scientific Instruments*, vol. 60, pp. 275–276, 1989.

[56] D. Koon, *Review of Scientific Instruments*, vol. 60, pp. 271–274, 1989.

[57] D. Koon and C. Knickerbocker, *Review of Scientific Instruments*, vol. 64, pp. 510–513, 1993.

[58] O. Bierwagen, T. Ive, c. van de Walle, and J. Speck, *App. Phys. Lett.*, vol. 93, p. 242108, 2008.

[59] A. Kalabukhov, R. Gunnarsson, J. Borjesson, E. Olsson, D. Winkler, and T. Claeson, *J. Phys: Conference Series*, vol. 100, p. 082039, 2008.

[60] J. Mannhart and D. Schlom, *Science*, vol. 327, p. 1607, 2010.

[61] R. Pentcheva and W. Pickett, *Phys. Rev. B*, vol. 74, p. 035112, 2006.

[62] S. Gariglio, N. Reyren, A. Caviglia, and J.-M. Triscone, *J. Phys.: Condens. Matter*, vol. 21, p. 164213, 2009.

[63] C. Bark, D. Felker, Y.Wang, Y. Zhang, H. Jang, C. Folkman, J. Park, S. Baek, X. Pan, E. Tsymbal, m.S. Rzchowski, and C. Eom, "Tailoring a two-dimensional electron gas at the laalo3/srtio3 (001) interface by epitaxial strain." arXiv:1011.4082v1, 2010.

[64] W. de Hass, J. de Boer, and G. van der Berg, *Physica*, vol. 1, p. 1115, 1933.

[65] J. Kondo, *Progress of Theoretical Physics*, vol. 32, p. 37, 1964.

[66] V. Ianca, A. Deshpande, and S. Hla, *Phys. Rev. Lett.*, vol. 97, p. 266603, 2006.

[67] A. Blanchly and N. Giordano, *Phys. Rev. B*, vol. 51, p. 12537, 1995.

[68] G. Chen and N. Giordano, *Phys. Rev. Lett.*, vol. 66, p. 209, 1991.

[69] A. Blanchly and N. Giordano, *Phys. Rev. B.*, vol. 46, p. 2951, 1992.

[70] V. Chandrasekhar, C. Haesendonck, and A. Zawadowski, eds., *Kondo effect and dephasing in low-dimensional metallic systems.* Kluwer Academic Publishers, 2000.

[71] V. C. et. al., *Phys. Rev. Lett.*, vol. 72, p. 2053, 1994.

[72] J. DiTusa, K. Lin, M. Park, M. Isaacson, and M. Parpia, *Phys. Rev. Lett.*, vol. 68, p. 678, 1992.

[73] D. Tindall and M. Jericho, *Phys. Rev. B.*, vol. 9, no. 7, p. 3113, 1974.

[74] J. Torrance, P. Lacorre, and A. Nazzal, *Phys. Rev. B*, vol. 45, no. 14, p. 8209, 1992.

[75] Y. Lee, C. Clement, J. Hellerstedt, J. Kinney, L. Kinnischtzke, S. Snyder, and A. Goldman, "Phase diagram of electrostatically doped srtio3." arXiv:1101.3750v1, 2011.

[76] Y. Kanke and A. Navrotsky, *J. Solid State Chem.*, vol. 141, p. 424, 1998.

[77] P. Dernier and R. Maines, *Mater. Res. Bull.*, vol. 6, p. 433, 1971.

[78] K. G. Jr., J.-C. Bunzli, and V. Pecharsky, eds., *Handbook on the physics and chemistry of rare earths*, vol. 39. Elsevier, 2009.

[79] L. Jiang, J. Guo, H. Liu, M. Zhu, X. Zhou, P. Wu, and C. Li, *J. Phys. Chem. Solids*, vol. 67, p. 1531, 2006.

[80] L. Vasylechko, A. Senyshyn, D. Trots, R. Niewa, W. Schnelle, and M. Knapp, *J. Solid State Chem.*, vol. 180, p. 1277, 2007.

[81] L. Vasylechko, Y. Pivak, A. Senyshyn, D. Savytskii, M. Berkowski, H. Borrmann, M. Knapp, and C. Paulmann, *J. Solid State Chem.*, vol. 178, p. 270, 2005.

[82] L. Vasylechko, A. Matkovskii, A. Senyshyn, D. Savytskii, and M. Knapp, *C. HASYLAB Ann. Rep.*, vol. 1, p. 251, 2003.

[83] L. Vasylechko, A. Senyshyn, and D. Trots, *C. HASYLAB Ann. Rep.*, vol. 1, p. 469, 2007.

[84] T. Basyuk, L. Vasylechko, I. Syvorotka, A. Fedorchuk, Y. Prots, and D. Trots, *C. HASYLAB Ann. Rep.*, vol. 1, p. 795, 2007.

[85] V. Goldschmidt, *Skr. Nor. Vidensk. Akad. Mat. Naturvidensk. KI.*, vol. 2, 1926.

[86] M. Chu, Y. Sun, U. Aghoram, and S. Thompson, *Annu. Rev. Mater. Res.*, vol. 39, p. 203, 2009.

[87] J. Welser, J. Hoyt, and J. Gibbons, *IEEE Electron. Device Lett.*, vol. 15, p. 100, 1994.

[88] J. Choi, U. Mirsaidov, C. Miller, Y. Lee, S. Guchhait, M. Chabot, W. Lu, and J. Markert, *Proceedings of SPIE*, vol. 5389, p. 399, 2004.

[89] M. W. et. al., *Science*, vol. 324, p. 367, 2009.

[90] J. R. et. al., *Adv. Mater.*, vol. 22, p. 2919, 2010.

[91] R. Woerdenweber, E. Hollmann, R. Kutzner, and J. Schubert, *J. Appl. Phys.*, vol. 102, p. 044119, 2007.

[92] A. Gozar, G. Logvenov, L. Kourkoutis, A. Bollinger, L. Giannuzzi, D. Muller, and I. Bezovic, *Nature*, vol. 455, p. 782, 2008.

[93] Y. Hotta, T. Susaki, and H. Hwang, *Phys. Rev. Lett.*, vol. 99, p. 236805, 2007.

[94] J. Sidles, *Appl. Phys. Lett.*, vol. 58, p. 2854, 1991.

[95] G. Binning, H. Rohrer, C. Gerber, and E. Weibel, *Phys. Rev. Lett.*, vol. 49, p. 57, 1982.

[96] G. Binning, C. Quate, and C. Gerber, *Phys. Rev. Lett.*, vol. 56, p. 930, 1986.

[97] D. Rugar, C. Yannoni, and J. Sidles, *Nature*, vol. 360, p. 563, 1992.

[98] D. Rugar, O. Zuger, S. Hoen, C. Yannoni, H. Vieth, and R. Kendrick, *Science*, vol. 264, p. 1560, 1994.

[99] B. Stipe and H. Mamin, *Phys. Rev. Lett.*, vol. 87, p. 76021, 2001.

[100] C. Miller, *Nuclear Magnetic Resonance Force Microscopy: Adiabaticity, External Field Effects, and Demonstration of Magnet-on-Oscillator Detection with Sub-Micron Resolution.* PhD thesis, University of Texas at Austin, 2003.

[101] U. Mirsaidov, *Nuclear Magnetic Resonance Force Microscopy of Ammonium Dihydrogen Phosphate and Magnetism of Cobalt Nanocrystals.* PhD thesis, University of Texas at Austin, 2005.

[102] Y. Lee, *Construction of a Low Temperature Nuclear Magnetic: Resonance Force Microscope.* PhD thesis, University of Texas at Austin, 2006.

[103] H. Chia, *Force Detected Nuclear Magnetic Resonance on (NH4)2SO4 and MgB2.* PhD thesis, University of Texas at Austin, 2009.

[104] J. Sidles and D. Rugar, *Phys. Rev. Lett.*, vol. 70, p. 3506, 1993.

[105] A. Abragam, *The Principles of Nuclear Magnetism.* Oxford: Clarendon Press, 1994.

[106] F. Borsa, M. Corti, and A. Rigamonti, *J. Appl. Phys.*, vol. 49, no. 3, p. 1383, 1978.

[107] M. Wencka, S. Vrtnik, M. Jagodic, Z. Jaglicic, S. Turczynski, D. Pawlak, and J. Dolinsek, *Phys. Rev. B*, vol. 80, p. 224410, 2009.

[108] C. Kittel, *Introduction to Solid State Physics*. Wiley, 7th ed., 2005.

[109] B. Wu, M. Zinkevich, F. Aldinger, and W. Zhang, *J. Phys. Chem. Solids*, vol. 68, p. 570, 2007.

Vita

Mark Charles Monti was born in Austin, TX. He met his wife Holly in a high school physics class where he truly found his future. After spending a year pursuing rock climbing after high school, he attended the University of California, San Diego and received a B.S in physics in 2005. He entered the Physics Department at the University of Texas at Austin in the fall of 2005 and joined Dr. John Markert's research group shortly thereafter. Mark worked first on nuclear magnetic resonance force microscopy and then on pulsed laser deposition of oxide thin films. After graduation Mark and Holly will move to Washington, DC.

Permanent address: monti@physics.utexas.edu

This dissertation was typeset with LaTeX[†] by the author.

[†] LaTeX is a document preparation system developed by Leslie Lamport as a special version of Donald Knuth's TeX Program.